Université de Montréal

SEARCH FOR HEAVY GLUONS FROM COMPOSITE HIGGS MODEL THROUGH VECTOR-LIKE TOP QUARK DECAY TOPOLOGIES WITH THE ATLAS EXPERIMENT

Par
Diane Shoaleh Saadi

Département de Physique
Faculté des arts et des sciences

Thèse présentée à la Faculté des études supérieures
en vue de l'obtention du grade de Philosophie Doctor (Ph.D.)
en Physique

Jury d'évaluation

Président rapporteur	Hugo Bouchard Université de Montréal département de physique
Directeur de recherche	Claude Leroy Université de Montréal département de physique
Examinateurs externe	Aldo Deandrea Université Claude Bernard Lyon 1 département de physique
Membre du jury	Georges Azuelos Université de Montréal département de physique
Représentant du doyen de la FES	Suzanne Giasson Université de Montréal département de chimie

Author's Contribution

The research presented in this thesis was produced within a collaborative effort in the ATLAS experiment. The list below is presented to summarize the author's contribution:

1. The production and validation of samples for "Bulk-RS" graviton, where graviton (G_{KK}) can decay like: $G_{KK} \to t\bar{t}$ [1]. Comparison with Z' samples (which were already validated) with graviton samples. More detail can be found in: https://twiki.cern.ch/twiki/bin/viewauth/AtlasProtected/KKGravitonToTTbar
2. The production and validation of samples for "Bulk-RS" gluons, where gluon (g_{KK}) can decay like $g_{KK} \to tT$. More detail can be found in [1] and: https://twiki.cern.ch/twiki/bin/viewauth/AtlasProtected/HeavyGluonSingleProductionVLQtT
3. The data to simulation comparison at reconstruction level, including a calculation of all systematic uncertainty effects, all the Monte Carlo simulation backgrounds and the implementation of the correction factors (but not including the data-driven back-ground parametrization estimates for the W + jets and QCD multi-jets backgrounds) [1, 2].

The author contributed also to the Run 1 TRT Performance which is not presented in this thesis [3].

She also participated to many shifts of class 1 and 2 listed in figure 1.

OTP Activities

Class 1

System	Activity	Task	2012	2013	2014	2015	Total
ID gen	Detector Operation	ATLAS ID Shifter (ACR)				9.24	9.24
ID gen	Detector Operation	ATLAS ID Shifter (ACR) in M7			7.22		7.22
General Tasks	Trigger	ATLAS Trigger Shifter (ACR)				1.98	1.98
General Tasks	Data Preparation	Online DQ shifts	6.57				6.57
Total	6.57		7.22	11.22	25.01		

Class 2

System	Activity	Task	2012	2013	2014	2015	Total
ID gen	Detector Operation	ATLAS ID Shadow Shifter				0.20	0.20
ID gen	Detector Operation	ID DCS Watcher (class-2)				6.66	6.66
TRT	Detector Operation	MILESTONE & OTHER COSMIC RUNS: TRT Operation and Monitoring Shifter in ACR			11.00		11.00
General Tasks	Data Preparation	Muon Combined DQ Monitoring Shifts	7.00				7.00
General Tasks	Computing/Software	Reconstruction Software Shifts	13.50	0.25			13.75
Total	20.50	0.25	11.00	6.86	38.61		

Class 3

System	Activity	Task	2012	2013	2014	2015	Total
TRT	Computing/Software	TRT Detector Response Simulation			0.25		0.25
TRT	Computing/Software	TRT Offline Commissioning, Performance & Optimisation		0.10			0.10
Total		0.10	0.25		0.35		

Figure 1: Shift activities from early 2012 to end of 2015.

Remerciements

During my work on this project, I was lucky to receive a permanent support and motivation from many great people. First of all, many thanks to my advisor, Prof. Claude Leroy, for giving me this opportunity and putting his trust in me to undertake this project with his fund. His enormous contribution of time and support inside and outside of the laboratory as well as our countless scientific discussions led to the success of this project. I would like to thank the examiners, Prof. Hugo Bouchard, Prof. Georges Azuelos, and Prof. Aldo Deandrea, for their invested time and effort as part of the jury committee. Furthermore, I would like to thank both ATLAS exotics, top and TRT group members. A few members in particular deserve special thanks: Dr. James Ferrando, a big thank you, for being a great conversational partner about the scientific details, and, for the great supervising; Dr. Danilo Ferreira de Lima, a special thank you, for always being available to fix any issues related to the analysis package that I used; Dr. Julien Plathier, thank you my love, for being present in my life, helping me with technical and mental support. Last but not least, I would like to thank my friends whose simple existence often provides the motivation for my work. And finally, I own my greatest gratitude to my country, France, for giving me freedom specially freedom of judgement, high quality education and a great sense of criticism.

Abstract

A search for production of the lightest Kaluza-Klein excitation of gluon (g_{KK}), in theories with a warped extra dimension, that decays into Standard Model (SM) top quark pairs ($t\bar{t}$) or into one vector-like top quark (VLQ top) in association with a SM top quark (Tt) is presented in this thesis. The search is based on proton proton collisions at $\sqrt{s} = 8$ TeV recorded in 2012 with the ATLAS detector at the CERN Large Hadron Collider and corresponding to an integrated luminosity of 20.3 fb^{-1}. For the analysis of $g_{KK} \to tT$, we performed targeting three cases: VLQ top (T) with significant branching ratio to a W boson and a b-quark ($T \to W\,b$), VLQ top with significant branching ratio to a composite Higgs boson and a standard model top quark ($T \to H\,t$) and VLQ top with significant branching ratio to a Z boson and a standard model top quark ($T \to Z\,t$). Data are analyzed in the lepton-plus-jets final state, characterized by an isolated electron or muon with high transverse momentum, large missing transverse momentum and multiple jets. The invariant mass spectrum of $t\bar{t}$ and $t\bar{t} + jets$ is examined for local excesses or deficits that are inconsistent with the Standard Model predictions. No evidence for a top quark pairs resonance is found, and 95% confidence-level limits on the production rate are determined for massive states in benchmark models. On the one hand, a Kaluza–Klein excitation of the gluon of width 15.3% with a branching ratio of 100% into a SM top quark pairs in a Randall–Sundrum model, is excluded for masses below 2.0 TeV. On the other hand, in a composite model where the heavy gluon decays to tT, using benchmark parameters for mixing angles, a 1.0 TeV Kaluza–Klein excitation of the gluon of width 10% that decay to one SM and a 0.6 TeV VLQ top, considering any VLQ top branching ratio scenario, is excluded at 95% Confidence Level (CL). Finally, a 2.0 TeV Kaluza–Klein excitation of the gluon, of width 10%, that decays into one SM in association with a 1.4 TeV VLQ top, with any scenario with BR ($T \to Wb$) < 0.80, is excluded at 95% CL. The samples used in these analyses were validated by ATLAS collaboration, however the results shown in this thesis were not reviewed by the ATLAS collaboration for publication.

Keywords: ATLAS, LHC, collider, vector-like quarks, resonance, analysis, Kaluza-Klein gluon, composite Higgs.

Résumé

La recherche de la production de gluons lourds g_{KK}, de type Kaluza-Klein dans la théorie avec dimensions supplémentaires, qui se désintègre en une paire de SM quark top ($t\bar{t}$), ou en un VLQ top et un SM quark top (tT), est présentée dans cette thèse. Cette recherche est basée sur les collisions de proton proton à $\sqrt{s} = 8$ TeV, enregistrées durant l'année 2012 par le détecteur ATLAS au LHC, au CERN. La luminosité, correspondante à ces énergies de collisions, a été de 20.3 fb^{-1}. Dans le cas de $g_{KK} \to tT$, trois types d'analyses ont été effectuées de façon indépendante: VLQ top (T) se désintégrant en un boson W et un quark b ($T \to W\,b$), avec un large rapport de branchement, VLQ top se désintégrant en un boson de Higgs composite et un SM quark top ($T \to H\,t$), avec un large rapport de branchement, et VLQ top se désintégrant en un boson Z et un SM quark top ($T \to Z\,t$). Dans chaque cas, les données, issues des collisions, sont étudiées dans des états finaux avec un lepton et des jets. Ces états sont caractérisés par un electron ou un muon isolé ayant une impulsion transverse large, une énergie transverse manquante et jets. Les spectres de la masse invariante de $t\bar{t}$ et de $t\bar{t} + jets$, sont ensuite examinés, afin de vérifier un éventuel excès (ou un déficit) inconsistant avec les prédictions du Modèle Standard. Aucune évidence de résonance de paire de quarks top a été observée, et une limite d'échelle de confiance de 95% a été déterminée pour des résonances lourdes prévues par les modèles benchmark. D'une part, une résonance correspondant à un gluon de type Kaluza–Klein (de largeur de 15.3%) prévu par le modèle Randall–Sundrum, qui se désintègre avec un taux d'embranchement de 100% en une paire de SM quarks top a été exclue avec 95% de degré de confiance, jusque pour les masses inférieures à 2.0 TeV. D'autre part, les excitations de gluon de type Kaluza–Klein, dans le modèle composite avec des paramètres de benchmark pour des angles de mélange et une largeur de 10%, de masse 1.0 TeV, qui se désintègrent en un SM quark top, et, un VLQ top de masse 0.6 TeV pour tous les embranchements propres à VLQ top, ont été exclues avec 95% de degré de confiance. Finalement, les excitations de gluon de type Kaluza–Klein, de largeur de 10%, ayant une masse de 2.0 TeV, qui se désintègrent en un SM quark top et un VLQ top de masse 1.4 TeV, avec des scenarios qui respectent BR ($T \to Wb$) < 0.80, ont été exclues avec 95% de degré de confiance. Les échantillons utilisés lors de cette analyse ont été validés par la collaboration ATLAS, cependant les résultats montrés dans cette thèse n'ont pas été vérifiés par la collaboration ATLAS en vue d'une publication.

Mots clés : ATLAS, LHC, collisionneur, quarks vectoriels, resonance, analyse, gluon de type Kaluza-Klein, Higgs composite.

Contents

List of Tables

List of Figures

List of Equations

List of abbreviations

MC	Monte Carlo . . . 60
SM	Standard Model . . . vii
p-p	proton proton . . . 10
VLQ	vector-like quarks . . . 2
g_{KK}	Kaluza-Klein excitation of gluon . . . vii
VLQ top	vector-like top quark . . . vii
QCD	Quantum ChromoDynamics . . . 6
QED	Quantum ElectroDynamics . . . 7
EW	ElectroWeak . . . 7
CKM	Cabibbo–Kobayashi–Maskawa . . . 10
vev	vacuum expectation values . . . 8
LSP	Lightest Supersymmetric Particles . . . 13
SUSY	SUperSYmmetry model . . . 2
f	fermion . . . 15
m_P	Planck scale . . . xxvii
Λ_{UV}	SM cutoff scale . . . xxvii
BSM	Beyond the Standard Model . . . 1
NGB	Nambu-Goldstone-Boson . . . 2
LH	Little Higgs . . . 16
Λ_{LH}	Little Higgs cutoff scale . . . 16
ADD	Arkani, Dimopoulos and Dvali . . . 17
KK	Kaluza-Klein . . . 17
RS	Randall-Sandrum . . . 18
AdS	Anti-de Sitter spaces . . . 19
CFT	Conformal Field Theory . . . 19
PMTs	photomultipliers . . . 42
LAr	Liquid Argon . . . 39

HEC Hadronic End-Cap . . . xix

EMEC ElectroMagnetic End-Cap . . . xix

FCal Liquid Argon Forward Calorimeter . . . 43

CL Confidence Level . . . vii

$\mu_{\mathbf{sig}}$ signal strength . . . 94

LO Leading Order . . . 71

NLO Next to Leading Order . . . 71

NNLO Next to Next to Leading Order . . . 83

JER Jet Energy Resolution . . . 52

JES Jet Energy Scale . . . 52

JMS Jet Mass Scale . . . 84

JMR Jet Mass Resolution . . . 84

JVF Jet Vertex Fraction . . . 52

PV Primary Vertex . . . 52

LCW Local Cluster Weights . . . 51

PDFs Parton Distribution Functions . . . 82

PDF Parton Distribution Function . . . 83

1 Introduction

Throughout human history, mankind has tried to describe anything that could be palpable. For example, humans described feelings, the objects and the animals around him, with words and art. With the progress of technology and methods for observations, we were able to describe celestial objects (stars, planets) and microscopic objects (molecules, atoms, nucleus, electrons) with mathematical models.

1.1 Modern physics

Nowadays, scientists look for the most elementary building blocks of matter. In modern accelerators, two particle beams, running at high energies increasingly, collide so the particles break into their constituents, called elementary particles. These particles are classified as fermions (quarks and leptons) and bosons. Their classification, according to their characteristics, was built by the theory of the Standard Model (SM) of Particle Physics. It is used to describe their interactions with one another under different conditions. These interactions are required in order to hold matter together and consequently for the existence of life. This model is verified, and, confirmed with excellent accuracy by many experiments.

The discovery of a new particle of 125 GeV consistent with the SM Higgs boson by the ATLAS and CMS collaborations is the latest major milestone in high-energy particle physics [15, 16].

1.2 Motivations

Despite all progress achieved, many fundamental questions remain unsolved to date. For instance, the observed matter-antimatter asymmetry in our universe, the origin of gravitationally interacting dark matter and the hierarchy problem [1] are not explained by the SM theory. Consequently, it is assumed that this model is a part of a bigger theory which includes new physics. Numerous models are proposed to address these issues, and many of them are being tested, rigorously constrained or completely have excluded by discovery, in the experiments at the LHC.

The discovery of the 125 GeV Higgs boson at the LHC as the final particle of the SM, increased the level of enthusiasm for theories Beyond the Standard Model (BSM) which postulate, with extreme

[1] hierarchy problem: loop corrections appear in the calculation of the Higgs boson mass [7]. If the standard model is to remain valid up to large energy scales such as the Planck scale, these loop corrections give rise to large divergences. The corrections needed to cancel these divergences exceed the actual mass of the Higgs boson itself by several orders of magnitude, which can be perceived as unnatural.

simplicity, the extension of the SM sector to new vector-like particles [2], enhancing certain Higgs boson production modes with respect to the standard model expectation strongly bounded by the LHC. Models with additional vector-like quarks (VLQ) compatible with current measurements of SM, have gained attractiveness. VLQ are predicted in many BSM, among which, SUperSYmmetry model (SUSY) model and few exotics models such as Little-Higgs models, Composite-Higgs models, models of extra dimensions or generically simplified models of an effective theory of the heavy gluon and the top partners. These models are proposed to solve the hierarchy problem and to explain the electroweak symmetry breaking.

The effective theory of the top partners, uses naturalness arguments to postulate a new mechanism in order to cancel quadratic divergences, that arise from radiative corrections to the Higgs boson mass. It also suggests, the existence of new heavy particles, which live in a 5-D space time world, called bulk, under $SU(3)_c \times O(4) \times U(1)_X$ global symmetry. As for the SM particles (SM Higgs boson excluded), they live in two elementary sectors enclosing an Anti-de-Sitter (AdS_5) bulk. A set of vector-like fermions, arises as composite states of a new QCD like, strong sector. These composite particles are characterized by their couplings to the SM particles, and, exist under multiplets composite vector-like forms of quarks. Unlike the SM quarks, both, their right-handed and left-handed components, have the same couplings to weak currents. With a mass of few TeV, they can affect the Higgs couplings and reduce the top-quark loop contribution. This Higgs doublet [17, 18] arises, thus, as a pseudo Nambu-Goldstone-Boson (NGB) boson of a larger symmetry breaking and is called composite Higgs. VLQ couple mainly to third generation SM quarks in this framework and are referred to as heavy top or bottom partners.

In parallel, with the effective theory of the heavy gluon, the lightest Kaluza-Klein excitation of gluon (g_{KK}) is introduced in theories with a warped extra dimension [19–22]. g_{KK}, also referred to as heavy gluon, transform under $SU(3)_c \times SU(2)_L \times SU(2)_R \times U(1)_X$ with a coupling to SM top quarks and VLQ top (T) large enough, so that, if kinematically allowed, g_{KK} decays with a large rate, to a pair of top quarks ($g_{KK} \to t\bar{t}$ or $g_{KK} \to T\bar{T}$) or to a SM top quark in association with a VLQ top ($g_{KK} \to T\bar{t}$) [3]. The VLQ top, from the effective theory of the top partners, is a $SU(2)_L$ doublet with charge $+2/3$. According to its largest coupling, it decays to Wb, Zt or Ht (t and H stand for SM top and Composite Higgs, respectively).

[2] The new vector-like particles share similar properties as the already known quarks.

[3] Considering $t\bar{t}$ ($t\bar{t}$+jets) as final states (g_{KK} coupling to $t\bar{t}$, instead of coupling to lighter quarks) is not a coincidence: the SM top quark is the most massive of the fundamental particles in the SM with a large coupling to Composite Higgs bosons [23–29]

1.3 Objectives

Considering the large cross section of g_{KK} for collisions of 8 TeV at the LHC, a search for heavy gluon production, via Drell-Yan process, has been performed using data with an integrated luminosity of 20.3 fb^{-1} recorded in 2012 by the ATLAS experiment. For each channel, a separate analysis has been done with final states involving one isolated electron or muon, high missing transverse momentum from the undetected neutrino and multiple jets.

The search presented in this thesis, is designed to be sensitive to the production of a heavy gluon that decays to $t\bar{t}$. The benchmark models adopted include colour-singlet bosons with spin 1 and masses from 0.4 to 3 TeV. The resonance width for the specific models varies from very narrow (1%) to a size similar to that of the experimental resolution (15%). Furthermore, the dependence of the limits on the resonance width is explored for heavy gluons up to a width of 40%. With these results, it is possible to interpret the cross-section limits in the context of a search for heavy gluon that decays to tT with the same production modes, in a composite model using benchmark parameters for mixing angles . The strategy used in this research is detailed in reference [1].

1.4 Synopsis

At the beginning of this thesis in Chapter 2, it has been considered that many references [7, 30–32] describe very well the SM of particle physics from different points of view. Hence, only the essential parts of the model, necessary to understand the main subject of this thesis, are detailed. In Chapter 3, after an overview of Little Higgs model and extra dimensions model, an effective two-site model is adopted to study the phenomenology of the heavy gluon and heavy fermions. Chapter 4, focuses on the experimental setup used to perform the analyses, and, the prospects of observing the heavy-light decays of g_{KK} in Wtb, Zt and Ht events at the LHC. Chapter 5, presents the measurements and searches done using the results of proton proton collisions in the ATLAS detector at the LHC. In Appendix A, the units used in this thesis are listed. Finally, in Appendix B and C are shown the results of g_{KK} sample validation using MADGRAPH+PYTHIA versus MADGRAPH only for tZ channel and tH channel respectively. The samples used in these analyses were validated by ATLAS collaboration, however the results shown in this thesis are preliminary.

2 The Standard Model of Particle Physics

Modern physics classifies the elementary particles and describes their interactions in the SM of Particle Physics as shown in figure 2.1. This model predicts the existence of six generations of fermions (leptons and quarks) and twelve bosons (eight gluons carrying colors, one photon, one Z, W^+ and W^- bosons).

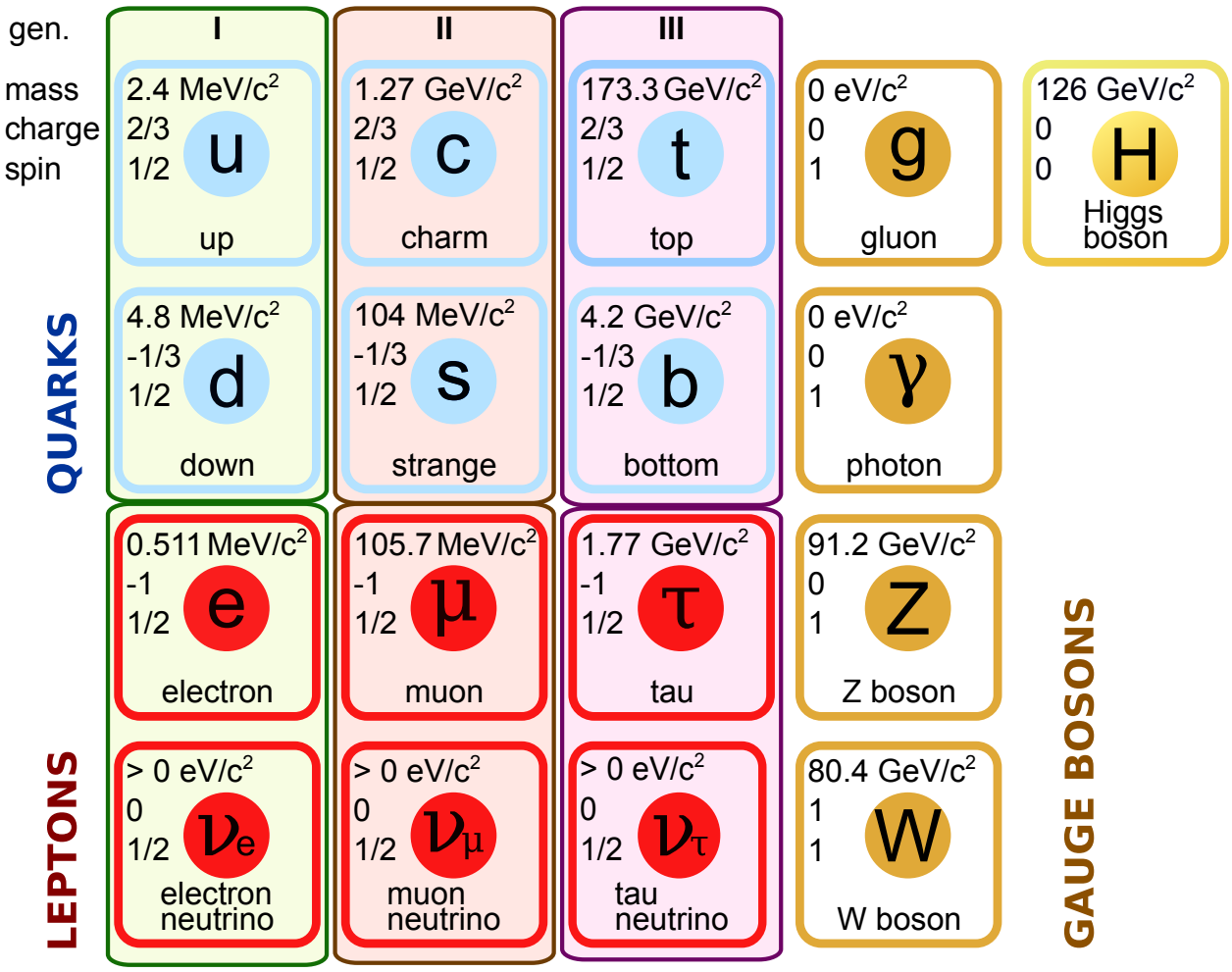

Figure 2.1: The properties of the Standard Model of particles. The SM particles are classified as quarks (in blue) of three generations (gen. I, II and III), leptons (in red) of three generations and bosons (in gold and yellow). These particles are denoted with their symbols (for instance, t for top quark in the middle of a blue circle). Their masses, charges and spin are shown in the Figure. The values are taken from the Review of Particle Physics [4].

Bosons have integer spin ($s = 0,\ 1$) and play the role of the mediator of the interaction between fermions. Leptons are half-integer spin particles and interact via weak interaction by exchange of $W^{\pm}$ or Z boson, or via electromagnetic interaction by exchange of photons. These interactions follow the Gauge symmetry $SU(2)_L \times U(1)_Y$ of weak isospin and hyper-charge [7]. Quark interact via the Quantum ChromoDynamics (QCD), based on the SU(3) symmetry group. In QCD, it is predicted that quarks are color triplets and interact with eight-colored gluons [1], which are also called as the mediator of the strong interaction. High precision measurements confirm the existence of the vector part of the SM. Although, the QCD coupling constant gets small as energies increase (E $>$ GeV), quarks and gluons will always appear as the fundamental constituants of hadrons such as protons and neutrons. Besides, quarks and gluons interactions follow rules such as all three colors (or color-anticolor) must be present and the resulting hadron has integer spin and is colorless.

2.1 Matter Fields and Gauge Fields

In quantum mechanics, fermions are called Matter fields ψ with chiral components defined as:

$$\psi_{L,R} = \frac{1}{2}(1 \pm \gamma_5)\psi\,. \tag{2.1}$$

Where γ_5 matrice is the product of four Dirac matrices $\gamma_5 = i\gamma_0\gamma_1\gamma_2\gamma_3$. In the SM, the Matter Fields from left chiral [2] fermions (L) are isospin doublets while the ones from right chiral fermions (R) are isospin singlets and denoted as [3]:

$$q_{iL} = \begin{pmatrix} u_i \\ d_i \end{pmatrix}_L,\ u_{iR},\ d_{iR}. \qquad l_{iL} = \begin{pmatrix} \nu_i \\ e_i \end{pmatrix}_L,\ e_{iR}\,.$$

Where q, l and i stand for quark, lepton and the fermion family, respectively (see figure 2.1) [4]. The third component of weak isospin (I^3) is a quantum number which is related to the singlet isospin Matter

[1] Gluons have an electric charge of zero.

[2] Usually we say left-handed (right-handed) instead of left (right) chiral fermion. In the SM, particles are isospin doublet left-handed and the anti-particles are isospin singlet right-handed

[3] The SM does not have a right-handed component for neutrinos, so its left-handed component is massless.

[4] If we take the third family of quarks and the first family of leptons then we get:

$$q_{3L} = \begin{pmatrix} t \\ b \end{pmatrix}_L,\ \bar{t},\ \bar{b}. \qquad l_{1L} = \begin{pmatrix} \nu_e \\ e^- \end{pmatrix}_L,\ e^+.$$

fields as $I^3_{\psi_R} = 0$ and to the doublet isospin Matter fields as

$$I^3_{\psi_L} = \begin{pmatrix} +1/2 \\ -1/2 \end{pmatrix}.$$

However, the most common parameter used is the weak hyper-charge Y_ψ. It links the third component of weak isospin I^3_ψ and electric charge Q_f (defined in the proton charge '+e' units) of the fermion f via the relation: $Y_\psi = Q_f - I^3_\psi$.

Finally, Gauge fields are related to bosons. There are two Gauge fields: B_μ with the quantum number Y of the U(1) symmetry Gauge group and W_μ with the isospin group SU(2) generator.

2.2 Lagrangian and local Gauge transformation of the Standard Model

As Matter and Gauge fields have been defined, one can approach the dynamics of the particle fields. To do so, field theory uses a function called Lagrangian density (or Lagrangian). The dynamic of a free particle of mass m is defined by the Lagrangian:

$$\mathcal{L} = i\bar{\psi}\gamma^\mu\partial_\mu\psi - m\bar{\psi}\psi\,, \tag{2.2}$$

with γ_μ denoting Dirac matrices and $\partial_\mu = \frac{\partial}{\partial x^\mu}$.

From Quantum ElectroDynamics (QED) theory, the equations of motion remain invariant under global transformations. Nevertheless, everything changes when we add a space dependent parameter (θ_μ) in the Lagrangian equation to study a particle in interaction. This case is referred to as local Gauge. The first term of the Lagrangian 2.2 becomes then, $-\bar{\psi}[\gamma^\mu\partial_\mu\theta_\mu]\psi$ and breaks the Gauge symmetry. To overcome this, one needs the covariant derivative (D_μ) which is a function of the particle charge q and a vector field A (electromagnetic four-potential) as follows:

$$\gamma^\mu D_\mu = \gamma^\mu\partial_\mu - iq\gamma^\mu A_\mu\,. \tag{2.3}$$

By using $q\gamma^\mu A_\mu = \gamma^\mu\partial_\mu\theta(\mu)$ in the Lagrangian equation 2.2, the Gauge invariance is restored under U(1).

Finally, the unification of the electromagnetic (of infinite range) and weak (of range $\Delta R = 10^{-17}$ m) forces is possible if the energy gets high enough so the two forces unify into a single force called ElectroWeak (EW). The latter force is then carried by the W^+, W^- , Z^0 and γ bosons. But how is it

possible, under a unique EW interaction, to maintain an invariant symmetry transformation and having massive EW gauge bosons [5]?

2.3 A theory developed by Brout–Englert–Higgs

A model to explain how mass could arise in local Gauge theory has been proposed by Robert Brout, François Englert and Peter Higgs. Their theory consists of the prediction of the Higgs field and Higgs boson [6]: when the energy scale of experimental observations is lower than the EW scale, a spontaneous symmetry breaking mechanism causes an asymmetry between electromagnetism and weak interactions. Furthermore, W and Z bosons acquire their masses as a consequence of the latter symmetry breaking mechanism (called Higgs mechanism) [7].

The Higgs mechanism provides an isospin doublet Φ of weak hyper-charge $Y = 1$ and forms four scalar fields:

$$\Phi = \begin{pmatrix} \phi^+ \\ \phi^0 \end{pmatrix}, \text{ with } \phi^+ = (\phi_1 + i\phi_2)/\sqrt{2},\ \phi^0 = (\phi_3 + i\phi_4)/\sqrt{2}\,.$$

The Higgs field couples to the gauge bosons and to itself through the potential V(ϕ) defined as:

$$V(\Phi) = \mu^2 \Phi^\dagger \Phi + \lambda (\Phi^\dagger \Phi)^2, \tag{2.4}$$

where λ and μ^2 are two parameters which control the Higgs potential shape. As shown in figure 2.2, for $\mu^2 > 0$, the potential $V(\Phi)$ is symmetric and has one single minimum at $\Phi = 0$. However, when μ^2 takes negative values, $V(\Phi)$ takes two minima at $\Phi = -\nu$ and $\Phi = +\nu$ called vacuum expectation values (vev) is SU(2) invariant. If one vev is arbitrarily set to

$$\phi_0 = \sqrt{\frac{1}{2}} \begin{pmatrix} 0 \\ \nu \end{pmatrix}$$

then, the EW Gauge symmetry is locally broken. For convenience, the scalar doublet is thus considered as follows:

$$\phi = \sqrt{\frac{1}{2}} \begin{pmatrix} 0 \\ \nu + h(x) \end{pmatrix}.$$

The Lagrangian contains three massless Gauge bosons $W^1_\mu(x)$, $W^2_\mu(x)$ and $W^3_\mu(x)$ and $B_\mu(x)$.

[5] Bosons mass are: $m_W = 80.4$ GeV, $m_Z = 91.2$ GeV and $m_\gamma = 0$ eV [31].
[6] This theory is also called Brout–Englert–Higgs (BEH), but, we traditionally call it after Higgs only.

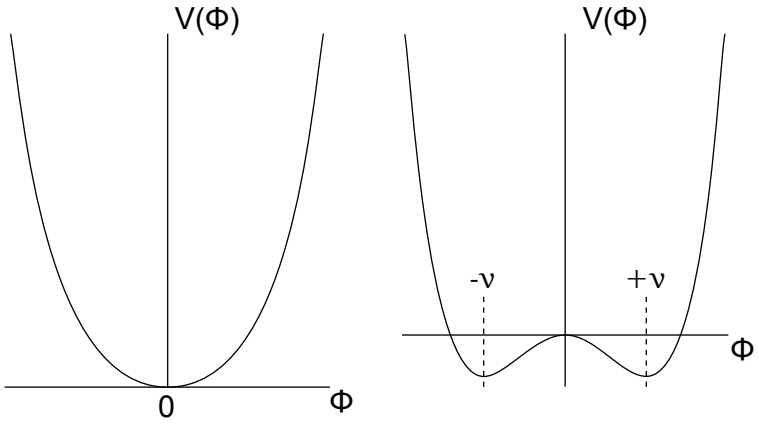

Figure 2.2: Higgs Potential as a function of μ^2 [5]. Left side: $\mu^2 > 0$ and $\lambda > 0$ so the potential has only one minimum at origin. Right side: $\mu^2 < 0$ and $\lambda > 0$ so the potential has two minima ($-\nu$, $+\nu$) and a maximum at origin.

Consequently the Higgs theory has four degrees of freedom corresponding to the four scalar fields. When the Gauge symmetry is spontaneously broken, three of the latter degrees of freedom disappear in the acquisition of W and Z bosons mass (in the unitary gauge). Besides, the W and Z boson couplings to the Higgs are of the form [7]:

$$\mathcal{L} = |D_\mu \phi|^2 = |(i\partial_\mu - g\frac{1}{2}\tau.W_\mu - g'\frac{Y}{2}B_\mu)\phi|^2 \,. \tag{2.5}$$

Since the electromagnetic symmetry is kept invariant, the photon remains massless. The fourth degree of freedom is nothing else than the scalar field h(x) called the Higgs boson H^0 whose properties are described in the section 2.5. The charged SM fermions acquire their mass via Yukawa-Higgs field coupling. So, the charged lepton Yukawa Lagrangian is defined as follows [7]:

$$\mathcal{L}_{Yukawa} = -G_l[\bar{\psi_R}(\phi^\dagger \psi_L) + (\bar{\psi_L}\phi)\psi_R] = -\frac{\nu G_l}{\sqrt{2}}\bar{l}l - \frac{G_l}{\sqrt{2}}\bar{l}lH \,, \tag{2.6}$$

where G_l is a function of the charged lepton mass as $m_l = \nu G_l/\sqrt{2}$ and l stands for the charged lepton. The Yukawa coupling of the SM quarks is very similar to the charged leptons. So we can easily conclude that the strength of the fermion-Higgs Yukawa coupling is proportional to the fermion mass in the SM framework. Therefore, the heaviest SM particle which is the top quark is strongly coupled to the Higgs boson.

2.4 Characteristics and production of the top quark

The top quark is the heaviest particle in the SM with a mass of $m_t = 173.34 \pm 0.27$ (stat) $\pm$ 0.71 (syst) GeV [4]. It has a lifetime $\tau_{top} \sim \Gamma_{top}^{-1} \simeq 5{\cdot}10^{-25}$ s, so that is approximatively 0.2 times smaller than the characteristic formation time of hadrons [7]. Therefore, instead of hadronising like the other quarks, the top quark decays almost as soon as it is produced.

With the Cabibbo–Kobayashi–Maskawa (CKM) [7] element $V_{tb} \simeq 1$, the SM top quark decays almost exclusively to a bottom quark and a W boson. If the W boson decays into leptons through $W \to l + \nu$, then, the top is classified as leptonic top. Otherwise, the W boson decays in two quarks through $W \to q + \bar{q'}$, and so, the top is classified as hadronic [8]. For the analyses shown in this thesis, only events with exactly one leptonic top quark are selected.

The top quark is produced during the LHC proton proton (p-p) collisions, mostly as particle-antiparticle pairs ($t\bar{t}$), via the strong interaction [9] notably through gluon fusion [33]. Single top production via the Weak interaction (in association with one to two quarks or a W boson) is also possible but due to its small cross section (compared to the $t\bar{t}$ cross section) [34], its contribution is not considered in this thesis.

2.5 The Higgs Boson

The Higgs Boson is the quantum excitation of the Higgs field described in the section 2.3. The Higgs model has been proposed in 1964, and ATLAS and CMS collaborations announced the observation of a Higgs-like particle in 2012 at CERN [4, 15].
Results from the combination of 7 and 8 TeV collisions data by the ATLAS group, show that the SM Higgs boson mass [10] is $m_H = \sqrt{2}\mu \sim 126.0 \pm 0.4$ (stat) $\pm$ 0.4 (sys) GeV [15, 16]. Considering sizeable cross sections, there are four major SM Higgs production modes shown in figure 2.3 such as gluon fusion, vector-boson fusion, production in association with vector bosons and production in association with top quarks. As illustrated in figure 2.4, the branching fraction of different Higgs decay modes depends exclusively on the latter Higgs mass. Yet, the Higgs boson mass measured at LHC is about 126 GeV,

[7] The formation time of hadrons is: $\tau_{had} \sim 1/\Lambda_{\text{QCD}} \sim 3 \times 10^{-24}$ s, where Λ_{QCD} is the scale at which QCD becomes non-perturbative.

[8] In the hadronic case, only W boson decays to (up,down) or (charm,strong) quarks are kinematically allowed. Considering three different color charges per quarks postulated by SM, there are a total of six hadronic and three leptonic possible modes.

[9] The cross section of $t\bar{t}$ at LHC: $\sigma_{t\bar{t}} = 242.4 \pm 1.7$ (stat.) $\pm$ 5.5 (syst.) $\pm$ 7.5 (uncert. in luminosity) $\pm$ 4.2 (uncert. in beam energy) [33].

[10] As shown in figure 2.4, the study of $H \to \gamma + \gamma$ (pink plot), $H \to Z + Z$ (black plot) and $H \to W + W$ (light-green plot) channels leads to the Higgs mass value with the best resolution allowed by the ATLAS detector. The $\gamma + \gamma$ channel has a low ratio but is the cleanest channel from backgrounds.

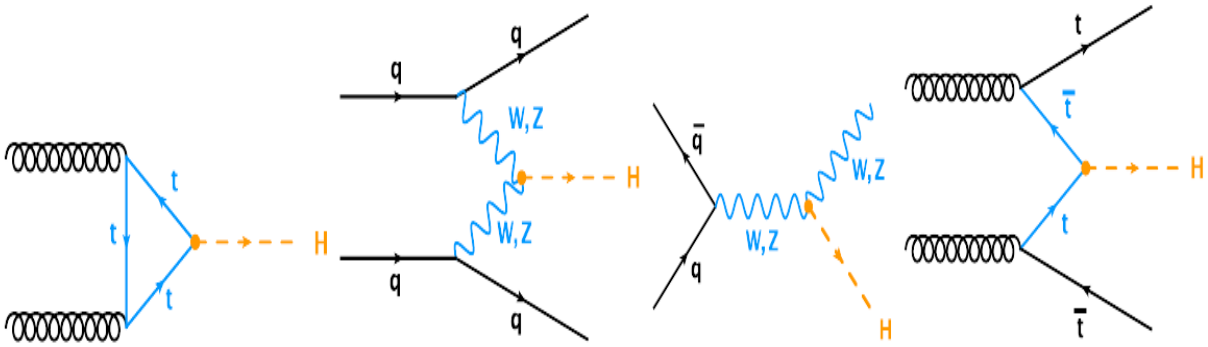

Figure 2.3: The main Higgs boson production mechanism in proton-proton collisions described by Feynman diagrams in decreasing order of the cross section from left to right: gluon fusion, vector boson fusion, associated production of vector bosons and associated production of top quarks [5].

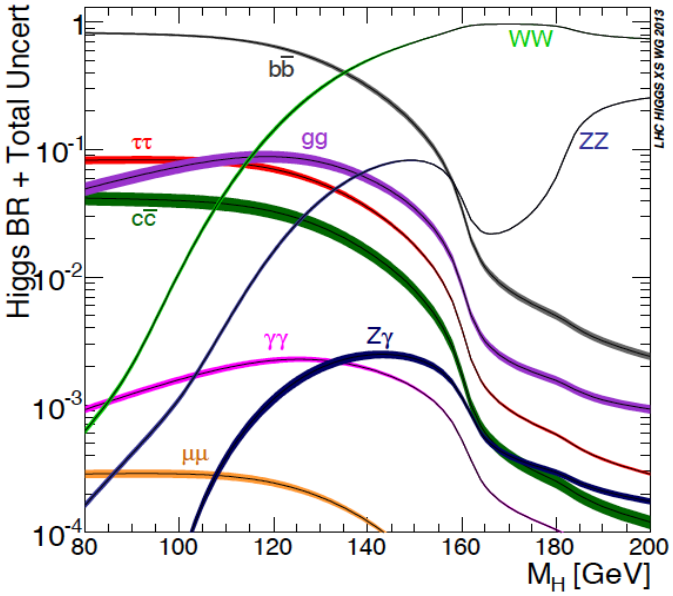

Figure 2.4: Predicted branching fractions as a function of the Higgs boson mass for different decay modes of the SM Higgs boson [6].

and decays most likely to bottom quark pairs, then, to W boson pairs. However, Z boson and photon pairs have been considered too (despite their small branching fractions). CMS and ATLAS experiments are more effective when it comes to the detection of photons and leptons with good resolution: the

QCD-multijet background suppression becomes much easier when the signal events contain isolated leptons.

Finally, all measured properties of the Higgs-like particle (mass, spin, parity and its coupling to other SM particles) lead strongly to the conclusion that this boson behaves to a good approximation as a SM Higgs boson [15, 35].

2.6 Standard Model Weaknesses

Although, the SM is able to predict a large number of phenomena and has been verified with excellent accuracy, it presents some deficiencies that could not be ignored. The main SM weakness is the leak of a description of gravity, neutrino masses, dark energy and dark matter, baryon-anti-baryon asymmetry and the hierarchy problem.

2.6.1 Quantum gravity

The only fundamental force not included in the SM is gravity, described by Einstein's general theory of relativity, as a fourth interaction force because its effects are strong only at the Planck scale $m_P = 10^{19}$ GeV where the SM is no longer valid. However, several models such as Supersymmetry, String theory and Loop Quantum Gravity attempt to unify all forces but none have been proved by experience so far.

2.6.2 Are the neutrinos really massless?

In the SM, neutrinos are left-handed and thus without a Dirac mass as mentioned in section 2.1. They do not carry electromagnetic charge nor color [11], so, their direct detection is impossible making neutrino analyses very difficult. However, the prediction of massless neutrinos is inconsistent with observations of neutrino oscillation at the Super-Kamiokande Observatory and the Sudbury Neutrino Observatory. Indeed several experiments show that a definite lepton flavor neutrino produced at a source can later be measured to have a different flavor which implies that neutrino have a non-zero mass. The seesaw mechanism considers right-handed neutrino with heavy Majorana [12] masses. As their mass is proportional to the inverse of the left-handed neutrino mass, the latter particles end up having very small masses.

[11] Neutrino interact via the weak and gravitational forces.
[12] A particle which is its own anti-particle is called Majorana.

2.6.3 What is the rest of the Universe?

The universe is composed of about 4.6% of baryonic matter, 71.4% of dark energy and 24% of dark matter, so particles which constitute 95.4% of the universe is not provided by the SM.

Cosmic microwave background observations lead to consider a form of energy, called dark energy, that permeates all space, tending to accelerate the expansion of the universe. The cosmological constant [13] proposed by Einstein or scalar fields such as quintessence [14] are two different energy candidates used to explain dark energy in Cosmology.

Interacting only with gravity, dark matter could not be observed directly but from observations: motions of galaxies (such as gravitational rotation curves in galaxies, Velocity dispersions of galaxies), Cosmic microwave background, etc. The SUSY model predicts Lightest Supersymmetric Particles (LSP) such as a stable neutralino as a possible dark matter candidate.

2.6.4 The baryon-anti-baryon asymmetry

In the universe, the imbalance in baryonic matter, composed of SM particles, and anti-baryonic matter, made of antiparticles which are distinguished from particles by their opposite charges, have been observed. This baryon asymmetry is not explained by the SM [36, 37].

2.6.5 The energy scales

On the one hand, fundamental interactions are described by the SM Gauge symmetry $SU_c(3) \times SU_L(2) \times U_Y(1)$ divided into two energy scales such as $\Lambda_{\text{QCD}} \sim 200$ MeV (for the strong coupling) and $m_W \sim 100$ GeV for EW force (spontaneous symmetry breaking) [7]. On the other hand, the Planck scale is at $m_P \sim 10^{19}$ GeV at which gravity effects become strong. The huge gap between the forces from the SM and the Planck scale is about a factor of 10^{17} and commonly called as the hierarchy problem. The grand unification is an attempt to unify these forces into a single one at the scale of $\sim 10^{15}$ to $\sim 10^{17}$ GeV. The LHC, at CERN, achieving 8 TeV (soon 14 TeV) center of mass energies, is still far from the grand unification energies.

For the time being, VLQ are an attractive scenario to address the top quark contribution to the hierarchy problem [38]. The phenomenology of the latter particles is described in section 3.5.

[13] The cosmological constant is a time-space constant energy density filling space homogeneously.
[14] In physics, quintessence is a dynamic quantity which energy density can vary in time and space.

3 Beyond the Standard Model

In section 2.6, we exposed few examples of the SM limitations and concluded that the SM is not the ultimate model of nature, but a part of a more complex model that could solve some, if not all, of the SM problems. Hence, new channels for Higgs production can arise in extensions of the SM. An attractive possibility is the Higgs production in decays of additional new heavy particles that can be produced at LHC via strong interactions.

The hierarchy problem (section 2.6.5) points out the fact that, we do not know why weak interaction is about 10^{17} stronger than gravity. It can also be considered in terms of the disparity between Higgs-boson mass and Planck scale.
Considering the SM to be valid up to a scale, called Λ_{UV}, the scalar Higgs boson mass should encounter radiative corrections from vacuum polarization diagrams. If the correction to m_H^2 (Δm_H^2) comes from a loop containing a fermion (f) with mass m_f, then, the Feynman diagram, as shown by figure 3.1, yields a correction proportional to the square of Λ_{UV}. This regulates the mass divergence as follows:

$$m_{H,phys.}^2 = m_H^2 - \Delta m_H^2 + \frac{\lambda}{4\pi^2}\Lambda_{UV}^2, \ (\lambda \text{ was defined in Equation 2.4}) \tag{3.1}$$

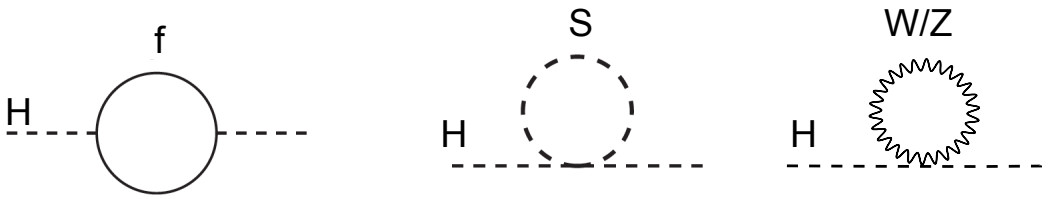

Figure 3.1: One-loop corrections to the Higgs squared mass due to ,from left to right, a Dirac fermion f, a scalar S (such as Higgs H boson), a W or Z boson [7].

The fermion could be any SM quark and lepton, but the largest correction comes from the top quark coupling [1]. If the mass divergence is not canceled by the value of Δm_H^2, and, Λ_{UV} is of the order of the m_P, as in the SM framework, then:

$$m_{H,phys.}^2 \sim 10^{32} \ \text{GeV}, \tag{3.2}$$

[1] For corrections coming from a top quark (t) coupling, the Higgs boson mass is then defined as $m_{H,phys.}^2 = m_H^2 - \Delta m_{H,t}^2 + \frac{\lambda}{4\pi^2}\Lambda_{UV}^2$. From the coupling, we have: $\Delta m_H^2 \sim \lambda^2$ and $m_H^2 \sim \lambda^2$.

e.g., many orders of magnitude larger than the experimentally measured value [2] , which is coherent with the SM predictions [15, 16]. Therefore, quantum gravity effects become large, and, the space-time notion loses its meaning. Otherwise, the Λ_{UV} value should be smaller, so at the scale of energy in which SM is no longer valid: we are, then, in the BSM area, also called new physics.

Choosing a value of m_H^2 much smaller than Δm_H^2 leads to a scale of $\Lambda_{UV} \sim \mathcal{O}(1)$ TeV, from which sets the lower limit of new physics reached by the LHC energy scale. In these limits, the most popular new physics models propose new partners that couple to Higgs and cancel the divergent correction. SUSY proposes supersymmetric partners associated to SM particles. Consequently, the loop correction to the Higgs-boson mass cancels out naturally [39]. Notably, a few Exotics models introduce heavy vector-like particles, such as VLQ top, with a mass of few TeV that can affect the Higgs coupling, and thus, reduce the top-quark loop contribution. The latter VLQ top should have the same quantum numbers as SM top quark, and, couple to the Higgs boson in the same way as does the SM top quark. These heavy VLQ have been predicted by several Exotics models such as:

- Little Higgs (LH) models,
- Extra Dimensions models,
- Effective theory of the Heavy gluon and the top partners.

The little Higgs models are briefly described in section 3.1, while an Extra Dimensions model is presented in section 3.2, to set a new sector in which new particles arise, and, the Higgs boson is a composite Nambu-Goldstone-Boson(NGB). Among the latter new particles, particular attention is given to the lightest Kaluza-Klein excitation of gluon (g_{KK}) and VLQ. Then, are introduced an effective theory of heavy gluon (g_{KK}) and the top partners in section 3.3. Finally, the phenomenology of heavy gluon and VLQ top will be detailed in section 3.4 and section 3.5, respectively.

3.1 Little Higgs

For energies below a cutoff scale of about Λ_{LH} ~10 TeV, Little Higgs models introduce the SM gauge bosons along with pairs of VLQ. These models contain only three parameters which are related to each other. When the Little Higgs cutoff scale (Λ_{LH}) is at the order of

$$\Lambda_{\text{Weak}} \sim 4\pi v \sim (4\pi)^2 m_{\text{Weak}}, \tag{3.3}$$

[2] $m^2_{H,phys.} \sim [126 \text{ GeV}]^2$.

a vev of v breaks a global symmetry producing Goldstone bosons, of which one will be the Higgs boson [40, 41]. Then, follows a second symmetry breaking at the electroweak scale m_{Weak} (=246 GeV at which SM particles lie). The Higgs boson becomes, then, a pseudo-Goldstone-Boson (PGB) [42].

On one hand, the PGB Higgs has a light and stable (free of radiation correction) mass. On the other hand, the new VLQ masses are at the TeV scale. Considering the top quark loop (for its large Yukawa-coupling to Higgs boson) and its partner VLQ top, T, the SM quark doublet is extended to triplets under Little Higgs models, like $\psi \equiv (t,\ b,\ T)$ [42, 43].

Although Little Higgs models are such a simple way to extend the SM, from now, we will focus on the Extra dimensions model which is indeed more complex, but predicts heavy gluons, VLQ top and composite Higgs in a elegant way.

3.2 Extra dimensions

The extra dimensions model is a hypothesis, proposed by Kaluza and Klein [44], of electromagnetic and gravitational field unification in a higher dimensional field component. They considered a five-dimensional theory in which space is a product of the $4D$ Minkowski space with a circle of radius R, noted $M^4 \bigotimes S^1$. The space is, then, seen as a $5D$ cylinder of radius R, and, the fifth dimension is periodically defined as $x^5 \sim x^5 + 2\pi R$ [8]. During this process called compactification [45], an infinite tower of fields is generated in which masses $m^2 = n^2/R^2$ are quantized via $n \in \mathbb{Z}$ in periodic dimensions. At small energies (compared to R^{-1}) the physics is exclusively four-dimensional (corresponds to the world as we know), while at high energies the tower of Kaluza-Klein (KK) particles come into play, in five-dimensional physics.

Since these KK particles have not been detected up to now, at the collisions energies up to TeV, their masses are thought to be high (greater than TeV) setting a constraint on the scale of $R \leq 10^{-21}$ cm. Nowadays, these dimensions are too small to be detected in any actual direct experiment.

3.2.1 Kaluza-Klein theories and Arkani-Dimopoulos-Dvali restrictions

Arkani, Dimopoulos and Dvali (ADD) [46] have proposed, then, that in the extra dimensions only gravity propagates (and not in SM field) so the radius scale is fixed by gravitation to $R_{\text{Bulk}} \leq 10^{-1}$ cm which is easily detectable. Moreover, the ADD scenario provides the argument according to which the gravity force is diluted in the large volume of extra dimensions. This way, the hierarchy between the Planck scale and the weak interaction, is only apparent: the hierarchy problem is naturally gone. Still,

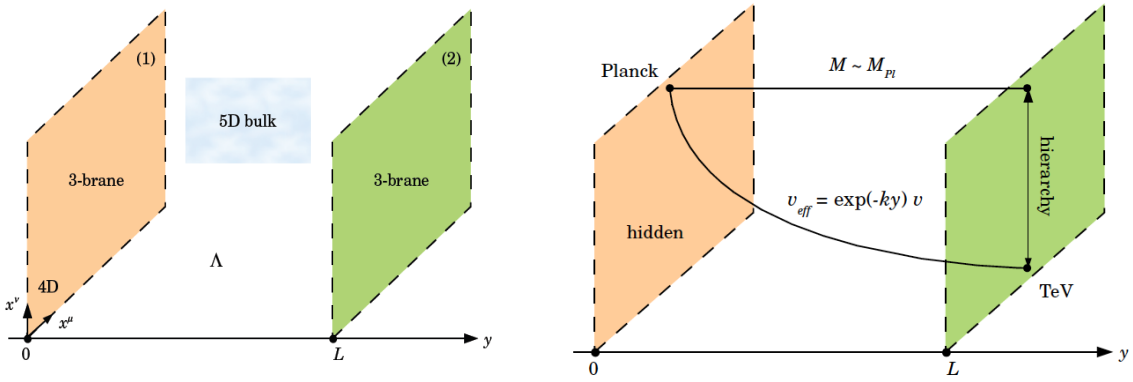

Figure 3.2: Left side: the Randall-Sandrum setup with two $4D$-branes enclosing an AdS_5 bulk of length L [8]. Right side: the RS setup with the generation of an exponential hierarchy ν_{eff} across the AdS_5 bulk: gravity scale in the Planck brane is dropped to the weak scale in the TeV brane [8].

a new problem comes to light concerning the scale R_{ADD} being 10^{20} times bigger than its natural scale from the original KK model.

3.2.2 The Randall-Sundrum model

The Randall-Sandrum (RS) model [8, 19, 47] came just after the ADD model, as a new solution to the Hierarchy Problem. The model involves one extra dimension compactified on an orbifold, $S^1/\mathbb{Z}_2$ of radius R, with $-\pi R \leq y \leq \pi R$. At the orbifold fixed points $y = 0$ and $y = \pi R$, a 3-branes enclose a $5D$ bulk of the size of $L = 2 \times R$, where R is considered to be the extra dimension parameter or the warp factor. The latter $5D$ bulk is characterized by a $5D$ cosmological constant Λ_{Bulk} which is chosen to be negative, so the bulk becomes a $5D$ anti-de Sitter space, noted AdS_5. In other words, the $5D$ bulk is assumed to be a non-factorizable geometry based on a slice of AdS_5 space (more detail can be found in section 3.2.3). Furthermore, each of the two $4D$ spaces is flat and static with a $4D$ cosmological constant vanished by the Λ_{Bulk}. The resulting warped metric is as followed [8]:

$$ds^2 = e^{-2A(y)}\eta_{\mu\nu}dx^\mu dx^\nu + dy^2, \tag{3.4}$$

where $\eta_{\mu\nu} = \text{diag}(-1, 1, 1, 1)$ is the $4D$ Minkowski metric, $e^{-2A(y)}$ is the warp factor and $A(y) = \pm ky$.

The general and basic view of the RS model is as follows:

- The first brane at $y = 0$ is called the Planck brane, ultraviolet (UV) or invisible boundary. While the second one is called TeV, InfraRed (IR) or visible brane [19].
- The SM particles live in the TeV brane but gravity is located on the Planck brane.
- The $5D$ bulk is in a AdS_5 space and only populated by gravity.

Along the AdS_5 bulk (as illustrated in the right side of figure 3.2) the vacuum expectation value ν is exponentially suppressed according to:

$$\nu_{\text{eff}} = e^{-\kappa L}\nu, \qquad \text{where } \kappa \text{ is a constant of the order of Planck scale.} \tag{3.5}$$

This exponential suppression results in some very nice consequences listed below:

- Exponential suppression of all mass parameters in the TeV brane.
- A field on the TeV brane, with a mass m_0, will appear [3] to have a physical mass of $m = e^{-\kappa R\pi}m_0$.
- So to Higgs, from the Planck brane with a mass of m_P, corresponds a physical Higgs in the TeV brane which mass is warped down to weak scale. The hierarchy problem is naturally solved with elegance.
- From $m_{\text{Weak}} \simeq 10^{-16}\ m_P$, the size of the extra dimension arises as $kL \simeq ln10^{16} \simeq 37$.
- This particular extra-dimensions model, in which TeV scales are generated from fundamental scales of order of m_P via the latter geometrical exponential factor, is so-called warped extra dimensions model.

Finally, the relations between the modes of the $5D$ bulk and the fields from the $4D$ boundaries are very well explained in the AdS_5/CFT correspondence model. Section 3.2.3 is devoted to the latter duality.

3.2.3 Anti-de Sitter and Conformal Field Theory correspondence

The Anti-de Sitter spaces (AdS) are used in quantum gravity theories such as String theory or M-theory. On the other hand, the Conformal Field Theory (CFT) is similar to Yang-Mills theories and describe elementary particles [48–50].

[3] As a consequence, one can start to introduce the term of duality but let us keep things simple and talk about it a little bit later as from the end of section 3.2.2.

There is a correspondence between Anti-de Sitter and Conformal Field Theory denoted as AdS/CFT. It is a duality between the $4D$ branes which shelters the strongly coupled fields and the AdS_5 bulk where the weakly coupled gravitational modes live [51]. The duality is then qualified as a gauge/gravity duality.

Let us imagine a graviton [4] travelling from Planck brane toward the TeV brane through the AdS bulk (in figure 3.2, the graviton travels from the orange brane to green brane). The Planck brane has an observer named Obs_{Pl} while the TeV brane has a observer named Obs_{TeV} and both observers watch the graviton moving along the bulk. The observer Obs_{Pl} sees the graviton traveling during a time $\sim$ TeV^{-1} before reaching TeV brane and producing SM particles. During the same time, Obs_{TeV} sees the graviton growing by size as it gets closer to him. At the time TeV^{-1}, the Obs_{TeV} sees the graviton hitting the brane, breaking the CFT symmetry and producing standard particles [51]. This AdS/CFT correspondence is also called holography in some physics papers.

3.2.4 Kaluza-Klein excitations

Originally the Randall-Sundrum scenario described in Section 3.2.2, predicts that the SM particles are confined to one of the 4-branes. However, considering the possibility that fermions and bosons can travel through the AdS_5 space is very helpful when it comes to solving several weaknesses of the SM such as the hierarchy of the fermion masses and the gauge coupling unification [52]. Therefore, to all SM fields correspond Kaluza-Klein excitations in the form of Kaluza-Klein mass towers. The Kaluza-Klein towers of state appear then above each doublet or singlet field of the SM. In this perspective, the new heavy particles arise as composite states of a new sector [9, 21, 52]. Among which, a particular focus are given to:

- the lighter Kaluza-Klein excitation of the gluon called heavy gluon and denoted as g_{KK},
- the composite Higgs as a pseudo Nambu-Goldstone boson [53],
- the composite vector-like fermions, especially the vector-like top quarks.

From now, we choose a framework of an effective theory [9] that considers only the lowest-lying resonances [5] which is described in the section 3.3. In this scenario, from a new strong sector arise new heavy particles which are composite and coupled to the SM ones via linear mixing terms. The Higgs Boson [53] is a bound state of the new dynamics and has direct couplings only to the composite fermions. Finally, we will study only the composite quarks in this thesis.

[4] The graviton is a massless hypothetical elementary particle that mediates the force of gravitation in the framework of quantum field theory.

[5] This effective theory is easier to build than a theory with a full set of particles and interactions.

3.3 Effective theory of the Heavy gluon and the top partners

To build the model we need two sectors enclosing an AdS_5 space time, as mentioned in section 3.2.2. First, the elementary sector (the TeV brane) is where all the SM particles, the Higgs boson excepted, live under the $SU(3)_c \times SU(2)_L \times U(1)_Y$ fields gauge [6]. Then, comes the composite sector (Planck brane) where composite particles such as the Higgs boson, transform under a $SU(3)_c \times O(4) \times U(1)_X$ global symmetry with $O(4) \supseteq SU(2)_L \times SU(2)_R$ so $SU(2)_L$ and $SU(2)_R$ are exchanged. The composite Higgs Field is defined as:

$$\mathcal{H} = (1,2,2)_0 = \begin{bmatrix} \Phi_0^\dagger & \Phi^+ \\ -\Phi^- & \Phi_0 \end{bmatrix}. \tag{3.6}$$

The composite and elementary sectors enclose the mixing sector (the AdS_5 bulk) where heavy particles such as the SM top and heavy gluon (g_{KK}) live and where the TeV brane quarks can travel. The heavy gluon transforms as $(8,1,1)_0$ under $SU(3)_c \times SU(2)_L \times SU(2))_R \times U(1)_X$. Also a set of new heavy particles arises as composite states of a new QCD like, strong sector. The new composite particles are characterized by their couplings to the SM particles and the fact that they exist under singlet or doublet composite vector-like forms of quarks as follows:

$$\begin{aligned} \mathcal{Q} = (3,2,2)_{2/3} &= \begin{bmatrix} T & T_{5/3} \\ B & T_{2/3} \end{bmatrix}, \ \tilde{T} = (3,1,1)_{2/3}. \\ \mathcal{Q}' = (3,2,2)'_{-1/3} &= \begin{bmatrix} B_{-1/3} & T' \\ B_{-4/3} & B' \end{bmatrix}, \ \tilde{B} = (3,1,1)_{-1/3}. \end{aligned} \tag{3.7}$$

Three sectors mean three Lagrangians the sum of which leads to the following global Lagrangian:

$$\mathcal{L} = \mathcal{L}_{elementary} + \mathcal{L}_{composite} + \mathcal{L}_{mixing} \tag{3.8}$$

The first element of the global Lagrangian defines the couplings between the SM particles in the TeV sector. The latter Lagrangian is naturally called $\mathcal{L}_{\text{elementary}}$ and defined as follows:

[6] Where $Y = T_R^3 + X$ links hyper-charge with isospin and charge. Y stands for Hypercharge, $T^3_{L/R}$ for third component of isospin under the $SU(2)_{L/R}$ groups. For instance, $T_L^3(t_L) = +1/2$, $T_L^3(b_L) = -1/2$ (they are the upper and lower components of a doublet) while $T_L^3(t_R) = 0$ (it is a singlet of $SU(2)_L$). X is the charge under the $U(1)_X$ group. The electric charge that is as in the SM ($Q = T_L^3 + Y$).

$$\mathcal{L}_{elementary} = -\frac{1}{4\varepsilon_{el3}^2} G_{\mu\nu} G^{\mu\nu} + q_L^{-i} i \not{D} q_L^i + u_R^{-i} i \not{D} u_R^i + \bar{d_R^i} i \not{D} d_R^i \tag{3.9}$$

where ε_{el3} is the gauge coupling constant, D_μ is covariant under $SU(3)_c$, the index $i = 1, 2, 3$ stands for the three SM families, index L and R stand for left and right-handed quarks so we can say $q_L^3 \equiv (t_L, b_L)$, $u_R^3 \equiv t_R$ and $d_R^3 \equiv b_R$.

Recall that, the global Lagrangian $\mathcal{L}$ should help with the description of the couplings between SM quarks fields, composite Higgs Fields and VLQ fields (so the AdS/CFT correspondence) on the one hand and flavor hierarchy on the other hand. However, we consider in this particular model that the strong sector is flavor anarchic so the full spectrum of quark masses and the CKM matrix ensue from three families of heavy quarks and three sets of mixing terms $\{\Delta_{L1}^i, \Delta_{L2}^i, \Delta_{tR}^i, \Delta_{bR}^i\}$, one for each SM flavor i. Furthermore, earlier studies [54–56] show that the mixing parameters of the light SM quarks ($i = 1, 2$) are so small that their effects in the heavy gluon study can be neglected.

Under these circumstances, only the third generation of quarks (SM and vector-like) remain in the Lagrangian. Hence, the third term of the global Lagrangian describes the couplings between the SM top and bottom quark fields and the composite fields via the third generation mass mixing terms. The resulting Lagrangian $\mathcal{L}_{\text{mixing}}$ is elegantly shown by equation 3.10:

$$\begin{aligned}\mathcal{L}_{mixing} =& \frac{\bar{m}_{g_{KK}}^2}{2\varepsilon_{*3}^2}(G_\mu - G_\mu^*)^2 - \Delta_{L1}\bar{q}_L^3(T, B) - \Delta_{L2}\bar{q}_L^3(T', B') \\ & - \Delta_{tR}\bar{t}_R\tilde{T} + \text{h.c.}\end{aligned} \tag{3.10}$$

The second component is the composite part of the global Lagrangian called $\mathcal{L}_{\text{composite}}$ (equation 3.11) used to describe the AdS/CFT correspondence of the Higgs Fields toward the composite quarks and the SM quarks (of the third family) through the SM Yukawa couplings (Y_{*U} and Y_{*D}) (described in detail in ref [9] appendix A).

$$\begin{aligned}\mathcal{L}_{composite} =& -\frac{1}{4\varepsilon_{*3}^2} G_{*\mu\nu} G^{*\mu\nu} + \frac{1}{2} Tr[\partial_\mu \mathcal{H}^\dagger \partial^\mu \mathcal{H}] - V(\mathcal{H}^\dagger \mathcal{H}) \\ & + Tr\{\bar{\mathcal{Q}}(i\not{\partial} - \not{G}^* - \bar{m}_{\mathcal{Q}})\mathcal{Q}\} + \bar{\tilde{T}}(i\not{\partial} - \not{G}^* - m_{\tilde{T}})\tilde{T} \\ & + Tr\{\bar{\mathcal{Q}}'(i\not{\partial} - \not{G}^* - \bar{m}_{\mathcal{Q}'})\mathcal{Q}'\} + \bar{\tilde{B}}(i\not{\partial} - \not{G}^* - m_{\tilde{B}})\tilde{B} \\ & - Y_{*U} Tr\{\bar{\mathcal{Q}}\mathcal{H}\}\tilde{T} - Y_{*D} Tr\{\bar{\mathcal{Q}}\mathcal{H}\}\tilde{B} + \text{h.c.}\end{aligned} \tag{3.11}$$

where $V(\mathcal{H}^\dagger \mathcal{H})$ is the Higgs potential, $\mathcal{Q} = (T, B)$, $\mathcal{Q} = (T', B')$ and ε_{*3} is the gauge coupling.

Following the Lagrangian parameters, we can see that the number of free parameters of the Lagrangian is up to thirteen by counting one for the Higgs mass, one for the self-couplings from the Higgs

potential, four for composite masses in the fermionic sector ($\bar{m}_Q$, $\bar{m}'_Q$, $\bar{m}_{\tilde{T}}$ and $\bar{m}_{\tilde{B}}$), one for heavy gluon mass ($\bar{m}_{g_{KK}}$), four for mixing terms mass (Δ_{L1}, Δ_{L2}, Δ_{tR}, Δ_{bR}), two for composite Yukawa couplings (Y_{*U} and Y_{*D}) and two gauge couplings (ε_{el3} for elementary case and ε_{*3} for the mixing one).

We consider the strong sector to be Charge Parity [57] and flavor [58–61] invariant so the heavy gluon can have a mass of few TeV [7]. Finally, the flavor bounds are simplified by some mechanism and we consider that the collisions at LHC achieve enough energy to produce the heavy masses without any restrictions [9]. Earlier studies on the model [62] show that the strong sector is invariant under P_{LR} (for left and right chiralities) leading to the fermionic representations of equation 3.7 and to the following approximations:

$$\Delta_{L2} \ll \Delta_{L1}, \tag{3.12a}$$

$$\Delta_{tR} \sim \Delta_{bR}. \tag{3.12b}$$

In order to diagonalize the global Lagrangian defined by the equation 3.8, one should consider that the first and second families of SM quarks do not mix with the composite quarks and can, thus, be simply identified by their corresponding SM states. As for the third family of the SM quarks, a field rotation from the mixing basis to the mass eigenstate basis is taken in consideration before the Electroweak Symmetry Breaking (for details see appendix A of [9]). The fermionic rotation between SM quarks and the composite quarks are thus parametrized by eight parameters such as:

- Four mixing angles in the fermionic sector:

$$\tan\varphi_{tR} = \frac{\Delta_{tR}}{\bar{m}_{\tilde{T}}}, \quad \tan\varphi_{bR} = \frac{\Delta_{bR}}{\bar{m}_{\tilde{B}}}, \quad \tan\varphi_L = \frac{\Delta_{L1}}{\bar{m}_{\mathcal{Q}}}, \quad s_2 = \frac{\Delta_{L2}}{\bar{m}_{\mathcal{Q}'}}\cos\varphi_L \tag{3.13}$$

  where $\sin\varphi_{tR}$, $\sin\varphi_{bR}$ and $\sin\varphi_L$ denote the degree of compositness of t_R, b_R and $(t_R,\ b_R)$, respectively.

- Two mixing angles in the gauge sector:

$$\tan\theta_3 = \frac{\varepsilon_{el3}}{\varepsilon_{*3}}, \quad \varepsilon_3 = \varepsilon_{el3}\cos\theta_3 = \varepsilon_{*3}\sin\theta_3, \tag{3.14}$$

  where ε_{el3} and ε_{*3} stand for the elementary and the composite couplings, respectively, and determine the rotation angle θ_3 and the SM gauge coupling ε_3.

[7] In this scenario the heavy gluon phenomenology remains qualitatively unchanged.

- Two mixing parameters:

$$s_3 = \frac{\Delta_{L2}\bar{m}_{\mathcal{Q}'}}{\Delta_{L1}^2 + \bar{m}_{\mathcal{Q}}^2 - \bar{m}_{\mathcal{Q}'}^2}\sin\varphi_L, \quad s_4 = \frac{\Delta_{L2}\Delta_{L1}}{\Delta_{L1}^2 + \bar{m}_{\mathcal{Q}}^2 - \bar{m}_{\mathcal{Q}'}^2}. \tag{3.15a}$$

The physical masses rise as:

$$m_{\tilde{T}} = \frac{\bar{m}_{\tilde{T}}}{\cos\varphi_{tR}}, \quad m_{\tilde{B}} = \frac{\bar{m}_{\tilde{B}}}{\cos\varphi_{bR}}, \quad m_T = m_B = \frac{\bar{m}_{\mathcal{Q}}}{\cos\varphi_L}, \quad m_{T'} = m_{B'} \simeq \bar{m}_{\mathcal{Q}'}, \tag{3.16a}$$

$$m_{T_{5/3}} = m_{T_{2/3}} = m_T\cos\varphi_L, \quad m_{B_{-4/3}} = m_{B_{-1/3}} = m_{T'}, \tag{3.16b}$$

$$m_{g_{KK}} = \frac{\bar{m}_{g_{KK}}}{\cos\theta_3}. \tag{3.16c}$$

The number of free parameters of the global Lagrangian (eq. 3.8) is then reduced to thirteen.

After the Electroweak Symmetry Breaking, the SM quarks (bottom and top) acquires a mass and the VLQ masses from equations 3.16a and 3.16b get corrections of order $(\nu Y_*/\bar{m})^2$ where $\nu = 246$ GeV is the electroweak scale. From now on, we assume $r \equiv \nu Y_*/\bar{m} << 1$ so all quantities are expressed at leading order in r as follows:

- SM top and bottom quarks mass:

$$m_t = \frac{\nu}{\sqrt{2}}Y_{*U}\sin\varphi_L\sin\varphi_{tR}, \quad m_b = \frac{\nu}{\sqrt{2}}Y_{*D}s^2\sin\varphi_{bR} \tag{3.17}$$

- As the values of the SM top and bottom masses and the SM gauge coupling ε_3 are set experimentally with high precision [4], the three following parameters are set as:

$$Y_{*U} = Y_{*D} = Y_*, \quad \sin\varphi_{bR} = \sin\varphi_L, \quad m_{T'} = m_{\tilde{B}} = m_{\tilde{T}}. \tag{3.18}$$

Therefore, only five free parameters remain in the global Lagrangian such as the mixing angles $\sin\varphi_L$, $\sin\varphi_{tR}$ and $\tan\theta_3$, VLQ top mass ($m_{\tilde{T}}$) and heavy gluon mass ($m_{g_{KK}}$). Alternatively, one can also trade the two mixing angles $\sin\varphi_L$ and $\tan\theta_3$ for the two couplings parameters Y_* and ε_{*3}.

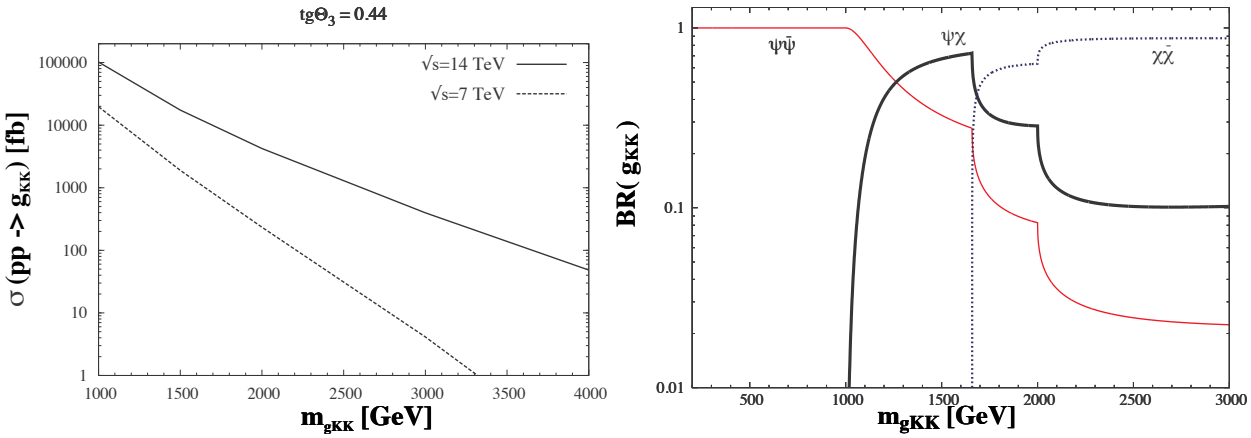

Figure 3.3: Left plot: Cross section of the Drell-Yan production of heavy gluons at LHC as a function of the heavy gluon mass [9], for $\tan\theta_3 = 0.44$ setting the composite coupling to $\varepsilon_{*3} = 3$. For a different value of $\tan\theta_3$, the heavy gluon cross section scales as $(\tan\theta_3)^2$. Right plot: Branching ratios for the decay of heavy gluons [9] to two SM quarks ($\psi\bar{\psi}$ in the red line), two heavy quarks ($\chi\bar{\chi}$ in the full black line) and one SM plus one heavy quark ($\psi\bar{\chi} + \chi\bar{\psi}$ in the black dotted lines), as a function of $m_{g_{KK}}$. The plot is done setting the other parameters to the following reference values: $m_{\tilde{T}} = 1$ TeV and $\tan\theta_3 = 0.44$, $\sin\varphi_{tR} = 0.6$, $Y_* = 3$.

3.4 The phenomenology of Heavy gluon

At LHC, heavy gluons (g_{KK}) would be mainly produced via the Drell-Yan process $q\bar{q} \to g_{KK}$. The left plot of figure 3.3 shows the heavy gluon cross sections for collisions of 7 TeV and 14 TeV for a reference mixing angle of $\tan\theta_3 = 0.44$ which corresponds to a composite coupling of $\varepsilon_{*3} = 3$ [9]. For different values of $\tan\theta_3$ the cross section scales as $(\tan\theta_3)^2$.
Considering the evolution of the cross sections versus heavy gluons mass, from 8 TeV collisions to be somewhere between the ones from 7 and 14 TeV (so in the area between the dotted line and the full line of the left plot of figure 3.3), the cross section of the heavy gluons of mass of 1.0 TeV is in the window of [20,100] pb while the cross section of a 2.0 TeV heavy gluon is greater than 0.2 pb but lower than 5 pb.

As soon as it is produced, the heavy gluon decays via one of three different channels according to the kinematic conditions. The wise choice of channels and the study of the final products will allow us to reconstruct the heavy gluon mass. To determine the channels, one need to look at the heavy gluon coupling force with SM particles and VLQ, then its decay rate in each channel.

The heavy gluon couples to the light SM quarks (denoted as $q = u,\ d,\ c,\ s$) with strength of $\varepsilon_{g_{KK,qq}} = -\varepsilon_3 \tan\theta_3$. However, its couplings to the SM top and bottom quark (denoted as $\psi = t_L,\ b_L,\ t_R,\ b_R$), and to the VLQ ($\chi = T,\ B, \tilde{T}, \tilde{B}$) are much stronger and measured by $\varepsilon_{g_{KK,\psi\psi}}$, $\varepsilon_{g_{KK,\chi\psi}}$ and $\varepsilon_{g_{KK,\chi\chi}}$, respectively, as follows:

$$\varepsilon_{g_{KK,\psi\psi}} = \varepsilon_3(\sin^2\varphi_\psi \cot\theta_3 - \cos^2\varphi_\psi \tan\theta_3), \quad \text{where} \quad \sin\varphi_{tL} = \sin\varphi_{bL} \equiv \sin\varphi_L \tag{3.19a}$$

$$\varepsilon_{g_{KK,\chi\psi}} = \varepsilon_3 \frac{\sin\varphi_\psi \cos\varphi_\psi}{\sin\theta_3 \cos\theta_3}, \quad \text{where} \quad \chi\psi = Tt_L,\ Bb_L,\ \tilde{T}t_R,\ \tilde{B}b_R \tag{3.19b}$$

$$\varepsilon_{g_{KK,\chi\chi}} = \varepsilon_3(\cos^2\bar{\varphi}_\chi \cot\theta_3 - \sin^2\bar{\varphi}_\chi \tan\theta_3). \tag{3.19c}$$

where $\sin\bar{\varphi}_{T_L} = \sin\bar{\varphi}_{B_L} \equiv \sin\varphi_L$, $\sin\bar{\varphi}_{\tilde{T}_R} \equiv \sin\varphi_{tR}$, $\sin\bar{\varphi}_{\tilde{B}_R} \equiv \sin\varphi_{bR}$ and $\sin\bar{\varphi}_\chi = 0$ for any other VLQ.

In this analysis, we will consider only the $SU(2)$ doublet T=(3, 2, 2) (left chirality) and in the $SU(2)$ singlet $\tilde{T}$=(3, 1, 1) (right chirality). Both particles are of a charge of 2/3 and are commonly called Vector-like Top (VLQ top denoted as T).

The first kinematic scenario is the production of a light-heavy gluon with a mass of $m_{g_{KK}} \lesssim m_{\tilde{T}}$ so its decay to a vector-like top is forbidden. The heavy gluon decays, then, to two SM quarks with the decay rates of:

$$\Gamma\left(g_{KK} \to q\bar{q}\right) = \frac{\alpha_3}{6} m_{g_{KK}} \tan^2\theta_3\,, \quad q = \ u,\ d,\ c, s, \tag{3.20}$$

$$\Gamma\left(g_{KK} \to \psi\bar{\psi}\right) = \frac{\alpha_3}{12} m_{g_{KK}} \left(\sin^2\varphi_\psi \cot\theta_3 - \cos^2\varphi_\psi \tan\theta_3\right)^2, \psi = \ t_L,\ b_L,\ t_R,\ b_R\,. \tag{3.21}$$

The top degrees of compositness $\sin_{\varphi_{tR}} \sin_{\varphi_L}$ and the value of $\tan_{\theta_3}$ will support the decay into a specific channel. For example, for small values of mixing angle, $\tan_{\theta_3} = 0.2$ (so $\varepsilon_{el3} \ll \varepsilon_{*3}$), large top degrees of compositness $\sin_{\varphi_{tR}} = 1$ and $Y_* = 3$, the heavy gluon would decay mostly in $t\bar{t}$ with a branching ratio of $BR(g_{KK} \to t\bar{t}) = 0.98$. On the other hand, if $\tan_{\theta_3} = 0.44$, $\sin_{\varphi_{tR}} = 0.6$ and $Y_* = 3$, then, we get a large branching ratio to pairs of light quarks (as shown in the right plot of figure 3.3 in red): $BR(g_{KK} \to t\bar{t}) = 0.18$ and $BR(g_{KK} \to q\bar{q}) = 0.69$ [9].

The second scenario is the production of a heavy gluon, so massive ($m_{g_{KK}} \gtrsim 2\ m_{\tilde{T}}$) that it would decay into two VLQ top with the decay rates of:

$$\begin{aligned}\Gamma\left(g_{KK} \to \chi\bar{\chi}\right) = \frac{\alpha_3}{12} m_{g_{KK}} \Bigg\{ &\left[\left(\cos^2\bar{\varphi}_\chi \cot\theta_3 - \sin^2\bar{\varphi}_\chi \tan\theta_3\right)^2 + \cot^2\theta_3\right]\left(1 - \frac{m_\chi^2}{m_{g_{KK}}^2}\right) \\ &+ 6\left(\cos^2\bar{\varphi}_\chi \cot^2\theta_3 - \sin^2\bar{\varphi}_\chi\right)\frac{m_\chi^2}{m_{g_{KK}}^2}\Bigg\}\sqrt{1 - 4\frac{m_\chi^2}{m_{g_{KK}}^2}}\,.\end{aligned} \tag{3.22}$$

A very nice illustration is given by the dotted blue line of right figure 3.3. The lowest and highest thresholds are at $m_{g_{KK}} = 2\, m_{\tilde{T}} \cos\varphi_L \sim 1.66$ TeV and $m_{g_{KK}} = 2\, m_{\tilde{T}} \sim 2$ TeV, respectively. However, the large jet multiplicity of the heavy gluon decay channels makes its discovery very challenging for the collisions of 8 TeV.

The last scenario is when the kinematic conditions allow the decay of the heavy gluon into a vector-like top in association with a SM quark. Since the latter SM quark should have the same quantum number as the vector-like top under $SU(2)_L \times U(1)_Y$, the partner should be a SM top quark. In this case, each of the heavy-light topologies has a sizeable branching ratio in a large range of heavy gluon masses above $m_{\tilde{T}}$ and below $2m_{\tilde{T}}$ where the heavy-heavy topology is forbidden. The decay rates are thus mentioned below:

$$\Gamma(g_{KK} \to \chi\bar{\psi} + \psi\bar{\chi}) = \frac{\alpha_3}{6} m_{g_{KK}} \frac{\sin^2\varphi_\psi \cos^2\varphi_\psi}{\sin^2\theta_3 \cos^2\theta_3} \left(1 - \frac{m_\chi^2}{m_{g_{KK}}^2}\right)\left(1 - \frac{1}{2}\frac{m_\chi^2}{m_{g_{KK}}^2} - \frac{1}{2}\frac{m_\chi^4}{m_{g_{KK}}^4}\right), \quad (3.23)$$

where $\chi = (T,\ \tilde{T})$, $\psi = (t_R,\ t_L)$ and $\chi\psi = Tt_L,\ \tilde{T}t_R$.

Therefore, during this analysis, we will consider the production of heavy gluons with a mass between 1 and 2.5 TeV (due to their large cross section at 8 TeV collisions) that decay into a VLQ top in association with a SM top quark (chosen ($m_{g_{KK}}$,m_T) are listed in section 5.2). In this scenario, the kinematics do not allow pair production of VLQ top.
As soon as they are produced, both SM and VLQ top quarks will decay into lighter particles. The SM top quark decays through the electroweak interaction into a W boson and a bottom quark (almost 100% of the time) [8]. Then, the W boson decays into two jets or one lepton and its associated neutrino with the branching ratio of $BR(W) \to q\bar{q} = 0.6760 \pm 0.0027$, $BR(W) \to e^+\nu_e = 0.1075 \pm 0.0013$, $BR(W) \to \mu^+\nu_\mu = 0.1075 \pm 0.0015$ and $BR(W) \to \tau^+\nu_\tau = 0.1125 \pm 0.0020$ (for electrons, muons and tauons respectively) [4]. For simplicity, we will consider that the latter W boson decays into a muon or an electron (and its neutrino). Next section 3.5, is dedicated to the VLQ top decays.

[8] The decay of the top quark into strange or down quarks are rare because of their small CKM elements.

3.5 The phenomenology of vector-like top quark

With a Yukawa coupling, the VLQ top decays mostly to one boson (W, Z boson or a composite Higgs H) and one SM top or bottom quark. The decay rates into the three possible channels are:

$$\Gamma\left(\chi \to W_L \psi\right) = \frac{\lambda_{W\chi}^2}{32\pi} m_\chi \left[\left(1 + \frac{m_\psi^2 - m_W^2}{m_\chi^2}\right)\left(1 + \frac{m_\psi^2 + 2m_W^2}{m_\chi^2}\right) - 4\frac{m_\psi^2}{m_\chi^2}\right] \times \sqrt{1 - 2\frac{m_\psi^2 + m_W^2}{m_\chi^2} + \frac{\left(m_\psi^2 - m_W^2\right)^2}{m_\chi^4}} \tag{3.24}$$

$$\Gamma\left(\chi \to Z_L \psi\right) = \frac{\lambda_{Z\chi}^2}{64\pi} m_\chi \left[\left(1 + \frac{m_\psi^2 - m_Z^2}{m_\chi^2}\right)\left(1 + \frac{m_\psi^2 + 2m_Z^2}{m_\chi^2}\right) - 4\frac{m_\psi^2}{m_\chi^2}\right] \times \sqrt{1 - 2\frac{m_\psi^2 + m_Z^2}{m_\chi^2} + \frac{\left(m_\psi^2 - m_Z^2\right)^2}{m_\chi^4}} \tag{3.25}$$

$$\Gamma\left(\chi \to H \psi\right) = \frac{\lambda_{H\psi}^2}{64\pi} m_\chi \left(1 + \frac{m_\psi^2}{m_\chi^2} - \frac{m_H^2}{m_\chi^2}\right) \sqrt{\left(1 - \frac{m_\psi^2}{m_\chi^2} + \frac{m_H^2}{m_\chi^2}\right)^2 - 4\frac{m_H^4}{m_\chi^4}}\,. \tag{3.26}$$

where [9]:

$$\lambda_{WT} = 0\,, \qquad \lambda_{ZT} = \lambda_{HT} = Y_* \cos\varphi_L \sin\varphi_{tR} \tag{3.27}$$

$$\lambda_{W\tilde{T}} = \lambda_{Z\tilde{T}} = \lambda_{H\tilde{T}} = Y_* \sin\varphi_L \cos\varphi_{tR}\,. \tag{3.28}$$

Because of the large mass of the VLQ top compared to the SM top quark mass or W boson mass, the branching ratios above channels can be written as follows:

$$\begin{gathered} BR\left(T \to Z_L t_R\right) \simeq BR\left(T \to H t_R\right) \simeq 50\%\,, \\ BR(\tilde{T} \to W_L b_L) \simeq 50\%\,, \quad BR(\tilde{T} \to Z_L t_L) \simeq BR(\tilde{T} \to h t_L) \simeq 25\%\,, \end{gathered} \tag{3.29}$$

Considering the small chance of the heavy gluon decaying to $b\bar{b}$, we will exclude this channel during this analysis. Three final channels are thus identified, listed below and nicely shown in figure 3.5 as a

[9] The couplings $\lambda_{W\chi}$, $\lambda_{Z\chi}$, $\lambda_{H\chi}$ are extracted from the coefficients of the Yukawa terms in the diagonalized Lagrangian defined in appendix A of [9].

function of heavy gluon mass [9] for the same reference values of parameters chosen for figures 3.3:

$$\tilde{T}t \to Wbt\,, \qquad Tt, \tilde{T}t \to Zt\bar{t}\,, \qquad Tt, \tilde{T}t \to Ht\bar{t}\,. \tag{3.30}$$

Therefore, the final decay chain of heavy gluons through four generations is shown in figure 3.4 (the heavy gluon is then considered as the Mother).

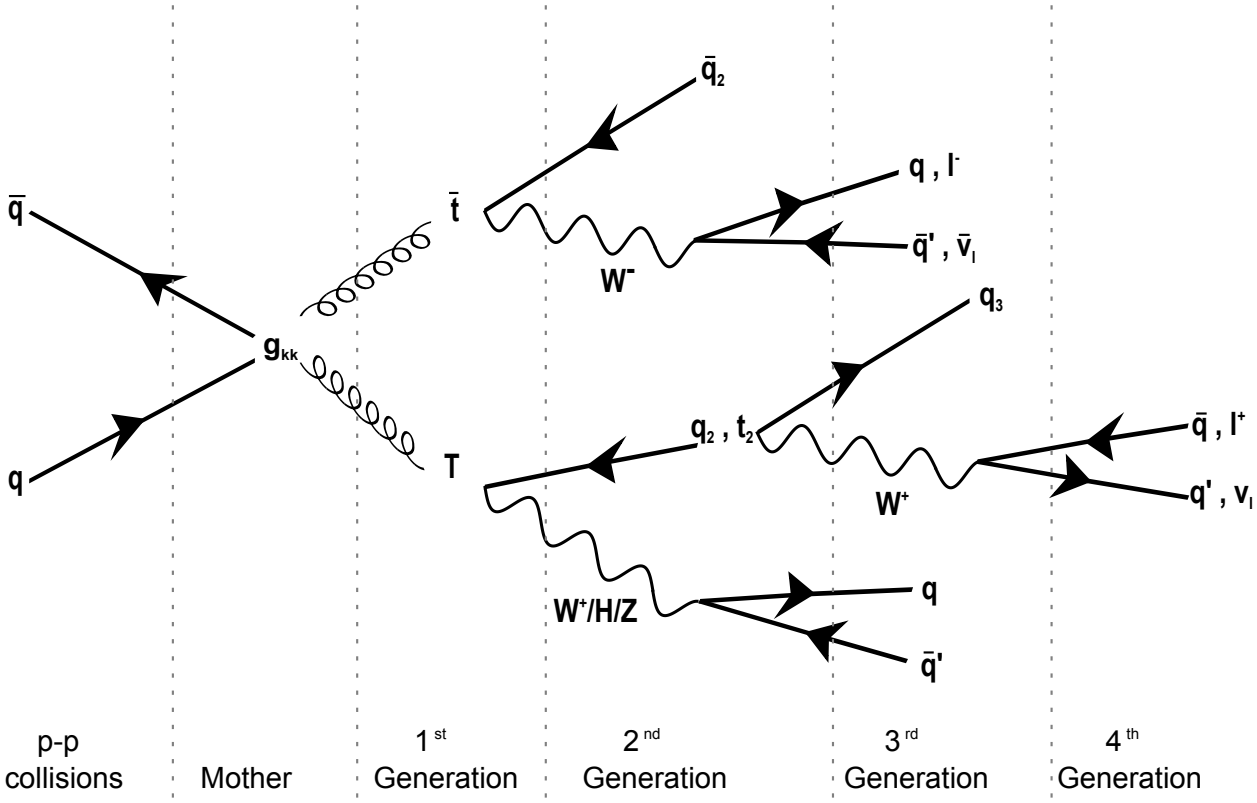

Figure 3.4: A possible decay chain of heavy gluons (g_{KK}) through four generations in the decay chain. The abbreviations used are: t and T for SM and vector-like top quarks, respectively, q_2 for bottom quarks, q for any quark, l and ν_l for lepton (μ or e) and its neutrino. Note that the Higgs boson (H) is a composite Higgs (see section 3).

Figure 3.5, shows once again that each of the heavy-light topologies has a sizeable branching ratio in a large range of heavy gluon masses above $m_{\tilde{T}}$ and below 2 $m_{\tilde{T}}$ where the discovery of the heavy gluon seems promising. On the one hand, we will reconstruct the VLQ top mass via the invariant mass of a subsystem in each heavy-light decays topology. The QCD background is thus heavily reduced. On the other hand, the light-light decay topology has a very small branching ratio in the limits of $m_{\tilde{T}} \lesssim m_{g_{KK}} < 2\ m_{\tilde{T}}$ and thus a very low efficiency for a discovery channel. Hence, the $t\bar{t}$ signal is considered as a background during the heavy-light topologies analysis. This kind of analysis could lead

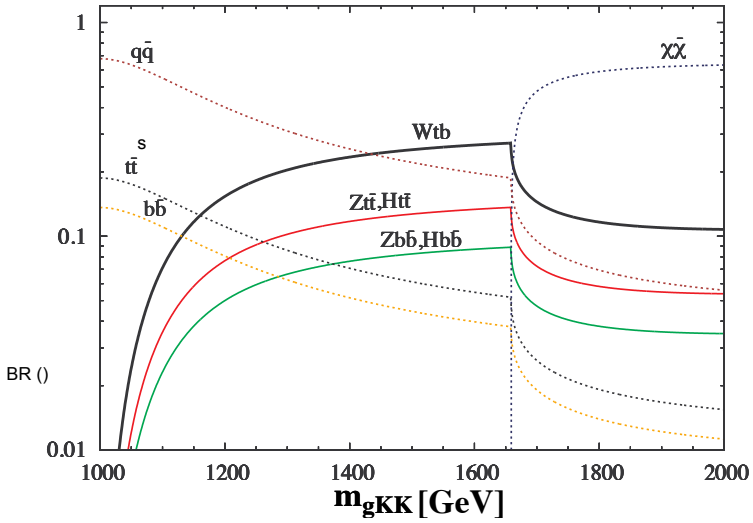

Figure 3.5: Branching ratio of the various final states that follow from the decay of g_{KK}, as functions of $m_{g_{KK}}$ [9]. The other parameters are set to the same reference values used for Fig. 3.3: $m_{\tilde{T}} = 1$ TeV and $\tan\theta_3 = 0.44$, $\sin\varphi_{tR} = 0.6$, $Y_* = 3$. The decay channel $Ht\bar{t}$ ($Hb\bar{b}$) has the same branching ratio of $Zt\bar{t}$ ($Zb\bar{b}$).

to the measurement of some important features of the fermionic sector such as the VLQ top couplings to the SM vector bosons, and thus determine its origin.

Finally, the considerations on the size of the SM backgrounds, made by previous studies [9, 21, 52, 53], suggest that the most promising final states could be Wt_b, $Zt\bar{t}$ and $Ht\bar{t}$ (Eq. 3.30). If we assume that the Higgs boson mostly decays to two SM bottom quarks, a VLQ top with charge $+2/3$ will then appear as a $(b\bar{b}t)$ resonance in $b\bar{b}t\bar{t}$ events or as a (Wb) resonance in Wtb events if it is a singlet of $SU(2)_L$ $(\tilde{T})$. The non-observation of this latter signal will be a motivation to consider the VLQ top as part of a doublet of $SU(2)_L$ (T).

4 Experimental setup

In this chapter, we will present the experimental procedures used to collect the data from hadron collisions in the ATLAS experiment, and to construct physics objects. ATLAS is located in the Large Hadron Collider (LHC) tunnel, which is part of the European Organization for Nuclear Research, commonly called CERN. The LHC tunnel has a circumference of 27 km, and is based in France and Switzerland. Besides ATLAS (A Toroidal LHC ApparatuS), the tunnel has six experiments which are ALICE (A Large Ion Collider Experiment), LHCb (Large Hadron Collider beauty), MoEDAL (Monopole and Exotics Detector at the LHC), TOTEM (ToTal Elastic and diffractive cross section Measurement), LHCf (Large Hadron Collider forward) and CMS (Compact Muon Solenoid).

4.1 Higher energies and larger luminosities

In colliders, what is called collider energy is in fact the energy of the center-of-mass system $\sqrt{s}$ which is a function of the energy of a beam of protons (E) as follows[1]:

$$\sqrt{s} = 2 \times E. \tag{4.1}$$

At LHC, during 2012 with the collisions at $\sqrt{s} = 8$ TeV (from proton beams of E =4 TeV), maximum of energies achieved in the center of mass was 8 times greater than the one produced at the TeVatron [2]. Last year, collisions of 13 TeV have been produced. These conditions help us to obtain energies at which the cross sections to produce heavy resonances of few TeV are large enough that we could have a chance to produce and observe them.
The analyses of the lightest heavy gluon and the lightest vector-like top quark were performed using data taken from the ATLAS experiment during the collisions at 8 TeV.

A collider is also characterized by its dimensions (the circumference size), its luminosity (L) and the type of the accelerated particles that are collided (frontal collisions or head-on collisions). To achieve energies of collision of up to 14 TeV, at LHC, one needs to go through the following steps:

- Protons are accelerated, via the ionization of hydrogen, until each proton reaches 23 GeV while running in the Proton Synchrotron (PS), and 450 GeV in the Super Proton Synchrotron (SPS);

[1] The result of the equation 4.1 is to be compared with the energy of the center of mass between a beam with energy E and a stationary target with a mass of m: $\sqrt{s} = \sqrt{2mE}$.
[2] TeVatron was the most powerful collider until year 2009 just before the LHC first run.

- 2808 bunches (7.4 m apart) of 1.15$\times$ 10^{11} protons are injected from the SPS into each of the two synchroton rings of the LHC. Then, the bunches of protons are accelerated at around the light speed until the protons achieve an energy of 7 TeV (for 14 TeV collisions);
- finally the proton beams are focused and collided at four intersections each of which corresponding to CMS, LHCb, ALICE and ATLAS experiments.

In physics, we are interested in the estimation of the probability of interactions from head-on collisions. The parameter used to define this probability is the luminosity (L). The event rate R in a collider is proportional to the interaction cross section σ_{int} and the luminosity:

$$R = L \times \sigma_{int}. \tag{4.2}$$

The luminosity depends only on the synchrotron properties. Therefore, in a synchrotron, the luminosity is a function of the number of bunches N_1 (and N_2) in the first (and in the second) ring, the transverse beam area A_{Teff} in the horizontal direction and the revolution frequency f_{rev}:

$$L = \frac{n_b \times f_{rev} \times N_1 \times N_2 \times F}{A_{Teff}}. \tag{4.3}$$

At LHC, the number of bunches is n_b=2808, $F \sim 0.8$ is a constant related proton proton collision geometry [3], the transverse area and the revolution frequency of the beams are:

$$A_{Teff} = 4\pi \times (\sigma_x\ \sigma_y) = 4\pi \times (17\ \mu\text{m})^2, \tag{4.4a}$$

$$\tag{4.4b}$$

$$f_{rev} = \frac{\text{proton speed}(\text{km s}^{-1})}{\text{LHC circumference length}(\text{km})} = \frac{3 \times 10^5}{26.7} \approx 11\ \text{kHz}. \tag{4.4c}$$

where σ_x and σ_y are the effective width of the horizontal and vertical profiles of the colliding beams, respectively.

[3] $F = F(\theta_C) = [\sqrt{1 + \frac{\theta_c \sigma_z}{2\sigma^*}}]^{-1}$ with $\sigma^* \sim \frac{\sigma_x + \sigma_y}{2} \sim 17$ µm (where σ_x and σ_y are the effective width of the horizontal and vertical profiles of p-p beams, respectively.), $\theta_C \sim 285$ µrad for crossing angle and $\sigma_z = 7.55$ cm for p-p collisions.

The maximum of the luminosity achieved at LHC is, then, up to $L \approx 10^{34}\ cm^{-2}s^{-1}$ (design luminosity), leading to an integrated luminosity during an effective year (=10^7 seconds):

$$L_{int} = \int_{t=0}^{10^7} L\,dt = 10^{34} \times 10^7 = 10^{41}\,cm^{-2} \approx 100\,\text{fb}^{-1}. \tag{4.5}$$

However, during 2012 collisions at 8 TeV, the LHC delivered an integrated luminosity of 23.30 fb^{-1}, and the ATLAS experiment recorded 20.3 fb^{-1}. The latter integrated luminosity recorded by ATLAS, during year 2012, is to be compared with the luminosity of 10 fb^{-1} achieved at the TeVatron during $8-9$ years. The cross sections are then much larger at LHC, so when it comes to the number of particles produced (such as the Higgs boson, top-anti top pairs, new heavy particles), LHC is by far much more powerful than TeVatron. Figure 4.1 shows the cross sections of the SM particles as a function of collider energy [10], LHC and TeVatron energies are highlighted by vertical dotted green line.

4.2 The ATLAS detector

LHCb is used for Flavour physics and measurements of the constants in the CKM matrice, ALICE is used to study the quark gluon plasma (QCD sector) and MoEDAL is designed to search for highly ionizing manifestations of new physics, such as magnetic monopoles or massive (pseudo-)stable charged particles. CMS and ATLAS are two detectors for the study of general physics. Data collected by the two latter detectors are used to track new physics but also to check the SM parameters with higher accuracy.

The ATLAS detector is the biggest detector thanks its dimensions of $44\,m \times 4\,m \times 25\,m$. Its toroidal shape as shown by figure 4.2, allows a forward-backward symmetry regarding the collision center (in the vacuum chamber) where the coordinate system used in ATLAS is centered.

As shown in figure 4.3, the x-axis of the coordinate points to the center of the LHC ring, the y-axis points upwards and the z-axis, along beam direction, is the right-handed coordinate system direction. The azimuthal angle (ϕ), is measured in the $(x-y)$ plane, and, the polar angle (θ) is measured in the $(z-y)$ plane (with $z > 0$). However, a useful coordinate is the pseudo-rapidity shown on the right hand side of figure 4.3 and defined as: $\eta = -\ln(\tan\frac{\theta}{2})$.

Let us imagine two physical objects J_1 and J_2 corresponding to two detected particles in the detectors. To reconstruct these objects we need to determine three parameters, which are $\Delta R(J_1, J_2)$ for the direction of their momenta, the transverse momentum p_T and the transverse energy, E_T, of each particle. The transverse momentum (energy) is simply the projection of the momentum (energy) in the

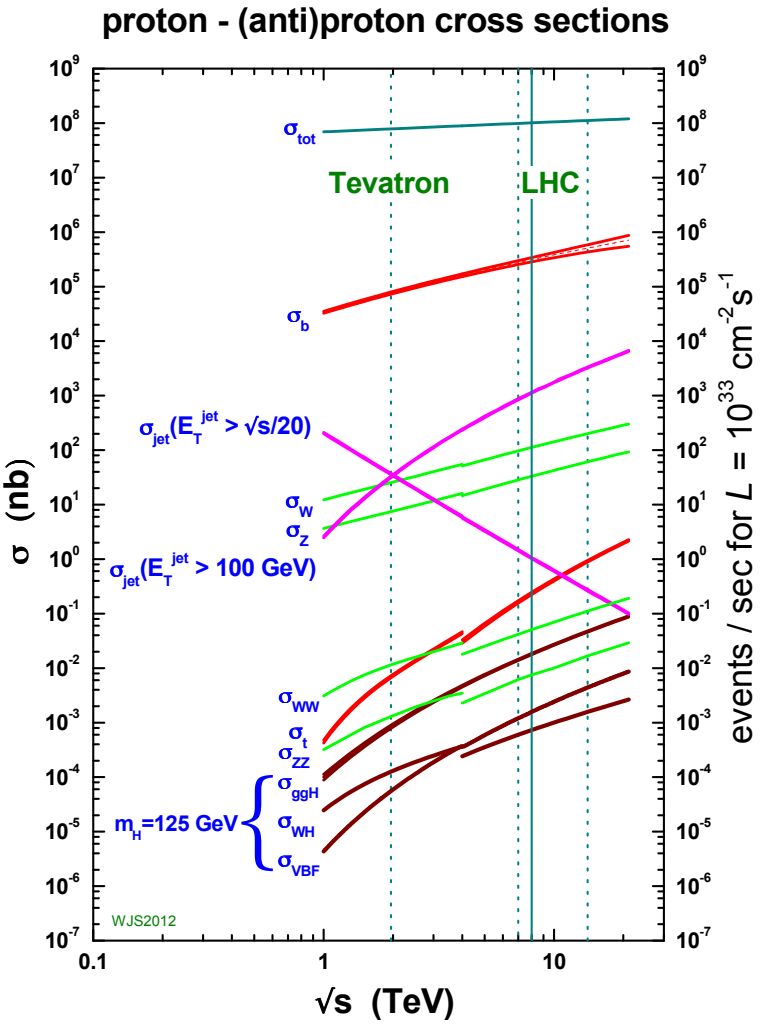

Figure 4.1: Standard Model cross sections as a function of collider energy [10]. These cross sections are calculated either at NLO or NNLO pQCD, using MSTW2008 (NLO or NNLO) parton distributions, with the exception of the total hadronic cross section which is based on a parameterization of the Particle Data Group. The discontinuity in some of the cross sections at 4 TeV is due to the switch from proton-antiproton to proton-proton collisions at that energy.

$(x - y)$ plan. These parameters are calculated as follows:

$$\Delta R(J_1, J_2) = \sqrt{[\Delta\eta(J_1, J_2)]^2 + \Delta\phi(J_1, J_2)]^2}\,, \quad \text{with} \tag{4.6a}$$

$$\Delta\eta(J_1, J_2) = \eta(J_2) - \eta(J_1), \quad \text{and} \tag{4.6b}$$

$$\Delta\phi(J_1, J_2) = min\,[\,|\phi(J_2) - \eta(J_1)|\,, 2\pi - |\phi(J_2) - \eta(J_1)|\,]\,, \tag{4.6c}$$

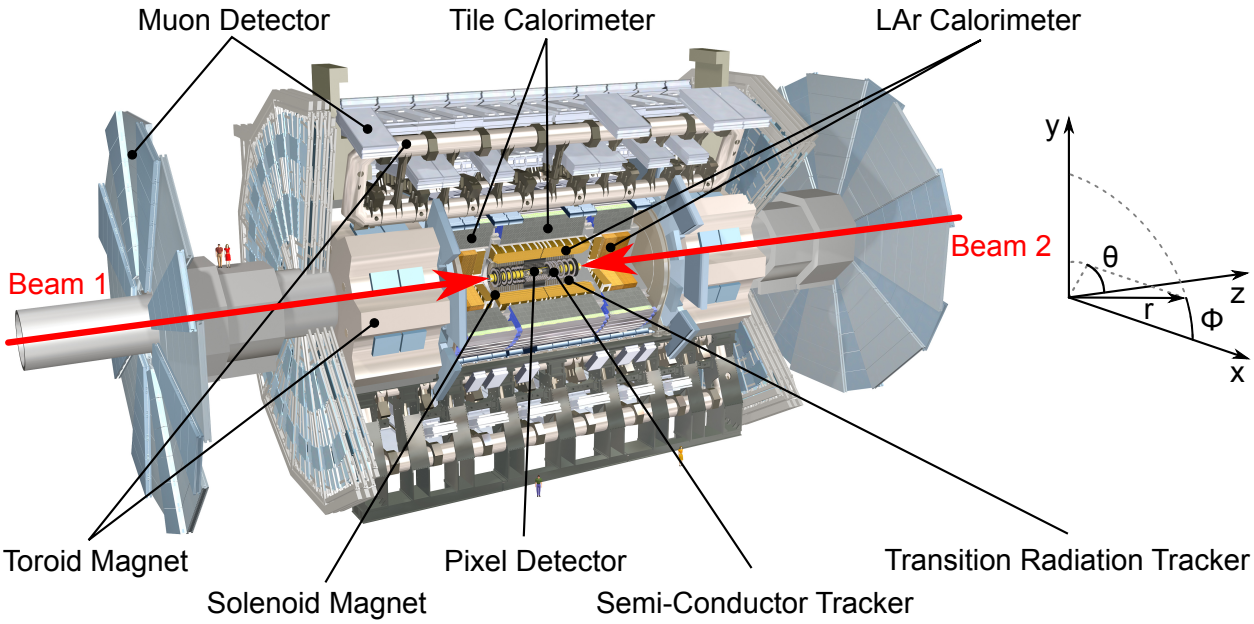

Figure 4.2: The general view of ATLAS. The detector is composed of three main sub-detectors from inside to outside: the Inner Detector immersed in a 2 T magnetic field (Solenoid Magnet), the calorimeters (LAr and Tile) and the Muon Spectrometer. The Inner Detector groups the innermost detector called pixel, the SCT and the Transition Radiation Tracker. Finally, the calorimeters are divided into LAr Calorimeter and Tile Calorimeter. Two sets of magnets are used in ATLAS: the Solenoid Magnet around the Inner Detector to bend charged particles trajectory, and the Toroid Magnet covering the Tile Calorimeter for muon trajectory bending. Note that the colliding beams are in red and the ATLAS coordinate system drawn in the right hand side is centered on the collision point (e.g., center of ATLAS). All credits to © CERN.

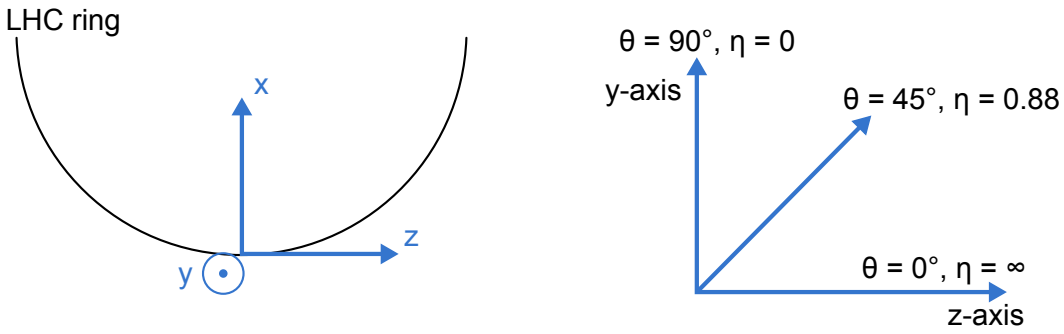

Figure 4.3: ATLAS coordinate systems: on the left-hand side, the x-axis points to the center of the LHC ring, the y-axis points upwards, and the z-axis is the right-handed coordinate system direction. On the right hand side, the pseudo-rapidity η in the $(z\,, y)$ plan is given for different values of the polar angle θ when $z > 0$.

$$p_T = p/\cosh(\eta)\,, \tag{4.7}$$

$$E_T = E/\cosh(\eta)\,, \tag{4.8}$$

where p is the magnitude of the particle three-momentum and E is the particle energy.

Finally, the cylindrical shape of the ATLAS ensures the coverage of the solid angle $\Omega = 4\pi$ by each of its main sub-detectors (see figure 4.2). The sub-detectors, shown in figures 4.2 and 4.4, are from inside to outside: the Inner Detector, the Calorimeters (LAr and Tile) and the Muon Spectrometer.

4.2.1 The Inner Detector

The Inner Detector [63, 64], is composed of three sub-detectors drawn in figure 4.5: the Pixel Detector, in green, facing the collision point at $R = 0$, the Semi-Conductor Tracker (SCT), in blue purple, as the middle detector, and the outer sub-detector, called the Transition Radiation Tracker (TRT), in yellow. As seen in schema 4.4, a charged particle leaves tracks while crossing each detector: the reconstruction of these tracks is the aim of the Inner Detector.

The Pixel Detector and the SCT are the innermost detectors, and cover a pseudo-rapidity region of $|\eta| < 2.5$. As seen in figure 4.6, in the barrel region, they are arranged as cylinders around the beam axis, but in the end-cap regions they are organized as disks perpendicular to the z-axis. Their extreme proximity to the collision point, requires tracking with sufficient precision such that the particles could be distinguished from the high-rate background in that area. An axial magnetic field of 2 T is created by the thin superconducting solenoid around the Inner Detector, with the aim of bending the charged particles trajectory. A particle trajectory is estimated from a fit to the hits [4] in the sub-detectors. In the magnetic field, the charge of the particle is determined by the bending direction and the Lorentz force law:

$$\mathbf{F} = q\,\mathbf{v} \times \mathbf{B}\,. \tag{4.9}$$

where q is the charge of the particle ($q = \pm e$), $\mathbf{F}$ the Lorentz force, $\mathbf{B}$ the magnetic field and $\mathbf{v}$ is the particle velocity vector. Finally, the charge to the momentum ratio, e/p, is estimated from the curvature of the track.

[4] Each point of the charged particle-detector interaction is called a hit. A track is made from the particle hits along its trajectory in the Inner Detector.

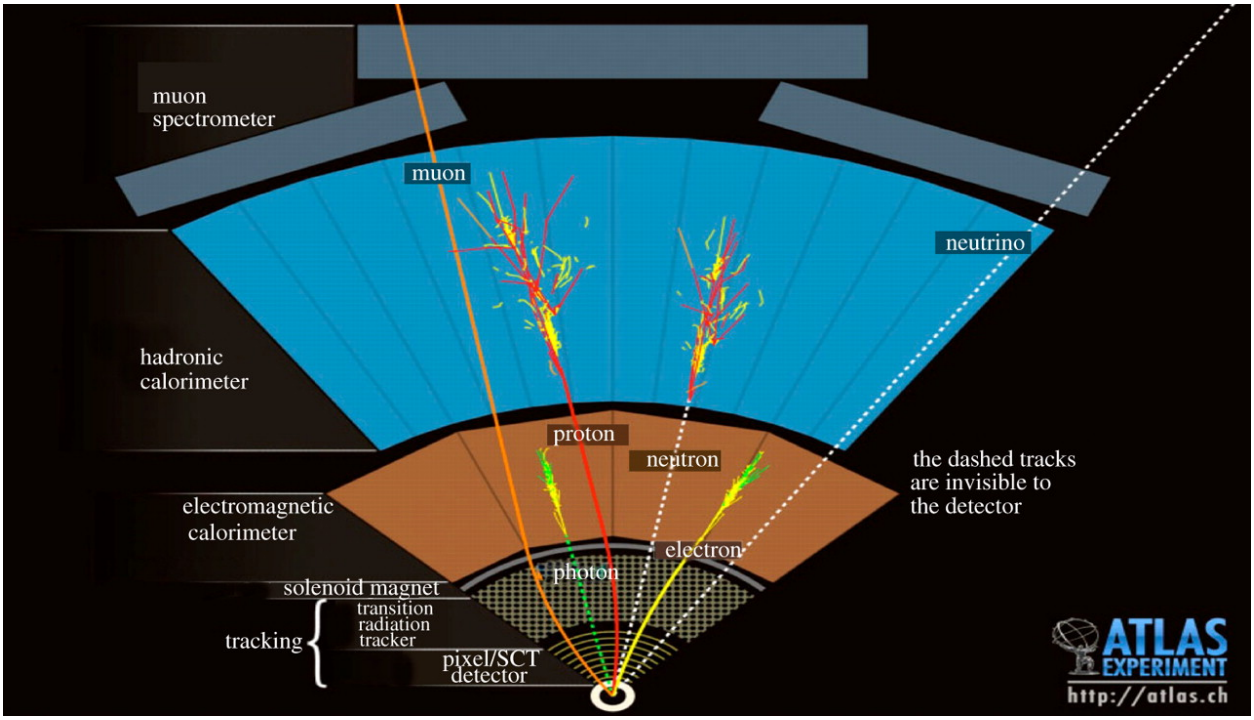

Figure 4.4: Particles interactions in different sub-detectors of ATLAS. Charged particles leave a track in the Inner Detector, photons and electrons lose their energy in the LAr Calorimeter, hadrons finish their journey in the Tile Calorimeter but the muons will fly the entire ATLAS Detector which magnetic fields can only slow them down by bending their trajectory. All credits to © CERN.

Notice that, in a magnetic field of B (in T), the transverse momentum from equation 4.7 is a function of the radius of the curve r (in m) as [5]:

$$p_T = 0.3\, B\, .\, r\ = p/\cosh(\eta). \tag{4.10}$$

The Pixel is a three-layer detector, the innermost layer of which is called the B-layer. With a 4 cm radius, B-layer is used for vertexing with an incredibly high performance. Moreover, each layer is an assembly of identical silicon pixel sensors of the size of (50×400) μm^2 in $(R-\phi\times z)$ plans. Finally, the number of the Pixel readout channels is approximately 80.4 million.

In the barrel region, the SCT is made of four cylindrical silicon strips layers, and eight layers of small-angle strips used for the coordinates measurement: one set of strips parallel to the z-axis measures the direction in the $(R-\phi)$ plan. Each layer is 6.4 cm long and contains 768 sensors of 80 μm strip pitches.

[5] As order of magnitude, a particle with a transverse momentum of $p_T = 1$ GeV deviated by the ATLAS axial magnetic field ($B = 2$ T) will leave a track of 1.67 m.

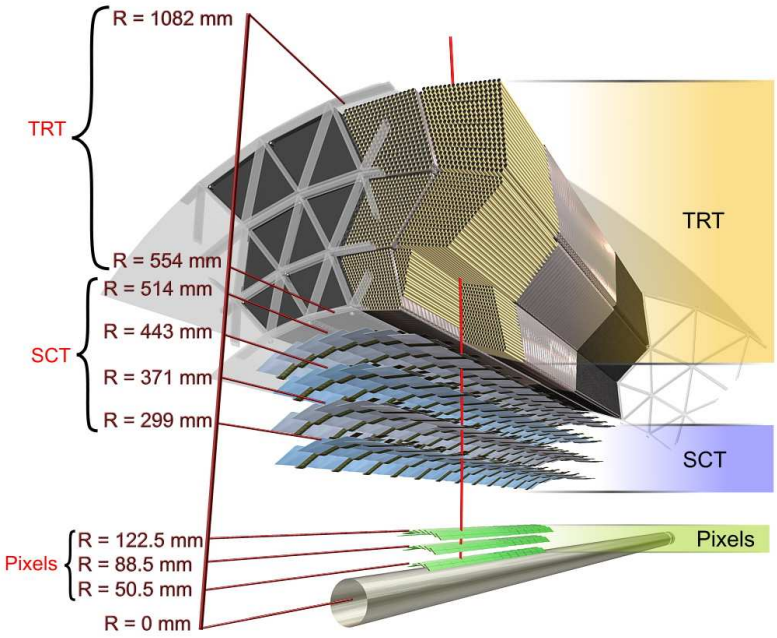

Figure 4.5: A view of the ATLAS Inner Detector, in the barrel region, composed of Pixels disposed around the collision region at $R = 0$, the Semi-Conductor Tracker (SCT) in blue purple and the Transition Radiation Tracker (TRT) in yellow. All credits to © CERN.

However, in each end-cap region, the SCT is made of nine disks, and the strips are radial. The SCT intrinsic granularity per module is (17$\times$ 580) µm for ($R - \phi \times z$), and, the total number of readout channels is around 6.3 million. The SCT is used to measure the impact parameter, and vertexing for heavy-flavors and τ-lepton tagging.

On the SCT detector, the Transition Radiation Tracker (TRT) is characterized by its pseudo-rapidity coverage of $|\eta| < 2.0$, its straw tubes of 4 mm diameter. In the barrel region, the straws are 144 cm long and parallel to the beam axis. While in the end-cap regions, the straws are 37 cm long and form radial wheels. The TRT provides $R - \phi$ coordinates information with an intrinsic accuracy of 130 µm per straw and the total readout channels is around 351×10^3.

The combination of precision trackers at small radii (Pixel and SCT), with the TRT at a large radius, leads to a robust pattern recognition and high precision in both coordinates. The low precision per point, in the TRT straws, is thus compensated by the large number of measurements and longer measured track length.

Once the tracking is provided by the Inner Detecter, different algorithms are used to fit the tracks. This leads to the best possible estimations of the charge to the momentum ratio, the particle transverse momentum, the trajectory, and, the closest point of the primary vertex in the ($x - y$, z) plan. By

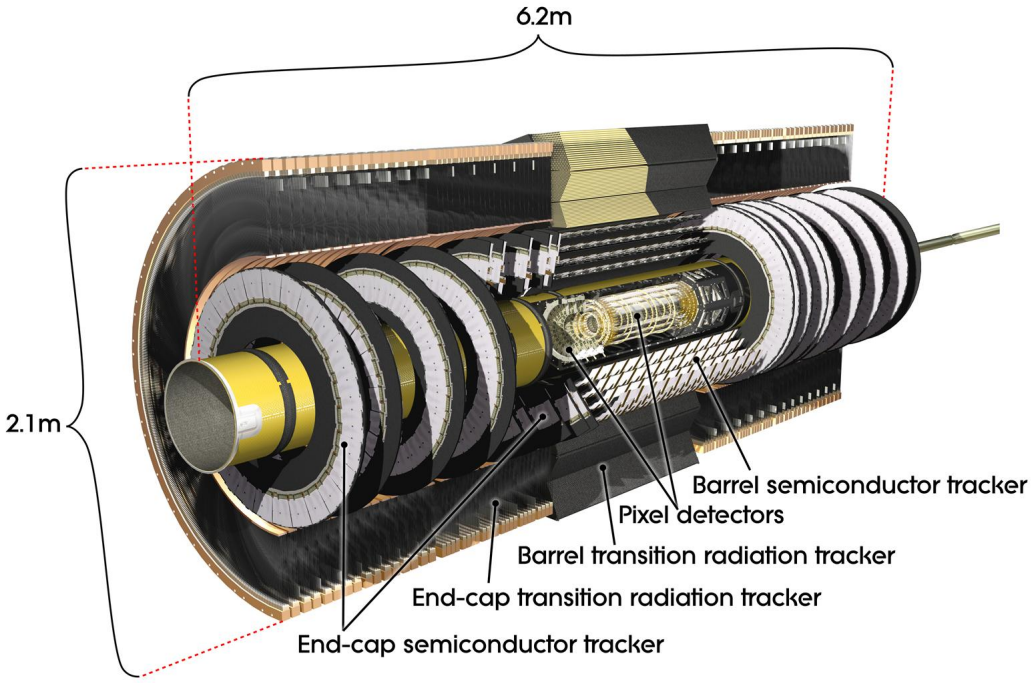

Figure 4.6: A general view of the ATLAS Inner Detector. Its sub-detectors are parallel (perpendicular) to the beam axis in the barrel region (end-cap regions). All credits to © CERN.

convention, the distance of the track to the primary vertex, in $z-$axis, is called the longitudinal transverse parameter (denoted as z_0), and in the $(x-y)$ plan, the transverse impact parameter (denoted as d_0). These parameters are drawn in figure 4.7. Then, only the good reconstructed tracks are selected. These good tracks are the ones with demands in the number of hits per track, and which match the hits in the electromagnetic Calorimeter. Notably, the electron identification starts with the selection of transition-radiation photons in the xenon-based gas mixture of the TRT straw tubes.

4.2.2 The Liquid Argon and Tile Calorimeters

Covering the Inner Detector, are the Calorimeters, in both barrel and end-cap regions. The Calorimeters are divided into Liquid Argon (LAr) Calorimeter and Tile Calorimeter, usually called electromagnetic and hadronic Calorimeter(figure 4.8), respectively, each of which is made of alternative layers of absorbers and samplers.

The LAr Calorimeter structure is ideally suited to absorb and measure the energy of the electrons and photons (and also the energy of the hadrons in the end-cap regions), as seen in figure 4.4. It is divided

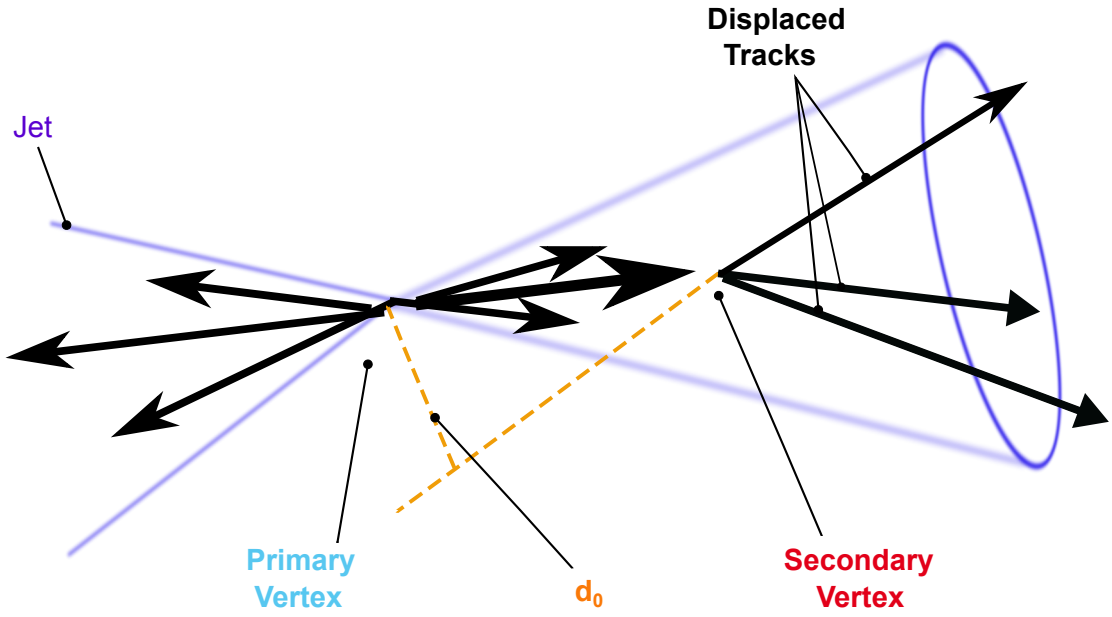

Figure 4.7: Schematic view of a hadron decay in two jets at the primary vertex. Inside of one the jets, an unstable hadron will decay resulting in a secondary vertex with three charged particle tracks. The tracks are significantly displaced with respect to the secondary and primary vertices. The track transverse (longitudinal) impact parameter d_0 (z_0) is the distance of the closest approach between the extrapolation of the track and the primary vertex.

into a barrel region to cover $|\eta| < 1.475$, and two end-cap regions in $1.375 < |\eta| < 3.2$ (figure 4.8). In the barrel region at $z = 0$, the calorimeter is divided into two identical half-barrels separated by a gap of 4 mm. Each end-cap calorimeter is organized as two coaxial wheels.

The electromagnetic interactions are measured, as a function of the ϕ coordinates (without any azimuthal cracks), with the help of the accordion geometry in the barrel region. The liquid argon fills the interspaces between the layers of lead and stainless steel absorbers. The lead gives the cascade development with its short radiation length ($X_0 = 1.8$ cm), and the secondary electrons create ionisation in the narrow gaps of liquid argon. A signal is, then, induced and collected by the copper electrodes

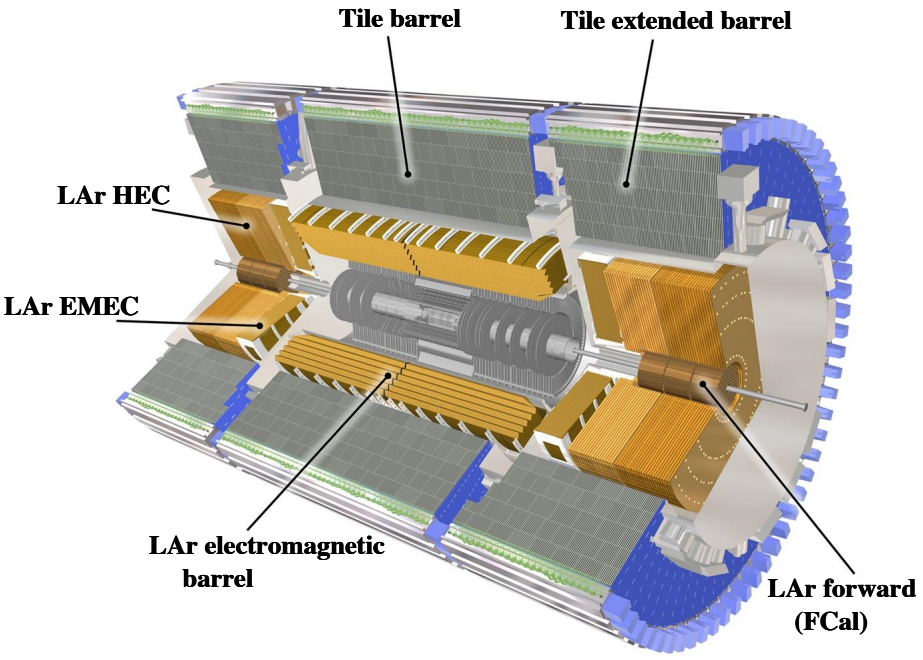

Figure 4.8: A view of the ATLAS Calorimeter. The LAr Calorimeter, in yellow, is divided into two identical half-barrels separated by a thin gap. Each end-cap calorimeter (HEC and EMEC stand for hadronic end-cap and electromagnetic end-cap, respectively) is organized as two coaxial wheels. Around the LAr Calorimeter is presented the Tile Calorimeter, in grey. In the barrel and the end-cap regions, the Calorimeter is segmented in layers and organized as wheels, respectively. All credits to © CERN.

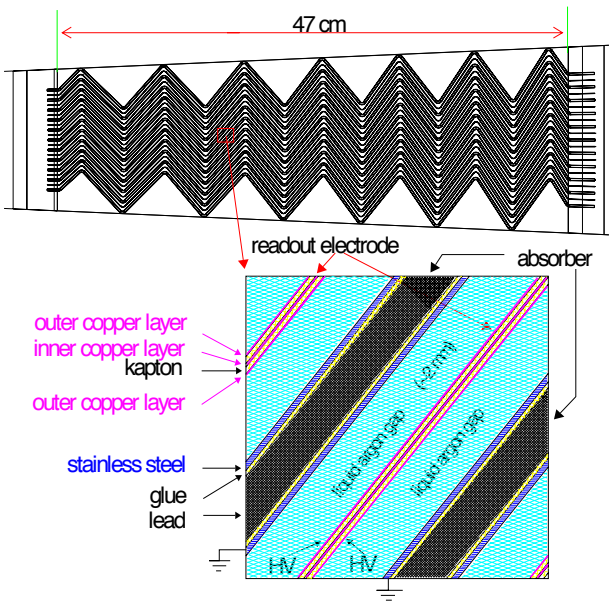

Figure 4.9: The accordion geometry of the calorimeter, in the barrel region, made of alternative layers of liquid argon absorbers (in azure) and lead (in grey) and stainless steel (in blue) samplers. The short radiation length of the lead helps with the start of an electromagnetic cascade which secondary electrons are ionized while hitting then drifting in the liquid argon. A signal is then induced and collected by the copper electrodes (in pink). All credits to © CERN.

(figure 4.9). Finally, the measured energy is corrected via electromagnetic measurements from a pre-sampler detector, located in the calorimeter region of $|\eta| < 1.8$. This pre-sampler detector is made of an active liquid argon layer of thickness of 1.1 cm in the barrel (0.5 cm in the end-cap) region.

The Tile Calorimeter, presented in grey in figure 4.8, is a hadronic cascade sampling using steel as absorber material and scintillating tiles as the active material. The collected signals, in the scintillators, are read with wavelength shifting fibers, and converted with photomultipliers (PMTs) into electric signals. This Calorimeter covers the regions $|\eta| < 1.0$ and $0.8 < |\eta| < 1.7$ corresponding to the barrel and extended barrel regions, respectively. The latter regions are divided azimuthally into 64 modules. Radially, the calorimeter has an inner radius of 2.28 m, and a outer radius of 4.25 m. In the barrel region, it is segmented in three layers, corresponding to 1.5 λ, 4.1 λ and 1.8 λ interaction length. In the extended barrel region, there is also a three-layer organization of the Calorimeter for three different 1.5 λ, 2.6 λ and 3.3 λ interaction length. The active calorimeter in the barrel is about 9.7 λ total interaction length which is deep enough for the calorimeter to contain the entire hadronic cascades.
In each end-cap region, the Tile Calorimeter consists of two independent wheels and cover the region of $1.5 < |\eta| < 3.2$. The end-cap regions have approximative 10 λ interaction length which is large enough to contain the hadronic cascades as shown in figure 4.4.

Therefore, the fine granularity of the LAr Calorimeter is ideally suited for precision measurements of electrons and photons while the coarser granularity of the Tile Calorimeter is sufficient to satisfy the physics requirement for jet reconstruction but also for the missing transverse energy E_T^{miss} measurements corresponding to the energy of the neutrinos represented by a dotted white line in figure 4.4.

Finally, the Liquid Argon Forward Calorimeter (FCal) (denoted as LAr forward in figure 4.8) is integrated into the end-cap regions. It was designed to detect hadron jets at angles from 1 to 5 degrees relative to the proton beams, but, also for the uniformity of the calorimetric coverage, and radiation background reduction in the Muons Spectrometer. More detail can be found in [63].

4.2.3 The Muon Spectrometer

The outermost part of the ATLAS detector is called the Muon Spectrometer. It surrounds the calorimeters, and measures the trajectories of muons to determine their direction, their electric charge and their momentum. Unlike electrons, photons and hadrons which are absorbed during their journey, muons can penetrate through the calorimeters and reach the outermost part of ATLAS and leave tracks behind (orange line in figure 4.4).

The Muon Spectrometer is made of a set of three large superconducting air-core toroid magnets, a trigger and high precision tracking chambers. In the barrel region of $|\eta| < 1.4$, the toroid magnets are disposed as eight coils used to deviate the muon tracks coming from the hadronic calorimeter. In each of the end-cap regions (corresponding to $1.6 < |\eta| < 2.7$), two small magnets bend the muon tracks. Over the transition region of $1.4 < |\eta| < 1.6$, the magnetic deflection of the muon tracks is provided by both barrel and end-cap regions' magnets.

The detection elements in the chambers, are made of thousands of metal tubes equipped with a central wire and filled with gas. As a muon passes through these tubes, it leaves a trail of electrically charged ions and electrons which drift to the sides and center of the tube. By measuring the time it takes for these charges to drift from the starting point, it is possible to determine the position of the muon as it passes through. The chambers form three cylindrical layers around the beam axis in the barrel region. In the transition and end-cap regions, chambers are arranged in three layers of planes perpendicular to the beam axis. As shown in figure 4.10, over most of the pseudo-rapidity range, the layers are a type of Monitored Drift Tube (MDT). However, for large pseudo-rapidities ($2 < |\eta| < 2.7$), the layers are multi-wire proportional chambers with strips segmented cathodes. The latter layers are commonly named as Cathode Strip Chambers (CSC). The two latter types of chambers provide precision tracking. Furthermore, the regions of $|\eta| < 2.4$ are covered by the trigger chambers. Layers of Resistive Plate Chambers (RPC's) and Thin Gap Chambers (TGC's) are used in the barrel and end-cap regions, respectively. Finally, the trigger system provides bunch-crossing identification, p_T thresholds and muon coordinate in the direction orthogonal to the coordinates provided by the precision-tracking chambers.

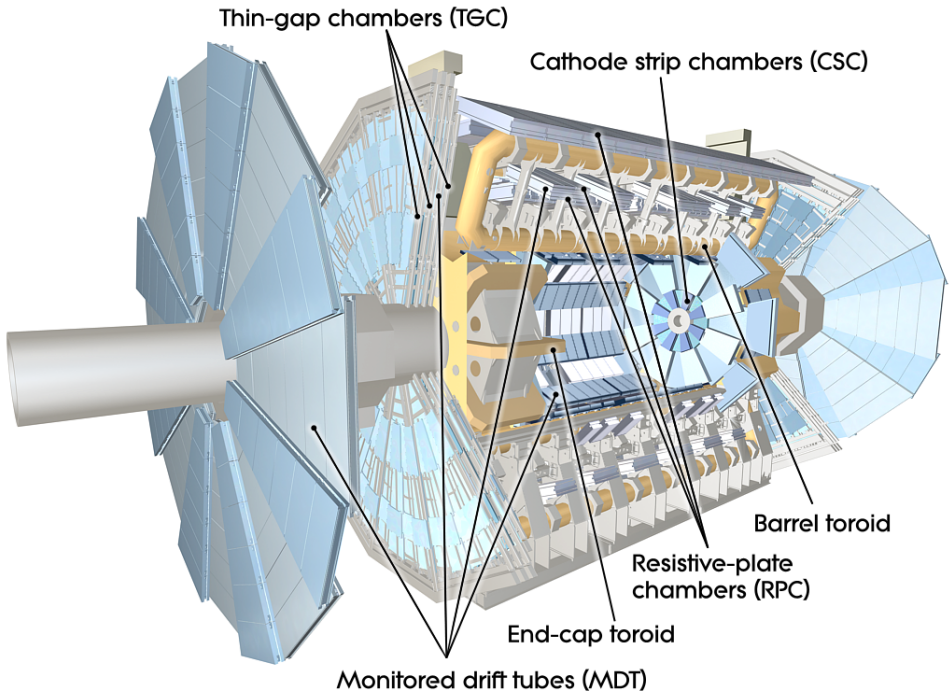

Figure 4.10: General view of the ATLAS Muon Spectrometer. It is made of Monitored Drift Tube (MDT), Cathode Strip Chambers (CSC), Resistive Plate Chambers (RPC's) and Thin Gap Chambers (TGC's) in the barrel and end-cap regions, respectively. The first two components provide precision tracking while the others are used to trigger fast response to select events which contain muons. All credits to © CERN.

4.3 Physics object reconstruction

In chapter 3, the prime importance of searches for particles introduced by models beyond the SM has been developed. For the collision energies achieved at LHC, searches for direct heavy gluon production (from hadron collisions) are possible. An analysis based on a top quark pair production study [65] is presented in this thesis (as a reminder please see the left plot of figure 3.3) Once produced, the heavy gluon decays, through a new QCD-like force, into a vector-like top quark in association with a SM top quark ($T\,\bar{t}$) which form the first generation in the decay chain in figure 3.4. Then, considering the results listed in equations 3.30, the latter vector-like top quarks decays into one of three main final states in which there will be a boson (W, Z or H) and a SM top quark as the second generation of particles in the decay chain. The SM top quark, W, Z bosons and Higgs boson (H) will then decay into final SM particles which are light, stable and form the third and fourth generations in the decay chain. These decays, as well as their corresponding rates, are listed in Table 4.1. However, in this thesis, only events which contain exactly one lepton (one muon or one electron), its associated neutrino and

Particle	Decay channel	Rate
t	Wb	$\sim$100%
W	$l\nu$	10%
	qq'	68%
Z	l^+l^-	3.4%
	hadrons	67%
	$b\bar{b}$	15%
	$\nu\bar{\nu}$	20%
H	$\gamma\gamma$	5.0%
	ZZ	4.0%
	W^-W^+	4.3%
	$\tau^+\tau^-$	5.7%
	$b\bar{b}$	3.2%
	$Z\gamma$	9.0%
	$\mu^+\mu^-$	6.0%

Table 4.1: The list of the most important decay modes with the corresponding rate for the SM top quarks (t), W, Z and Higgs (H) bosons. Index l indicates each type of lepton (e ,μ and τ), ν stands for the neutrino, q and q' for any SM quark. These informations are taken from the Particle Data Group Review.

multiple quarks will be selected. As a consequence, only the following decay channels from Table 4.1 are considered:

- $H \to b\bar{b}$,
- $Z \to b\bar{b}$,
- one single W boson is leptonic ($W \to l\nu$) but the others are hadronic: $W \to qq'$.

Therefore, contributions from background processes must be taken in account because of their high rate of fake production (such as fake leptons and mis-tagged jet). The study of the interactions in ATLAS, in section 4.3.1, will help to find the biggest source of background which will be suppressed mostly by applying the first event selections through ATLAS triggers. In this analysis, specific triggers will be applied for each object reconstruction. A quick presentation of the Trigger System has been made in section 4.3.2. Only then, physics object corresponding to jets, leptons and neutrinos are constructed in the following sections.

4.3.1 Interactions in ATLAS

In the high energy collisions described in section 4.1, we expect to see more than one interaction per collision. Also, the mean number of interactions per proton crossing (denoted as $< \mu >$) is a function

of the luminosity. We can see from figure 4.11 from [66], that $< \mu >$ increased from 9.1 in year 2011 recording a total luminosity of 5.2 fb^{-1} from year 2011 run (azure plot) to 20.7 in year 2012 recording a total luminosity of 21.7 fb^{-1} (green plot). Let us not forget that in each beam collision, two major types

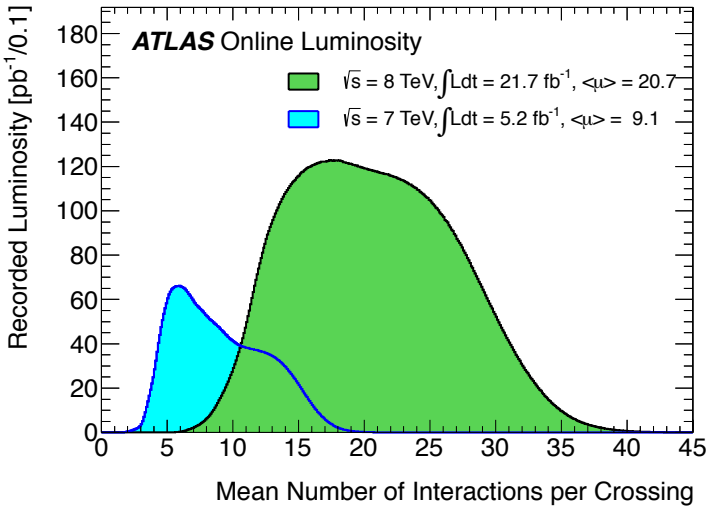

Figure 4.11: The luminosity-weighted distribution of the mean number of interactions per crossing for the 2011 and 2012 data [11, 12]. The mean number of interactions per crossing corresponds to the mean of the Poisson distribution on the number of interactions per crossing ($< \mu >$) calculated for each bunch.

of interactions can happen. The first type is called hard scattering and is a result of the collision between two partons facing each other. The final states of particles produced from these processes are the ones we are looking for. However, beams collisions are dominated by soft-hadronic interactions during which the protons facing each other produce, through inelastic interactions, final state of particles with low transverse momentum. The latter effect is called pile-up to which are associated minimum bias energies referred to as MinBias. Thus, the CERN Data Acquisition System process data with a huge rate of events, most of which are considered as background in the majority of physics analyses: for the design luminosity of 10^{34} cm^{-1} s^{-1}, the LHC will have a 40 MHz bunch crossing rate with an average of 25 interactions per bunch crossing. This is to be compared to 10^{-5} Hz corresponding to the production rate of the final state of particles (such as new particles) from parton collisions. It is technically and financially impossible to store as much data during each run and for each experiment (ATLAS in our case). Consequently, a first data selection is made by the highly selective and efficient Trigger System reducing the data storage rate to 200 Hz [6]. A global description of the ATLAS triggers is made in schema 4.12.

[6] The storage rate of 200 Hz corresponds to an average of data rate of $\sim$ 300 MBs^{-1}.

4.3.2 The ATLAS Trigger System

The ATLAS Trigger System has three distinct levels $L1$ Trigger, $L2$ Trigger and the Event Filter Trigger shown in figure 4.12 from [13]. Each trigger refines the decisions made at the previous level and applies additional selection criteria. The trigger $L1$ is hardware-based and leads to search in each event for [13]:

- high-momentum muons using trigger chambers of the Muon spectrometer,
- electrons, photons, tauons (decaying into hadrons) and jets by using the Calorimeter selections based on coarse granularity information from all the Calorimeters,
- missing transverse momentum.

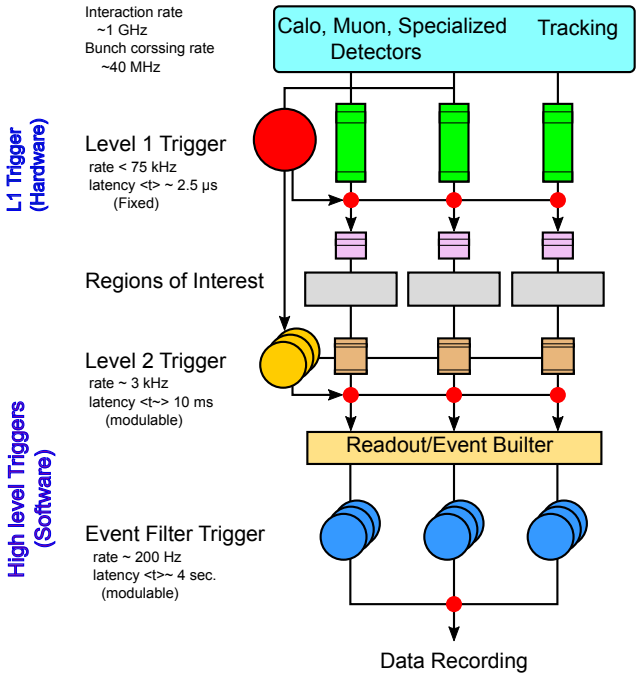

Figure 4.12: A simplified schematic of the ATLAS Trigger System [13]. The Data collected from hadron collisions pass the first trigger $L1$ (in red circles). At this level the Trigger System uses the Calorimeters and the Muon Spectrometer to select, for each event, the good particle. The selected particle position is then saved in a region called Region of Interest (RoI). Are also saved its momentum and energy in the RoI. Then, the selected event passes the two high level Triggers composed of $L2$ (in gold circle) and Event Filter Triggers (in blue circles). The later triggers use the Inner Detector tracking in addition to the Calorimeters and the Muon Detector. For each particle, the RoI is double-checked. If the event passes all the triggers, then it is saved in the Data Recording system. For the Data Acquisition System, the recording rate drops from $\sim$ 40 MHz at the Bunch crossing step to $\sim$ 200 Hz after the Event Filter Trigger ($<$ 75 kHz at $L1$ Trigger and $\sim$ 3 kHz after the $L2$ Trigger.

Using the latter information in each event, the first level trigger is able to select a so-called Regions of Interest, in the coordinates (η, ϕ), where a particle candidate is detected. Also the Region of Interest data contain information about the type of the identified particle and a so-called L_1 threshold at which the event passed. The selected event is then transferred to be checked by two high level triggers, each of which is implemented in software and analysis data with a finer granularity.
The level $L2$ uses the trigger from the Inner Detector tracking system in addition to the Calorimeters and the Muon Spectrometer triggers [13]. It processes only the selected data in the defined Region of Interest and tests the hypothesis that the event contains a relevant signal. The trigger rate is then reduced to $\sim$ 3.4 kHz with an event processing time of $\sim$ 40 ms.
The final stage of the event selection is carried out by the Event Filter trigger (which has the same characteristics as the $L2$ trigger). For each selected event, the trigger will check the decisions made at the previous levels by scanning the entire ATLAS detector with fine granularity. The event rate is, then, reduced to $\sim$ 200 Hz with an event processing time of $\sim$ 4 s [13].

Data for events selected by the Trigger System are written to inclusive data streams based on the trigger type. There are four primary physics streams: Egamma, Muons, JetTauEtmiss and MinBias. Besides of the global ATLAS triggers that have been described above, the triggers are adjusted to each analysis purpose. For the current analyses, appropriate triggers will be used during the reconstruction of each physics object that we need: electrons, muons, jets and missing transverse energye.

4.3.3 Electron objects

The electron triggers, used to identify and reconstruct the electron, is a chain of triggers illustrated in figure 4.13 [13]. The online part of the trigger chain, $L1$-$L2$, is to request that the electron objects match the lowest threshold single electron trigger. The $L1$ trigger used in the present analyses is named EF_E24VHI_MEDIUM1 [7]. It filters electrons with transverse energy (E_T) lower than the threshold value fixed to 24 GeV. Because of the lack of efficiency of this trigger for high energy electron objects (i.e, $E_T >>$ 200 GeV), another trigger called EF_E60_MEDIUM1 is used (in Ored) with a threshold of $E_T >$ 60 GeV. The trigger consists of a loose track isolation $p_T^{0.2}/E_T < 0.1$, so the p_T sum of the tracks in a cone of size $R = 0.2$ around the electron is required to be less than 10% of the electron transverse energy.

Then, comes the offline part of the trigger chain, which is composed of two types of algorithms. The first type, called Feature Extraction (FEX) algorithms, will help to reconstruct the calorimeter clusters where the electron energy is deposited. The created cluster is defined by its pseudo-rapidity η_{cl}, its energy E_{cl} and the direction of its associated track η_{track}. The last two parameters are related to the

[7] EF stands for Event Filter, E for electrons, V and H are used for the calorimeter isolation and stand for varied threshold and the hadronic core isolation, the index I refers to track isolation and medium is for identification.

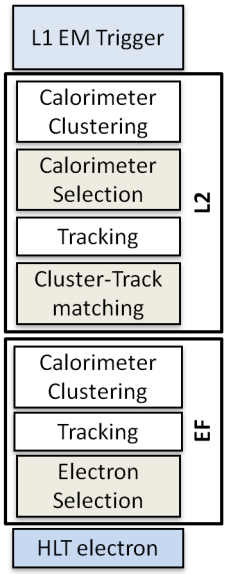

Figure 4.13: The simplified electron trigger chain. Note that HLT stands for High Level Trigger and EF stands for Event Filter [13].

electron transverse energy [8]defined in equation 4.8. Using isolated electromagnetic calorimeter energy deposit matched to an inner detector track [67], we will consider only the cluster with a pseudo-rapidity of $|\eta_{\text{cl}}| < 2.47$ excluding the calorimeter transition region $1.37 < |\eta_{\text{cl}}| < 1.52$.

Next, come the Hypothesis (HYPO) algorithms used to apply selection criteria to the reconstructed clusters. The electron energy transverse should be greater than 25 GeV and satisfy the Tight $++$ criteria. This criteria includes stringent selection cuts on calorimeter, tracking and combined variables that provide good separation between isolated electrons and jets [68].

Then, the track associated with the isolated electron is reconstructed with a longitudinal impact parameter of $z_0 < 2$ mm. To reject fake and the non-prompt electrons, a mini-isolation criteria is applied. Lepton mini-isolation has been defined in [68] and scales as follows [69]:

$$MI_K^l = \sum_{\text{tracks}} p_T^{\text{track}} / p_T^l \,. \tag{4.11}$$

where l is the lepton (electron in this case), and p_T^l is its transverse momentum. The sum runs over all non-lepton, associated tracks with a transverse momentum $p_T^{\text{track}} > 1$ GeV, and passes the following quality cuts:

- transverse impact parameter of $d_0 < 2$ mm,

[8] The cluster parameters are related to the electron transverse energy as $E_T = E_{\text{cl}}/\cosh(\eta_{\text{track}})$.

- $z_0 \sin(\theta_{\text{track}}) < 10$ mm,
- a total of at least 4 hits and dead sensors in the SCT and Pixel Detectors.

Finally, we know that, at these energies of collision, the objects have high energy so they tend to be very close to each other. To distinguish two very close objects, such as a lepton and the closest jet (track), we define the distance between them by $dR(l, track) < K/p_T^l$, where K is a scale parameter. Studies for 8 TeV collisions [68], show that the best performance has been achieved for a scale parameter of K = 10 GeV, giving an electron mini isolation of $MI_{10}^e < 0.05$.

4.3.4 Muon objects

A chain of triggers, similar to the one used for electrons exist for muon reconstruction. The muons are identified initially by the $L1$ trigger, using the Muon Spectrometer, and they are further analyzed by the next trigger levels, using the Inner Detector tracks. The sub-detectors resolutions are taken into account by the muon triggers to reconstruct the muon momentum and charge. The single muon triggers, used in the analyses shown in this thesis, are EF_MU24I_TIGHT and EF_MU36I_TIGHT. These triggers differ by the p_T threshold criteria, which is 24 GeV for the first one against 36 GeV in the second trigger. Also, the isolation requirement in EF_MU24I_TIGHT trigger is to consider a cone, of size $dR = 0.2$, around the muon in which the p_T sum of the tracks is less than 12% of the muon p_T ($p_T^{0.2}/p_{T,\mu} < 0.12$). But, any isolation requirement is made in the EF_MU36I_TIGHT [9] trigger. Thus, we apply to the muon the same mini isolation used for the electrons: $MI_{10}^{\mu} < 0.05$. The ATLAS Muon group defines three types of muon events, according to the sub-detectors used to reconstruct the muon objects. Muon events that are reconstructed only by the Muon Spectrometers, without any matching to the Inner Detector track, are called Standalone Muons. While, muons which have an Inner Detector track, that can be associated with straight track segments in the Muon Spectrometer, are called Segment Tagged Muons (ST). However, the muons used in this thesis, have a track reconstruction performed separately in the inner Detector and the Muon Spectrometer: these two tracks can be combined so the muon object is called Combined Muon (CB).

A muon identification (muid) algorithm [70] has been used, for the muon objects reconstructions, which consists of a combined muon selection within the detector acceptance of pseudo-rapidity of $|\eta| < 2.5$. Next, the events containing a muon object with a transverse momentum p_T lower than the trigger efficiency threshold, set to 25 GeV, are rejected. Also, muon objects must pass the MCP identification track quality cuts. Finally, the longitudinal impact parameter relative to the primary vertex (z_0) is

[9] In EF_MU36I_TIGHT: μ stands for muons, the subsequent number (24 and 36) is the p_T threshold in GeV and tight is for identification.

required to be less than 2 mm, and the transverse impact parameter significance relative to the primary vertex is required to be: $d_0/\sigma_{d_0} < 3$.

4.3.5 Jet objects

The physics object corresponding to a parton, causing a hadronic cascade [10], is called a jet. A jet carries the quark type name, so in the case of a quark bottom, we will look forward to reconstruct a b-jet (see section 4.3.6). A jet is represented by a cone of radius R, centred around the jet axis, and containing the hadronic cascade of particles (each of which is represented by a black arrow in the figure). Different jet clustering algorithms can be used to reconstruct jet objects. The first step of any jet clustering algorithm is to determine the distances d_{ij} and d_{iB} defined by formulas 4.12 and 4.13 [71], respectively. The first one is the distance between entities i and j (such as particles, pseudo-jets), while the second one is the distance between entity i and the beam B.

$$d_{ij} = min(\, k_{tj}^{2p} \,,\, k_{ti}^{2p} \,)\, \frac{\Delta_{ij}^2}{R^2}, \tag{4.12}$$

$$d_{iB} = k_{ti}^{2p}, \tag{4.13}$$

where $\Delta_{ij}^2 = (\eta_i - \eta_j)^2 + (\phi_i - \phi_j)^2$, k_{ti}, η_i and ϕ_i are the transverse momentum, rapidity and azimuthal of particle i, respectively. In addition to the radius parameter R, a parameter p is added to govern the relative power of the energy versus geometric (Δ_{ij}) scales. Three distinct algorithms arise from different values of the p parameter: the k_t algorithm if $p = 1$, the Cambridge/Aachen algorithm for $p = 0$ and the case of $p =$ -1 corresponds to the anti-k_t algorithm [71, 72].

Once these distances are calculated, the clustering algorithm proceeds by identifying the shortest of these two distances: if $d_{ij} < d_{iB}$, then, entities i and j are recombined. However, if the shortest distance is d_{iB}, then, i is called a jet, removed from the list of entities, its four-momentum is calculated and the value of the radius R related to that jet is saved. The process is repeated until there is no entity left. Finally, the FastJet software [73] is used to implement the chosen jet algorithm.

In the ATLAS experiment, jets are detected as groups of topologically related energy deposits in nearby clusters in the Calorimeters (called calorimeter jets) or as tracks for charged particles in the tracking chambers (called track jets) [74].

In the present analyses, calorimeter jets are reconstructed with the anti-k_t algorithm, using the topological clusters [11] which energy is compensated for the presence of hadronic activity, using Local

[10] Standard model quarks interact through the strong force and cause cascades of particles.

[11] A cluster is a set of calorimeter cells which contain the energy of the jet (the hadronic cascade). Topo-cluster energy is either calibrated, to the electromagnetic scale (EM), or compensated for the presence of hadronic activity, using local cluster weights (LCW). The EM scale is defined by unit response to electromagnetic particles, e.g., photons and electrons.

Cluster Weights (LCW). The LCW calibration classifies clusters as electromagnetic or hadronic. Then, applies calibration accordingly, by taking into account the energy lost, due to the non-compensation [12] and non-instrumented regions of the calorimeters, as well as noise suppression. Thus, Monte Carlo simulation-based, (p_T, η) dependent, correction factors have been used for jet calibration. For the present analyses, we used a Monte Carlo sample of MC12a that was produced with PYTHIA generator and inclusive QCD jet events.

Furthermore, a Jet Energy Scale (JES) calibration is used, at the electromagnetic scale, to apply corrections as a function of the jet transverse momentum and pseudo-rapidity. This calibration is called EM+JES, and consists of pile-up correction, vertex correction as well as jet energy and direction correction [75, 76]. A total of 47 nuisance parameters are available from in-situ analysis of the 2012 dataset. That number is reduced to 12 by using a matrix diagonalization technique. More detail can be found in [77].

It would be interesting to collect information about the origin of the particles that form a reconstructed calorimeter jet object. To do so, we can associate either tracks or simulated truth particles with the jets [74]. The associated tracks are in fact track jets initiated by charged particle tracks originating from the hard-scatter primary vertex. These tracks have to satisfy minimal quality criteria such as the number of hits in the Pixel and SCT detectors. As for truth jets, they are reconstructed in Monte Carlo simulations from the stable interacting particles in the final state of the strong interaction in a simulated event [13]. In physics analyses, the efficiency with which truth jets or track jets are matched to the calorimeter jets is called the jet reconstruction efficiency [77]. Because track jets and calorimeter jets are reconstructed by independent ATLAS sub-detectors, a good agreement between data and Monte Carlo simulation means that the absolute jet reconstruction efficiency can be determined from the simulation [78, 79]. In the current analyses, the small observed difference between data and Monte Carlo simulation was applied to Monte Carlo simulation events by discarding a fraction of jets taken at random within the inefficiency range of $p_T < 30$ GeV. The uncertainty on the jet reconstruction efficiency is also taken into account. The Jet Energy Resolution (JER) was also measured [77, 79], and jets were smeared when calculating the systematic uncertainty.

After the JES calibration, a small contamination of pile-up jets remains, so a track-based algorithm has been developed by ATLAS collaboration. This algorithm uses a variable, called Jet Vertex Fraction (JVF), to identify the primary vertex from which the jet is born. The Primary Vertex (PV) is calculated as the vertex associated with the highest sum of tracks squared transverse momenta ($\sum_{\text{track}} p_T^2$) for all tracks associated with that vertex. For each jet, the JVF value is calculated [76, 80] as the ratio of the scalar sum of the p_T of matched tracks, that originated from a given hard-scatter primary vertex, to

[12] ATLAS Calorimeter non-compensating means that the Calorimeters lead only to a partial measurement of the energy deposited by hadrons.

[13] Truth particles are considered stable if their decay length is greater than 1 cm. However, a truth particle is considered to be interacting if it is expected to deposit most of its energy in the ATLAS calorimeters excluding muons and neutrinos which are considered to be non-interacting.

the scalar sum of the p_T of all matched tracks in the jet, independently of their origin. A cut on the JVF variable will help to remove most of the jets which are not associated with the hard-scatter primary vertex and have passed the JES calibration. The efficiency of the JVF selection requirement is measured from the data/MC simulation comparison of Z+jets events, with specific selections, to obtain a sample of scatter jets (in which Z boson decays into a pair of electrons) [75].

Furthermore, jet quality criteria are applied to identify jets which are not produced by in-time real jet energy deposits in the Calorimeters. These jets, called bad jets, arise from various sources such as hardware problems in the calorimeter, LHC beam-gas interactions and cosmic-ray induced showers. A loose minus/looser selection is then used to reject these jets [81]. For the purposes of the analyses made in this thesis, we use a criteria called isBadLooseMinus [82]. The isBadLooseMinus consists of the selection of jets [14] in the detector regions of $|\eta| > 2.5$ with positive energy ($E > 0$) and transverse momentum greater than 20 GeV.

In the present analyses, the jet radius parameter used was either $R = 0.4$ or $R = 1.0$, referred to as small-R jets and large-R jets, respectively. We used, for both types of jets, the inclusive anti-k_t algorithm implemented in FAST-JET2.4.2P5 [83] and the E-scheme cluster recombination algorithm. The small-R jets (denoted as j) are required to have p_T (j) > 25 GeV, be within the detector region of $|\eta| < 2.5$. The small-R jets of p_T (j) > 50 GeV from the regions of $|\eta| < 2.4$ should pass the JVF cut of |JVF| > 0.5 to reduce the in-time pile-up effect, especially when it comes to the muon-jet overlap removal (see section 4.3.7 for more detail). The highest p_T and closest small-R jet to the selected lepton is called the *selected jet* and denoted as j_{sel}. Events without at least one *selected jet* are rejected.

For large-R jets (denoted as J), Jet trimming algorithm [84] is used to remove low energy clusters that are formed by pile-up and initial state radiation. This algorithm reconstructs, inside the large-R jet, sub-jets with a radius of $R_{\text{sub jets}} = 0.3$. Also sub-jets with a transverse momentum of $p_T < f_{\text{cut}}\,\Lambda_{\text{hard}}$ are discarded. In the analyses shown in this thesis, $f_{\text{cut}} = 0.05$ and Λ_{hard} is the transverse momentum of the original large-R jet [85]. A study of the large-R jet substructure leads to the re-clustering of the jet constituents with the previous k_t algorithm and a d_{ij} value (see equation 4.12) called the first splitting scale $\sqrt{d12}$. This observable is used in these analyses to select jets generated by heavy particle decay.

For two body decay, this value is expected to have the value of half the mass of the original particle which is usually heavy. In these analyses, selected large-R jets are required to have a transverse momentum larger than 300 GeV, a mass greater than 100 GeV, be within the detector region (pseudo-rapidity range) of $|\eta| < 2.0$, with a distance from the selected jet (j_{sel}) and the selected lepton (l) as follows: $\Delta R\,(\,Lj\,,\,j_{\text{sel}}\,) > 1.5$ and $\Delta\phi\,(\,Lj\,,\,l\,) > 2.3$. Furthermore, the first splitting scale is set to be greater than 40 GeV.

Finally, we will keep the events which contain at least one small-R jet generated from a bottom quark called b-jet. The identification of these jets is called b-tagging and is very important because b-jet

[14] The isBadLooseMinus cut is applied only on small-R jets.

selection makes sure that a selected event contains, on the one hand, a top quark [15] and on the other hand, is free of backgrounds.

4.3.6 The b-tagging algorithms

Earlier, we described the small-R jet reconstruction and the selection part of the process used in the analyses presented in this thesis. However, it is important to take into account the origin of the production of these jets: they are produced in many ways such as hadronization (of SM up, down or strange quarks), decay of high momentum particles (like the Higgs boson, SM top quark and composite particles). The study of heavy gluon decay, illustrated by figure 3.4, encourages looking for the analyses of events containing at least one SM top quark. Hence, the identification of small-R jets containing b-quarks is based on their properties. First, b-hadrons have a long lifetime ($\sim 10^{-12}$ second) compared to the other light hadrons [16], resulting in a significant flight path length from which are measured secondary vertices and impact parameters (both longitudinal z_0 and transverse d_0) of the decay products.

The algorithm chosen for b-tagging is MV1 tagger [86]. This algorithm uses calorimeter jets and reconstructed tracks in the Inner Detector. The primary vertex is selected from the primary vertices reconstructed from two or more of the latter tracks [87]. Then, tracks are associated with the calorimeter jets based on their distances. A working point of 70% corresponding to a cut on the MV1 weight larger than 0.7892 is chosen for the present analyses. More detail about b-tagging algorithm as well as scale factors and uncertainties can be found in reference [86–88].

4.3.7 Overlap removal

When a heavy particle is produced with high transverse momentum, its decay products get to be very close to each other [17]. As a consequence, sometimes the decay may not be distinguished from one and another during a physics analysis. This phenomenon could not be neglected for the proton-proton collisions at the center of mass energy as much as 8 TeV. In particular, when a lepton is misidentified as jets, then, we are in the case of lepton-jets overlap. The following selection criteria from [65] will help to remove this kind of overlap, so double counting is avoided and the particle identification efficiency is increased.

[15] The top quark decays mostly into a W boson and a bottom quark.

[16] Hadrons coming from a c-quark hadronization are called c-jets, while jets originated from u, d, s quarks or gluons are jointly called light-hadrons (or light-jets).

[17] Let us consider a heavy gluon decaying into a SM top quark, with a mass of
173.3 GeV, and a 600 GeV vector like top quark. The heavy gluon mass excess is transferred to its products transverse momenta, so the latter two top quarks will have much higher transverse momenta if they are products of a 2 TeV heavy gluon compared to a 1 TeV gluon.

Electrons and jets overlap:

- If the selected electron [18] is within a cone of $\Delta R(\text{e}, \text{jet}) < 0.4$ of the nearest jet, the electron is marked and the jet as needing to undergo overlap removal.
- Removal of the selected electron within a cone of $\Delta R(\text{e}, \text{jet}) < 0.2$ from a *selected jet* [19]. If that jet was marked, then, the electron is considered to be a jet and is added to the jet four-vector.
- If the jet was marked, then, the $\Delta R(\text{e}, \text{jet})$ is calculated via the subtracted jet four vector.

Muons and jets overlap:

- Removal of any selected muon [20] that is within a cone of $\Delta R(\mu, \text{jet}) < 0.4$ of any *selected jet*.
- Removal of the non-prompt muons, e.g., muons within $\Delta R(\mu, \text{jet}) < (0.04 + 10 \text{ GeV})/p_T^{\mu}$ to a small-R jet with a transverse momentum greater than 25 GeV and |JVF| > 0.5.
- Rejection of jets which are in the detector region of $|\eta| > 2.5$, have a transverse momentum smaller than 25 GeV and do not pass JVF cut.

4.3.8 Missing transverse momentum

In a hadron collider event, the measurement of the missing transverse momentum is defined as the imbalance of the total transverse momentum. As seen in schema 4.14, each of the four black arrow represents an observed particle momentum. In the calculation of the total transverse momentum, the vector sum of their momenta (as done in the right hand-sided figure) is computed by attaching each vector on the tip of the previous one. This leads to an open black polygon because of a missing arrow-particle. The missing transverse momentum is then estimated by the dashed green arrow. This imbalance corresponds to particles undetectable by the ATLAS detector such as SM neutrinos or new weakly-interacting particles. As an illustration, figure 4.15 is a display, in ATLAS detector, of a Higgs boson candidate event. In the final state are reconstructed a muon (light-blue line), an electron (red line) and a missing transverse momentum as the sum of momenta of their respective neutrinos (dashed white lines). These particles have been produced through the Higgs decay into double W bosons.

In the analyses presented in this thesis, the undetected(missing) particle is the neutrino which has been produced in association with muon or electron by W-boson decay . The physics object corresponding to the magnitude of the missing transverse energy is denoted as E_T^{miss} and is defined as

[18] A selected electron is an electron which passed the object selection criteria listed in the section 4.3.3
[19] A selected jet matches the jet object selection criteria from section 4.3.5
[20] A selected muon is a muon which passed the object selection criteria listed in section 4.3.4

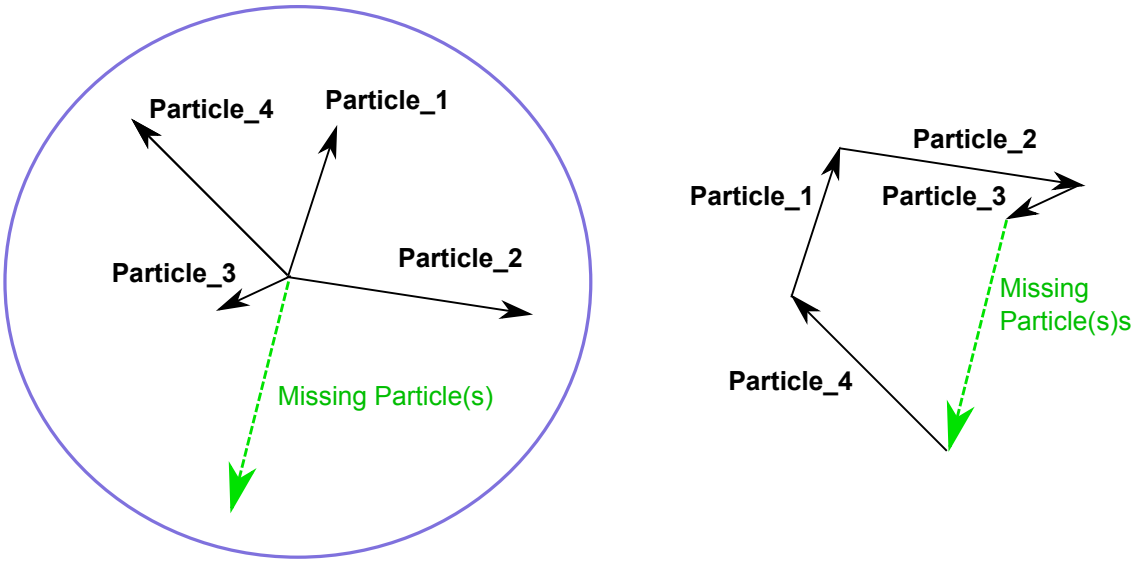

Figure 4.14: Left plot: In a transverse view of the detector (such that beams punch orthogonally through the page), each black arrow represents an observed particle momentum: the longer the arrow, the larger the momentum. Right plot: The vector sum of the particles momenta (from the right plot) is computed by attaching each vector on the tip of the previous one forming a black open polygon. To close the polygon, a dashed green arrow is drawn which stands for the missing particle(s) momentum (in both right and left plots). In physics analyses, the dashed green line is called missing transverse momentum [14].

the sum of the contributions of the imbalance of the energy deposits in the calorimeters and the muons reconstructed in the Muon Spectrometer [89]:

$$E_{x(y)}^{\text{miss}} = E_{x(y)}^{\text{miss, calo}} + E_{x(y)}^{\text{miss, }\mu}. \tag{4.14}$$

leading to the total missing transverse momentum, called missing energy transverse, and defined as follows:

$$E_T^{\text{miss}} = \sqrt{(E_x^{\text{miss}})^2 + (E_y^{\text{miss}})^2}. \tag{4.15}$$

The calorimeter term of E_T^{miss} is reconstructed from calibrated calorimeter cells associated with reconstructed and identified high transverse momentum (high-p_T) objects. These objects are, in order of importance: electrons, photons, hadronically decaying τ-leptons, jets and muons. For an improved missing transverse momentum resolution, the calorimeter cells which are not associated with any such objects are taken in account and their contribution is named $E^{\text{miss, CellOut}}$. The full calorimeter term is

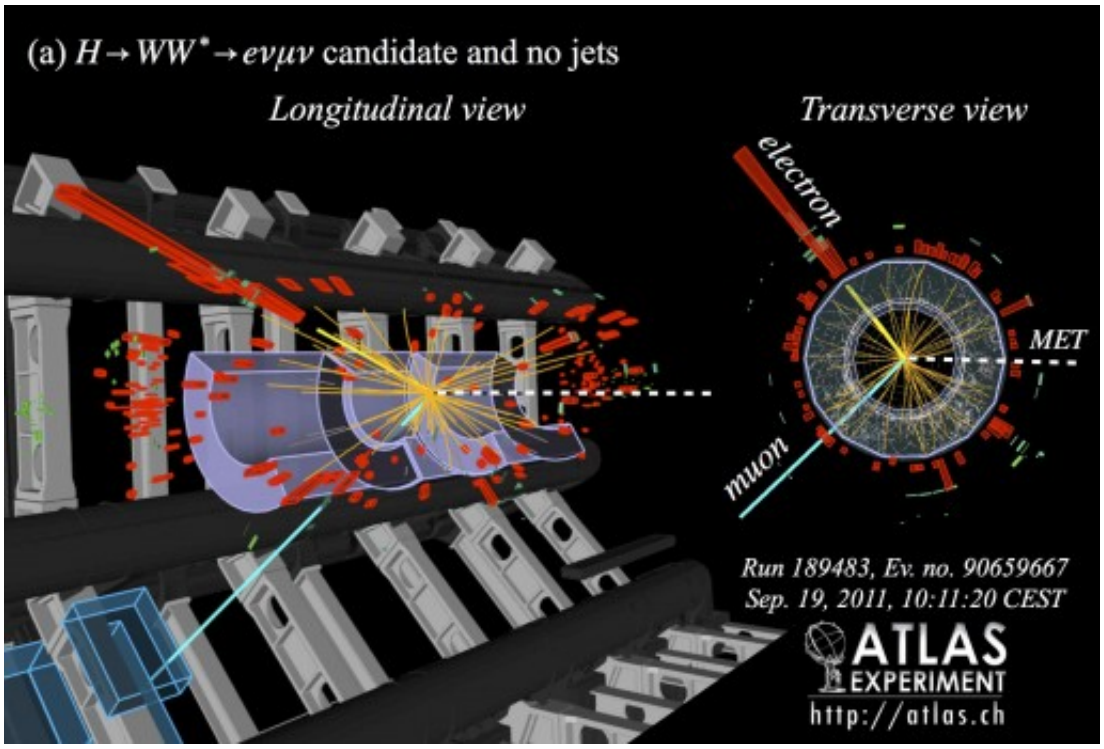

Figure 4.15: Display of a Higgs boson candidate event as reconstructed in the ATLAS detector. This Higgs boson decays into two W bosons leading to two leptons and their neutrinos leptonic as $H \to WW \to e\nu\mu\nu$. The invisible neutrinos are represented by missing transverse momentum denoted as MET (dashed lines) that point away from the electron-muon system.

then defined as [89]:

$$\begin{aligned} E_{x(y)}^{\text{miss, calo}} = E_{x(y)}^{\text{miss, electrons}} + E_{x(y)}^{\text{miss, photons}} + E_{x(y)}^{\text{miss, }\tau} \\ + E_{x(y)}^{\text{miss, jets}} + E_{x(y)}^{\text{miss, soft-jets}} + E_{x(y)}^{\text{miss, calo,}\mu} \\ + E_{x(y)}^{\text{miss, CellOut}} \end{aligned} \tag{4.16}$$

where the soft-jets term is calculated in cells for clusters associated with jets that have a low transverse momentum (between 10 GeV and 20 GeV) and each term is the negative of the sum of calibrated cell energies inside the objects as follows:

$$E_x^{\text{miss, term}} = -\sum_{i=1}^{\text{Nterm cell}} E_i \sin\theta_i \cos\phi_i, \tag{4.17a}$$

$$E_y^{\text{miss, term}} = -\sum_{i=1}^{\text{Nterm cell}} E_i \sin\theta_i \sin\phi_i, \tag{4.17b}$$

where E_i , θ_i and ϕ_i stand for the energy, the polar angle and the azimuthal angle of the i^{th} cell of each object within the pseudo-rapidity range of $|\eta| < 4.5$, respectively. In addition, an appropriate Noise-removal criteria, listed in reference [89], is applied to reduce the effect of the noise due to the high granularity of the ATLAS Calorimeter.

The muon term of E_T^{miss} is reconstructed [89] by using the transverse momentum of combined muons. These objects correspond to muons reconstructed in the Muon Spectrometer with a matched track in the Inner Detector. However, muons deposit a part of their energy in the Calorimeters so the muon term is calculated differently for isolated and non-isolated muons. Isolated muons are considered to be within a distance $\Delta R(\,\mu\,,\,\text{jet}\,) < 0.3$ of a reconstructed jet in the event. Unlike non-isolated muons, the energy lost by isolated muons is included in the muon term of E_T^{miss}, so the term $E_{x(y)}^{\text{miss},\,\text{calo},\mu}$ is not added to the calorimeter term defined by the equation 4.16 to avoid double counting of energy. Considering only the muon tracks within the detector region of $|\eta| < 2.7$, the muon term of E_T^{miss} is calculated by adding negative of their transverse momentum components as in:

$$E_{x(y)}^{\text{miss},\,\mu} = -\sum_{\text{muons}} p_{x(y)}^{\mu}. \tag{4.18}$$

The E_T^{miss} calibration and performance have been made by an earlier study that can be found in reference [89].

Finally, in the analyses presented in this thesis, missing transverse energy was reconstructed using MET_RefFinal_tightpp tool. This tool is used to reconstruct the physics objects regarding event criteria presented in this section. A selection criteria on the missing transverse energy will help to remove misidentified leptons (also referred to as fake leptons). More details can be found in chapter 5.

5 Searches for heavy gluons in the single lepton channel

5.1 Data sample

The dataset used during this analysis are from the All-Good run list (GRL) that contains the runs and the luminosity blocks (LB) during which ATLAS detector and LHC beam conditions were stable. The dataset has been arranged into ten data-taking times tagged by run periods A to L (with the periods F and K excluded due to the bad data quality). These data were recorded from 2012 proton-proton collisions at center of mass energies of $\sqrt{s}=$ 8 TeV with a time between successive bunch of collisions of 25 ns. A total integrated luminosity of 20 fb^{-1} was delivered and was certified to be good quality data for physics (as shown by figure 5.1 taken from ref [90]).

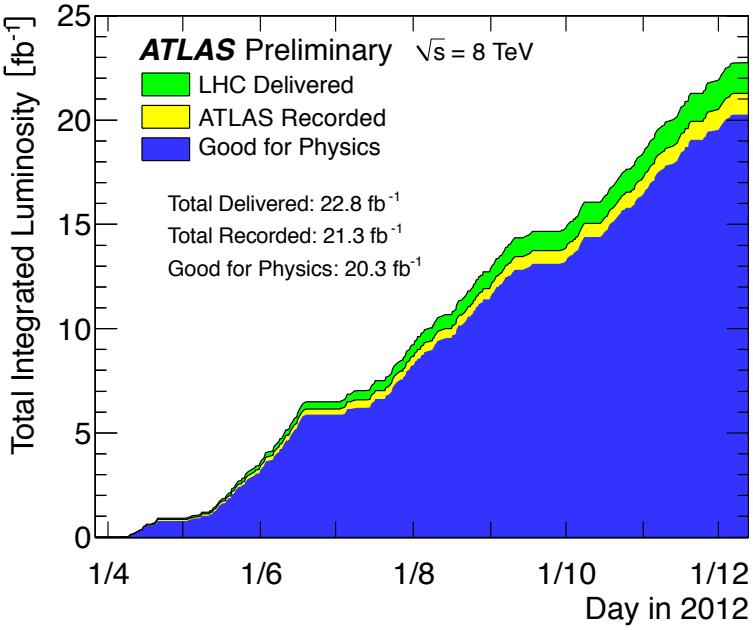

Figure 5.1: Total Integrated Luminosity and Data Quality in 2012 [11]. Cumulative luminosity versus time delivered to (green), recorded by ATLAS(yellow), and certified to be good quality data (blue) during stable beams and for pp collisions at 8 TeV centre-of-mass energy in 2012. The delivered luminosity accounts for the luminosity delivered from the start of stable beams until the LHC requests ATLAS to put the detector in a safe standby mode to allow a beam dump or beam studies. The recorded luminosity reflects the DAQ inefficiency, as well as the inefficiency of the so-called "warm start": when the stable beam flag is raised, the tracking detectors undergo a ramp of the high-voltage and, for the pixel system, turning on the preamplifiers. The data quality assessment shown corresponds to the All Good efficiency shown in the 2012 Data Quality table. The luminosity shown represents the preliminary 8 TeV luminosity calibration. Data quality has been assessed after reprocessing.

5.2 Heavy gluon simulated samples

5.2.1 Cross Sections for all the $\mathrm{g_{KK}} \rightarrow \mathrm{tT}$ samples

The Monte Carlo (MC) samples have set a cross-section limit to show exclusion/discovery regions in the present analysis. Therefore for several points in the heavy gluon and VLQ top mass ($m_{g_{KK}}$ and m_T respectively) region, the cross sections has been calculated for each g_{KK} decay channel:
pp $\rightarrow$ g_{KK} $\rightarrow$ tT $\rightarrow$ t $Wb/tZ/tH$, where, H is a composite Higgs boson and T is a VLQ top. Events have been generated with MADGRAPH5 via GTBMOD_UFO using the Model provided by J Santiago and M Chala [91] for g_{KK} (also implemented in madgraphControl for on-the-fly production) and the CTEQ6L1 PDF set is used for the generation. The parameters are chosen to match those of the scenario described in section 3.3. However, we used a simplified version of the composite Higgs models [9], and set the light quark coupling to g_{KK} with the mixing angle $\tan\theta_3 = 0.3$, as seen in Table 5.1, and then, we changed the $g_{KK} \rightarrow tT$ coupling to fix the total decay width of heavy gluon, $\Gamma(g_{KK})$ to be in the range of 1, 10 and 30 percent of the g_{KK} mass. The value of 10% is the same order of magnitude as the expected experimental resolution. Furthermore, for each point in ($m_{g_{KK}}$, m_T) regions, 8 TeV p-p collisions have been simulated and 10000 events selected.

As an illustration, we provide the cross sections in Tables 5.2, 5.3 and 5.4 for VLQ top decaying into Wb, tZ and tH respectively (each channel has been produced separately). For example, in the second line of table 5.2, from left to right, to region ($m_{g_{KK}}$, m_T) = (1.5 TeV, 0.8 TeV) corresponds a Branching Ratio of BR = 0.459 giving a cross section of 0.229 pb for decay width of $\Gamma(g_{KK})/m_{g_{KK}} = 1\%$.

Table 5.1: Parameters used for $g_{KK} \to Tt$ MC production. The mixing angle was set to $\tan\theta_3 = 0.3$ then the $g_{KK} \to tT$ coupling, g_{trTr}, was changed to fix the total decay width of heavy gluon, $\Gamma(g_{KK})$ to be in the range of 1%, 10% and 30% of the g_{KK} mass. The error on each calculated cross section is less than 0.1%.

Process $g_{KK} \to Tt$		g_{KK} coupling to tT (g_{trTr})		
$m_{g_{KK}}$ (TeV)	m_T (TeV)	$\Gamma(g_{KK})/m_{g_{KK}}$ = 1%	$\Gamma(g_{KK})/m_{g_{KK}}$ = 10%	$\Gamma(g_{KK})/m_{g_{KK}}$ = 30%
1.0	0.6	1.106	4.113	7.196
1.5	0.8	0.969	3.604	6.306
	1.0	1.224	4.553	7.967
	1.2	1.942	7.223	12.639
2.0	1.4	1.306	4.857	8.498
	1.6	1.847	6.869	12.020
	1.8	4.523	16.819	29.428
2.5	1.4	0.992	3.690	6.457
	1.8	1.367	5.085	8.898
	2.0	1.814	6.747	11.806
	2.2	3.021	11.234	19.656

Table 5.2: Cross sections for each point in ($m_{g_{KK}}$, m_T) for $T \to Wb$ channel.The mixing angle was set to $\tan\theta_3 = 0.3$ then the $g_{KK} \to tT$ coupling was changed to fix the total decay width of heavy gluon, $\Gamma(g_{KK})$ to be in the range of 1, 10 and 30 percent of the g_{KK} mass. The error on each calculated cross section is less than 0.1%.

Process $T \to Wb$			Cross Section: σ(pp $\to g_{KK}$) $\times$ BR ($g_{KK} \to tT \to tWb$)(pb)		
$m_{g_{KK}}$ (TeV)	m_T (TeV)	Branching Ratio	$\Gamma(g_{KK})/m_{g_{KK}}$ = 1%	$\Gamma(g_{KK})/m_{g_{KK}}$ = 10%	$\Gamma(g_{KK})/m_{g_{KK}}$ = 30%
1.0	0.6	0.546	2.220	2.689	2.086
1.5	0.8	0.459	0.229	0.289	0.231
	1.0	0.457	0.228	0.268	0.199
	1.2	0.456	0.225	0.257	0.202
2.0	1.4	0.509	0.040	0.047	0.033
	1.6	0.507	0.040	0.044	0.031
	1.8	0.455	0.041	0.063	0.062
2.5	1.4	0.456	0.006	0.008	0.007
	1.8	0.455	0.006	0.007	0.005
	2.0	0.455	0.006	0.007	0.004
	2.2	0.455	0.006	0.007	0.005

Table 5.3: Cross sections for each point in ($m_{g_{KK}}$, m_T) for $T \to tZ$ channel.The mixing angle was set to $\tan\theta_3 = 0.3$ then the $g_{KK} \to tT$ coupling was changed to fix the total decay width of heavy gluon, $\Gamma(g_{KK})$ to be in the range of 1, 10 and 30 percent of the g_{KK} mass. The error on each calculated cross section is less than 0.1%.

Process $T \to tZ$			Cross Section: σ(pp $\to g_{KK}$) $\times$ BR ($g_{KK} \to tT \to ttZ$)(pb)		
$m_{g_{KK}}$ (TeV)	m_T (TeV)	Branching Ratio	$\Gamma(g_{KK})/m_{g_{KK}}$ = 1%	$\Gamma(g_{KK})/m_{g_{KK}}$ = 10%	$\Gamma(g_{KK})/m_{g_{KK}}$ = 30%
1.0	0.6	0.206	0.847	1.016	0.788
1.5	0.8	0.290	0.146	0.182	0.146
	1.0	0.305	0.152	0.179	0.133
	1.2	0.313	0.155	0.176	0.138
2.0	1.4	0.239	0.019	0.022	0.016
	1.6	0.240	0.019	0.021	0.015
	1.8	0.323	0.029	0.044	0.044
2.5	1.4	0.318	0.004	0.006	0.005
	1.8	0.323	0.004	0.005	0.003
	2.0	0.325	0.004	0.005	0.003
	2.2	0.326	0.005	0.005	0.004

Table 5.4: Cross sections for each point in ($m_{g_{KK}}$, m_T) for $T \to tH$ channel. The mixing angle was set to $\tan\theta_3 = 0.3$ then the $g_{KK} \to tT$ coupling was changed to fix the total decay width of heavy gluon, $\Gamma(g_{KK})$ to be in the range of 1, 10 and 30 percent of the g_{KK} mass. The error on each calculated cross section is less than 0.1%.

Process $T \to tH$			Cross Section: σ(pp $\to g_{KK}$) $\times$ BR ($g_{KK} \to tT \to ttH$)(pb)		
$m_{g_{KK}}$ (TeV)	m_T (TeV)	Branching Ratio	$\Gamma(g_{KK})/m_{g_{KK}}$ = 1%	$\Gamma(g_{KK})/m_{g_{KK}}$ = 10%	$\Gamma(g_{KK})/m_{g_{KK}}$ = 30%
1.0	0.6	0.248	1.015	1.219	0.947
1.5	0.8	0.251	0.127	0.158	0.127
	1.0	0.238	0.119	0.140	0.104
	1.2	0.231	0.116	0.131	0.102
2.0	1.4	0.252	0.020	0.023	0.017
	1.6	0.252	0.020	0.022	0.016
	1.8	0.221	0.022	0.032	0.031
2.5	1.4	0.226	0.003	0.004	0.003
	1.8	0.221	0.003	0.003	0.002
	2.0	0.220	0.003	0.003	0.002
	2.2	0.219	0.003	0.004	0.003

5.2.2 Generation and validation

Validation of single VLQ top production via Heavy Gluons has been performed via a study focused on samples of $m_{g_{KK}} = 1.0$ TeV, $m_T = 0.5$ TeV and Width of 10 %.

MADGRAPH+PYTHIA or MADGRAPH only: tWb channel

We compare two samples. The first one (MADGRAPH+PYTHIA8 in red) is produced by decaying heavy Gluon and VLQ top in MADGRAPH. Then SM top quark and the last generation particles are decayed automatically by PYTHIA8. However, for the second sample (MADGRAPH, in blue) we make sure that SM top quark also decay via MADGRAPH.

For both samples, the heavy gluon, as seen in Figure 5.2b, decays 50% into a top and 50% into an anti-top quark. In each case the decay particle is produced in association with a vector like anti-top or top quark. The VLQ top are not shown because of their large pdgid (999002). As first generation of particles according to g_{KK} decay chain from Figure 3.4, we checked top quark and VLQ top characteristics such as their multiplicity, their transverse momentum, top quark rapidity and the PID of the products of their decays (considered as the second generation of particles in g_{KK} decay chain) in Figures 5.3 and 5.4.

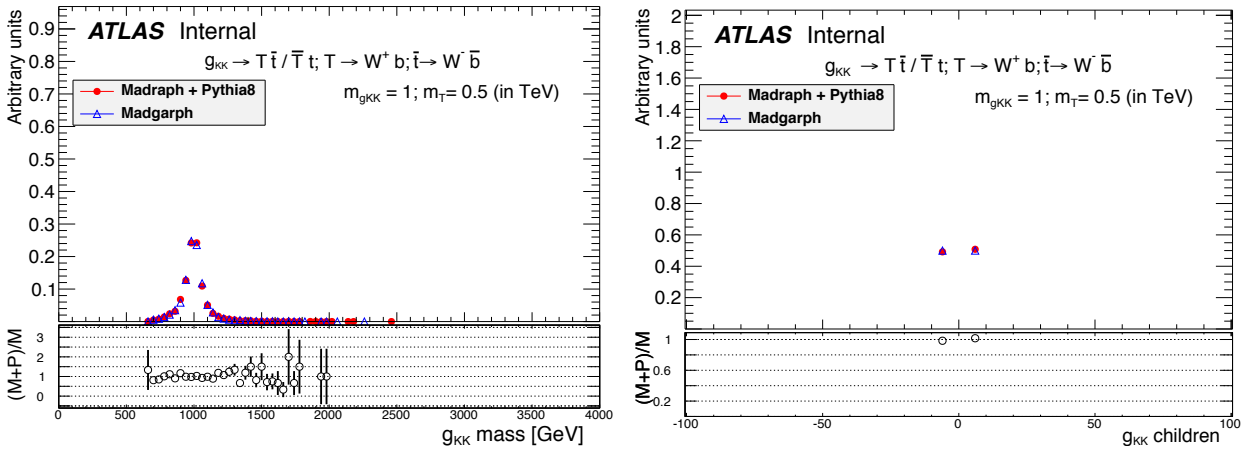

(a) Heavy gluon mass in GeV.

(b) Heavy gluon children.

Figure 5.2: Heavy Gluon (g_{KK}) mass and its children, with $m_{g_{KK}} = 1.0$ TeV, $m_T = 0.5$ TeV, $\tan\theta_3 = 0.3$ and $\Gamma(g_{KK})/m_{g_{KK}} = 10$ %.

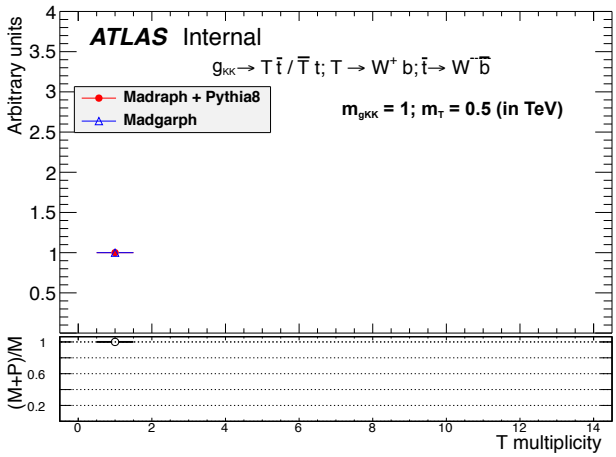

(a) The multiplicity of decayed VLQ top.

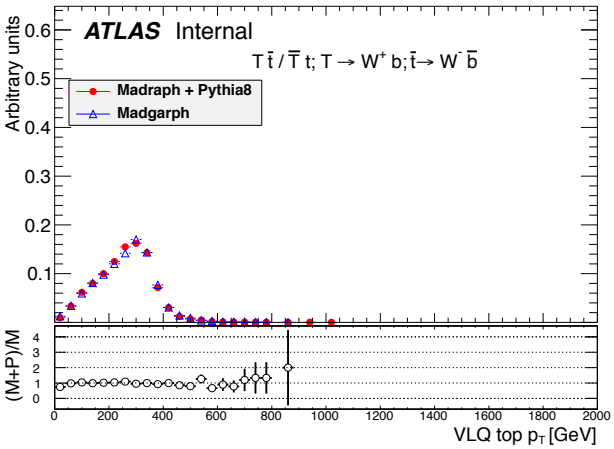

(b) VLQ top transverse momentum.

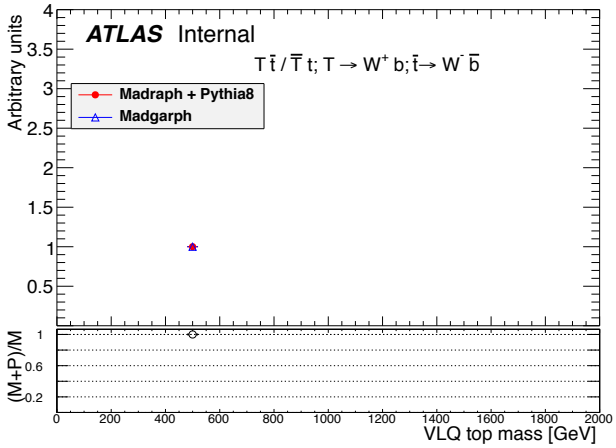

(c) VLQ top mass.

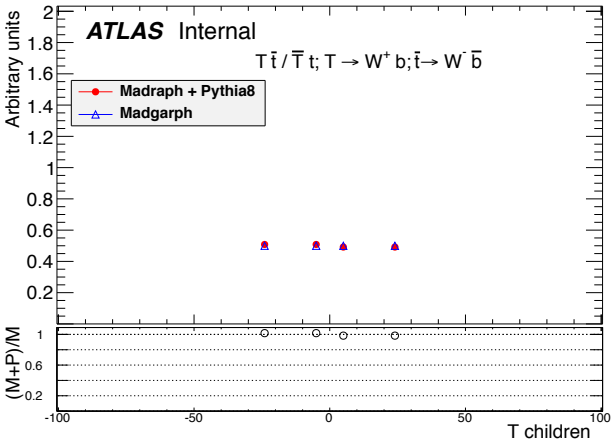

(d) The decay products of VLQ top.

Figure 5.3: First generation of particles according to g_{KK} decay chain visible in Figure 3.4, with $m_{g_{KK}} = 1.0$ TeV, $m_T = 0.5$ TeV, $\tan\theta_3 = 0.3$ and $\Gamma(g_{KK})/m_{g_{KK}} = 10$ %.

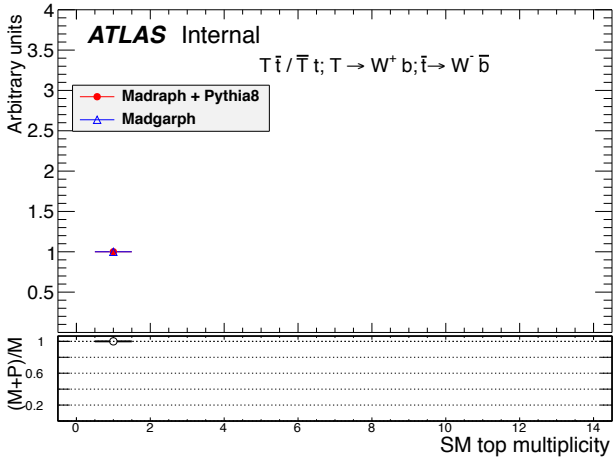

(a) The multiplicity of decayed SM top quark.

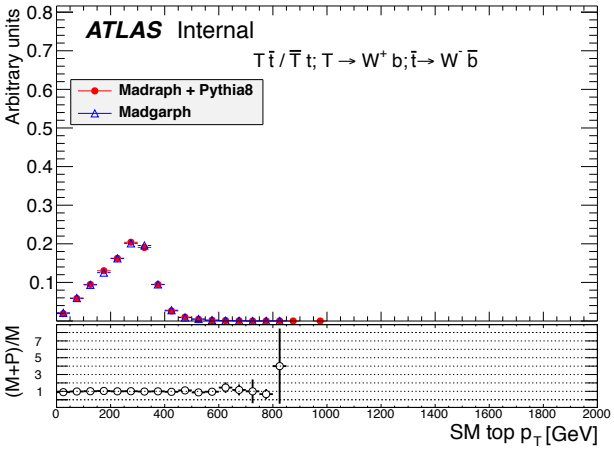

(b) SM top quark transverse momentum.

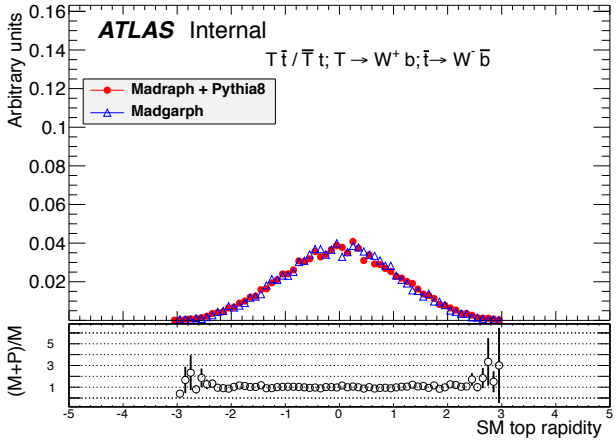

(c) SM top quark rapidity.

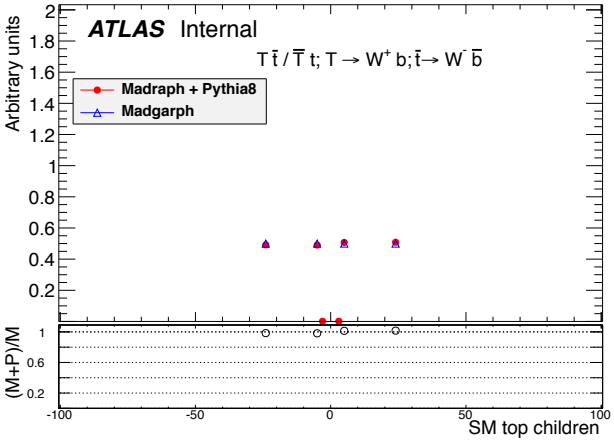

(d) The decay products of SM top quark.

Figure 5.4: First generation of particles according to g_{KK} decay chain from Figure 3.4: SM top quark, with $m_{g_{KK}} = 1.0$ TeV, $m_T = 0.5$ TeV, $\tan\theta_3 = 0.3$ and $\Gamma(g_{KK})/m_{g_{KK}} = 10$ %.

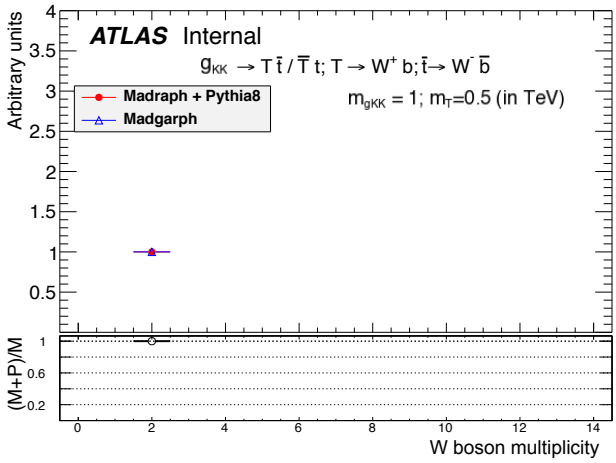

(a) Number of decayed W Boson.

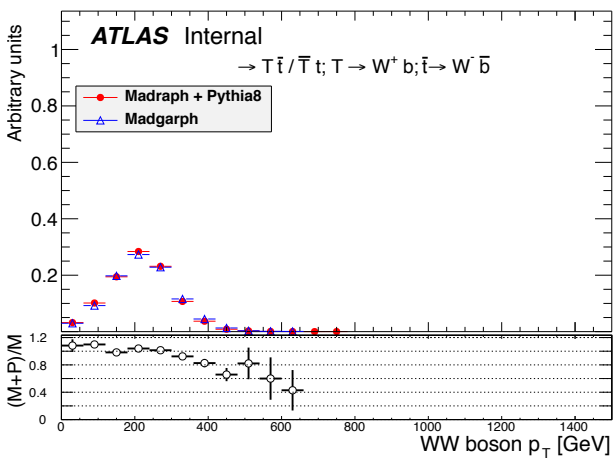

(b) Diboson $p_T(WW)$.

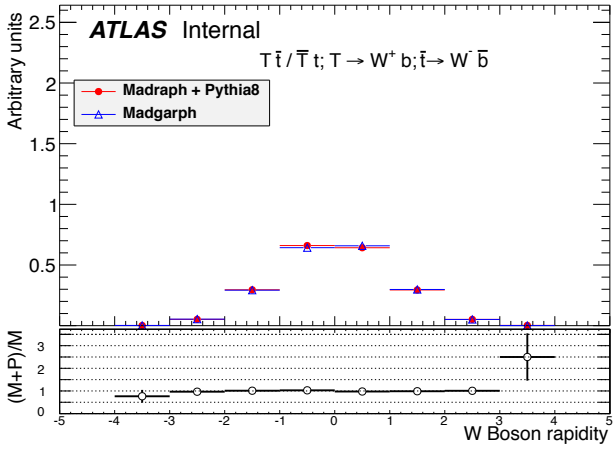

(c) W Boson rapidity (y_W).

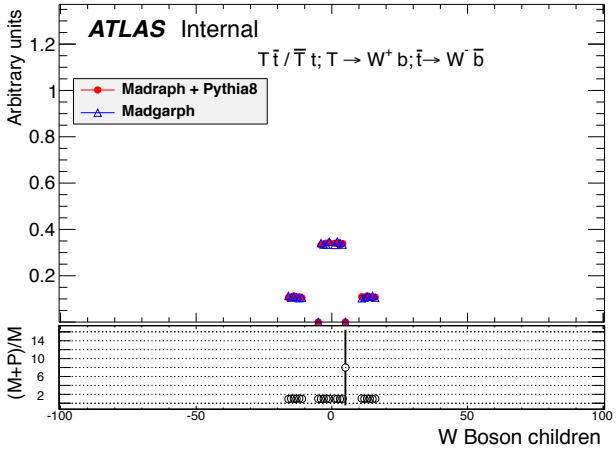

(d) W Boson children.

Figure 5.5: Second generation of particles according to g_{KK} decay chain from Figure 3.4: W Boson, with $m_{g_{KK}} = 1.0$ TeV, $m_T = 0.5$ TeV, $\tan\theta_3 = 0.3$ and $\Gamma(g_{KK})/m_{g_{KK}} = 10$ %.

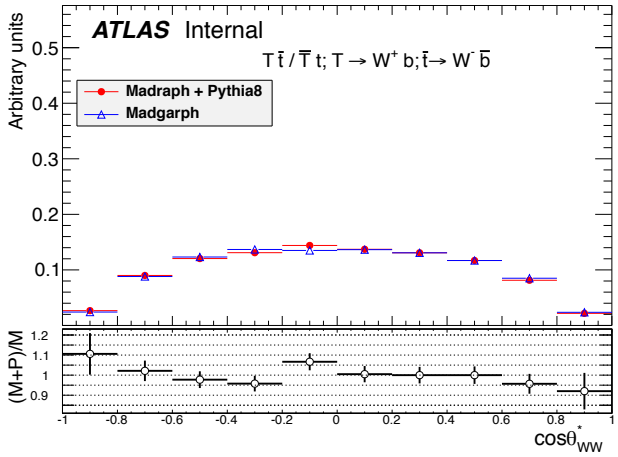

Figure 5.6: Centre-of-mass scattering angle $cos[\theta^*(WW)]$ of the WW system, with $m_{g_{KK}} = 1.0$ TeV, $m_T = 0.5$ TeV, $\tan\theta_3 = 0.3$ and $\Gamma(g_{KK})/m_{g_{KK}} = 10$ %.

The study of the second generation of particles (in g_{KK} decay chain), as seen in Figures 5.5, shows the production of two W Bosons (one from each top quark) with a symmetric center-of-mass scattering angle (Figure 5.6) in association with b quarks. These bosons decay into leptons and jets which are considered as third generation particles in g_{KK} decay chain. Their parameters are shown in Figures 5.7, 5.8 and 5.9. The small-R jets are ordered by transverse momentum as: $p_T(j_1) > p_T(j_2) > p_T(j_3)$.
Very small angular decay correlation effects in the dilepton system are seen in Figure 5.7d, which proves that there is no need to decay the gauge bosons in MADGRAPH. The differences in these plots are down to different BR($W \rightarrow$ leptons) in MDG5+PYTHIA8, hence, there are more events in MDG5 with very few jet. In general, the ratio between the two tested samples are around 1% encouraging the production of heavy gluon samples for tWb, tH and tZ channels with MADGRAPH only.

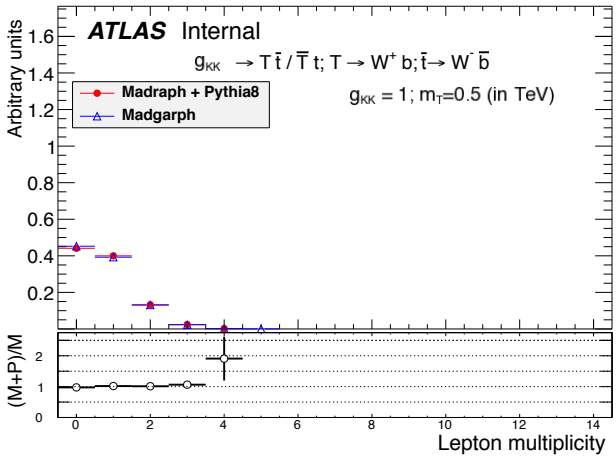

(a) Number of lepton.

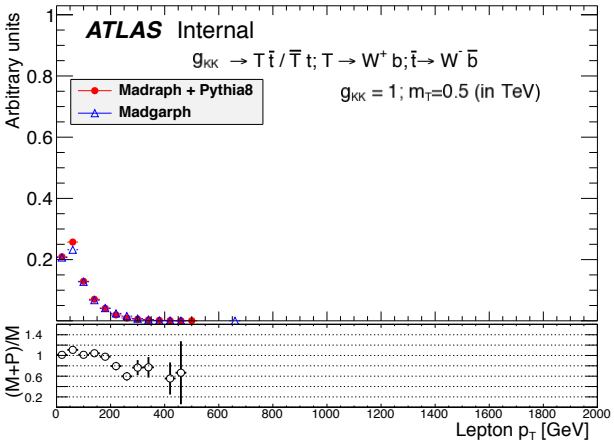

(b) Lepton $p_T(l)$ in GeV.

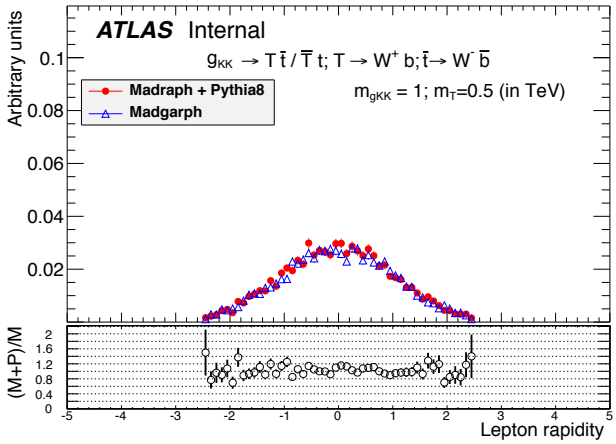

(c) Lepton rapidity.

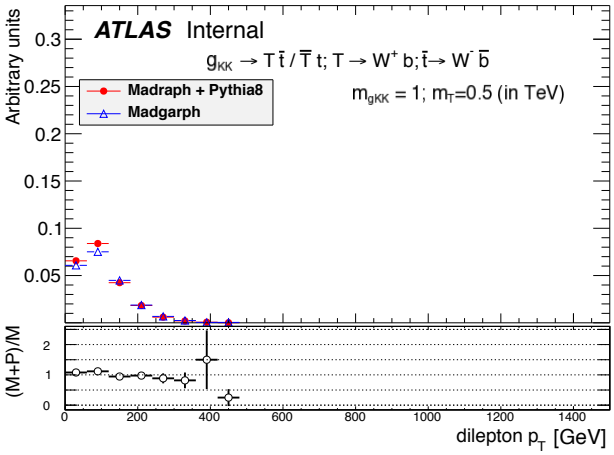

(d) Dilepton transverse momentum.

Figure 5.7: last generation of particles according to g_{KK} decay chain from Figure 3.4: lepton.

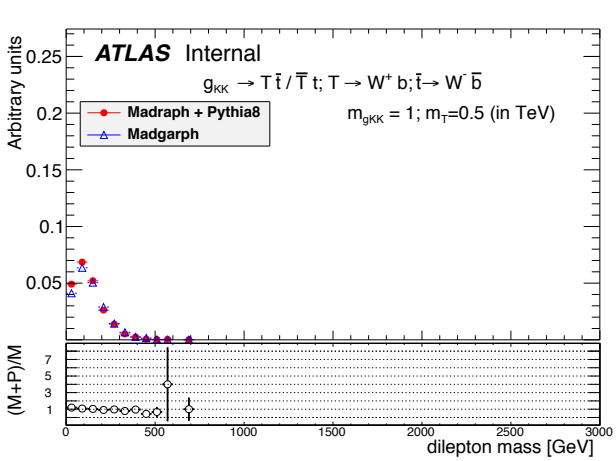

(a) Dilepton mass.

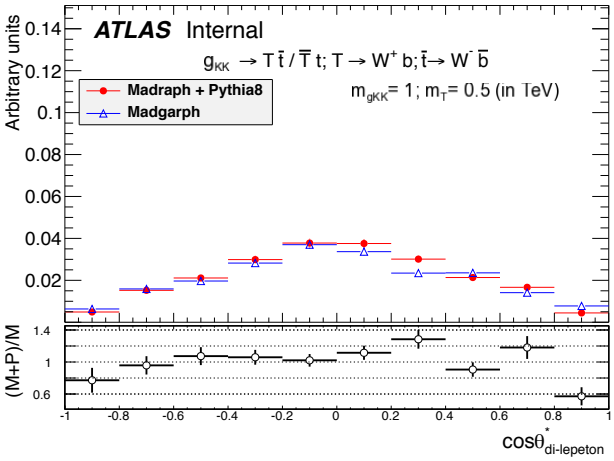

(b) Centre-of-mass scattering angle of the dilepton system.

Figure 5.8: last generation of particles according to g_{KK} decay chain from Figure 3.4: lepton.

A list of similar plots to the ones we saw for $T \to Wb$, could be found in appendices B and C for the channels $T \to tZ$ and $T \to tH$, respectively. These results show that, the samples produced via MADGRAPH only have a good sensitivity for the analyses presented in this thesis. We did not use Leading Order (LO) $\to$ Next to Leading Order (NLO) K-factor, because, there is no consensus in the literature as to the validity of various calculations for this model.

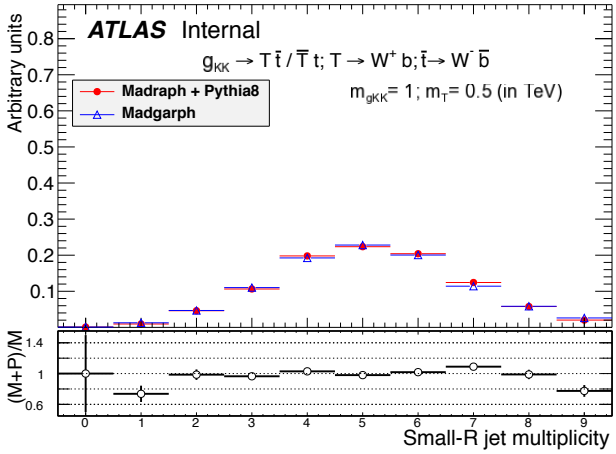

(a) Number of small-R jet.

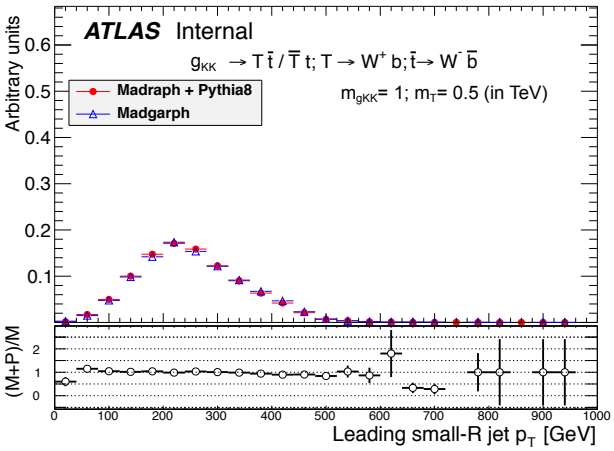

(b) Leading small-R jet $p_T(j_1)$ in GeV.

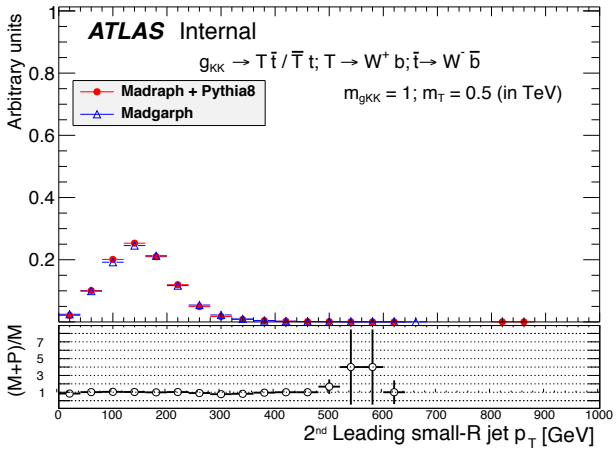

(c) Second leading small-R jet $p_T(j_2)$ in GeV.

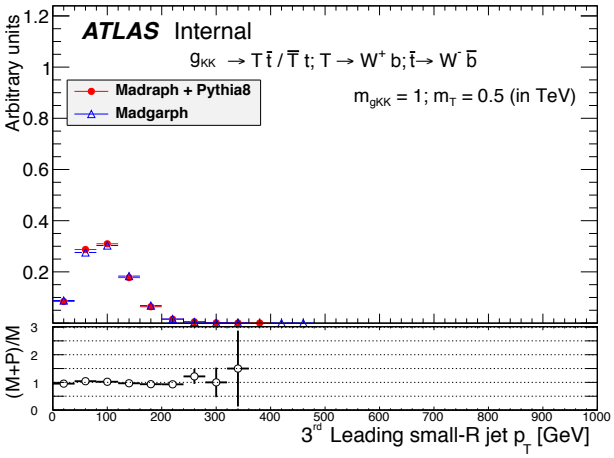

(d) Third leading small-R jet $p_T(j_3)$ in GeV.

Figure 5.9: Last generation of particles according to g_{KK} decay chain from Figure 3.4: small-R jets.

5.2.3 Kaluza-Klein gluon samples: $g_{KK} \to t\bar{t}$

We will compare the results from $g_{KK} \to Tt$ analysis with those obtained in previous studies [9]. Reference [52], searches for a g_{KK} that decays to pairs of light quarks (described in section 3.4 and shown in the right plot of Figure 3.3). According to the kinematic conditions considered in those searches, the branching ratio to SM top quarks is great than 90 %. The right-handed top quark is fully composite, and the values of parameters are as followed: $(\sin\varphi_L,\ \sin\varphi_{tR},\ \tan\theta_3) = (0.33,\ 1\ ,\ 0.2)$ leading to a width of 15.3% at all g_{KK} masses. Events ($g_{KK} \to t\bar{t}$) are generated with MADGRAPH [92] and then showered using PYTHIA 8 and the MSTW2008LO PDF set is used for the generation. Table 5.5 shows the g_{KK} cross sections.

Table 5.5: Cross sections for g_{KK} process $g_{KK} \to t\bar{t}$ for width of 15.3%.

$m_{g_{KK}}$ (GeV)	Cross Sections (pb)
400	112.2
500	81.9
600	45.0
700	25.2
800	14.6
900	8.81
1000	5.47
1150	2.82
1300	1.52
1600	0.500
1800	0.255
2000	0.137
2250	0.0670
2500	0.0351
2750	0.0196
3000	0.0120

5.3 Event selection

The required event selection used in these analyses, follows four steps: trigger selection, lepton selection, jet selection and missing transverse momentum requirements.

Triggers have been used to select events which contain at least one electron with $p_T > 24$ GeV or $p_T > 60$ GeV, or, at least one muon with $p_T > 24$ GeV or $p_T > 36$ GeV. Then, it has been required that at least four associated tracks with $p_T > 400$ MeV are used to reconstruct the position of the primary vertex. This ensures good quality event reconstruction and helps to reduce the effects from multiple p-p interactions (pileup).

The lepton selection consists of removing events that do not have exactly one electron or exactly one muon. The chosen lepton must match the appropriate trigger in the previous step. To pass lepton-plus-jets selection, events are required to have at least one *selected jet* [1]. The small-R jets, the selected jet and the large-R jets should satisfy the quality and kinematic criteria listed in Table 5.6. A summary of lepton reconstruction from the chapter 4 is presented in Table 5.7.

The missing transverse momentum criteria selection is used to reject backgrounds from hadronic decay of the $t\bar{T}$ and QCD multi-jets events. These events do not have any neutrino (from on-shell W or Z boson decay) in the final state. Their suppression is achieved by a requirement on E_T^{miss} as well as on the sum of the transverse mass of the selected lepton (m_T^W) and E_T^{miss}. For both electron and muon selections, the requirements are $E_T^{\text{miss}} > 20$ GeV or $E_T^{\text{miss}} + m_T^W > 60$ GeV, where m_T^W is the selected lepton transverse mass [2]. Further suppression of the background, not including jets containing a b-hadron, is achieved by requiring at least one of the small-R jets to be b-tagged jet. Finally we reject the events which passed all these selections, if they do not contain at least four small-R jets or at least one large-R jet. For events with a least a large-R jets, a 300 GeV transverse momentum threshold trigger has been used. Close to this threshold, Figures 5.20 show that number of events in the channel with small-R jets decreases significantly while the channel with large-R jets becomes relevant. Table 5.7 summarises the event selection requirements.

[1] The highest p_T and closest small-R jet to the selected lepton is called the *selected jet* and denoted as j_{sel}

[2] The transverse mass is defined as follows: $m_T^W = \sqrt{2p_T^l \, E_T^{\text{miss}} \, (1 - \cos\Delta\beta)}$. Where p_T^l is the lepton transverse momentum, E_T^{miss} is the missing transverse momentum and $\Delta\beta$ is the azimuthal angle separation between p_T^l and E_T^{miss}.

Table 5.6: Summary of jet selection and reconstruction requirements for g_{KK} analyses in both electron and muon channel, and in scenario S1, S2 and S3 from Figures 5.10 to 5.12.

Small-R jet Selection	Requirements
Algorithm	anti-k_t FAST-JET
Radius parameter	R=0.4
Cluster recombinaison	E-scheme
Pseudo-rapidity	$\|\eta\| < 2.5$
Transverse momentum	$p_T(j) > 25$ GeV
Jet Vertex Fraction	|JVF| > 0.5
Jet Overlap Removal	See section 4.3.7
isBadLooseMinus	$E(j) > 0$ && $p_T > 20$ GeV &&$\|\eta\| < 2.5$
b-jet	MV1 > 0.7892
Large-R jet Selection	**Requirements**
Algorithm	anti-k_t FAST-JET
Radius parameter	$R = 1.0$
Cluster recombinaison	E-scheme
Jet trimming parameters	$f_{\text{cut}} = 0.05$ and $R_{\text{sub jets}} = 0.3$
Distance from j_{sel}	$\Delta R(Lj, j_{\text{sel}}) > 1.5$
Distance from the selected lepton	$\Delta\phi(Lj, l) > 2.3$
Loose	$\|\eta\| < 1.5$, $p_T(Lj) > 200$ GeV
Tight	$\|\eta\| < 2.5$, $p_T(Lj) > 300$ GeV, $M(Lj) > 60$ GeV

Table 5.7: Summary of event selection and reconstruction requirements for g_{KK} analyses in both electron and muon channel, and in scenario S1, S2 and S3 from Figures 5.10 to 5.12.

Selection	Requirements
Lepton	Exactly one electron or one muon
Electron Triggers	EF_e24vhi_medium1 or EF_e60_medium1
Muon Trigger	EF_mu24i_tight or EF_mu36i_tight
Jet cleaning	isBadLooseMinus
Missing transverse momentum	$E_T^{\text{miss}} > 20$ GeV or $E_T^{\text{miss}} + m_T^W > 60$ GeV
Number of selected jet	$N(j_{\text{sel}}) >= 1$
Number of jets	$N(j) > 3$ or $N(Lj) >= 1$
Number of b-tagged jets	$N(bj) >= 1$
Electron Selection	**Requirements**
loose track isolation	$p_T^{0.2}/E_T < 0.1$
clusters pseudo-rapidity	$\lvert\eta_{\text{cl}}\rvert < 2.47$ with exclusion of $1.37 < \lvert\eta_{\text{cl}}\rvert < 1.52$
electron energy transverse	$E_T > 25$ GeV
identification criteria	Tight++
longitudinal impact parameter	$z_0 < 2$ mm, $z_0 \sin(\theta_{\text{track}}) < 10$ mm
mini isolation	$MI_{10}^e < 0.05$
transverse impact parameter	$d_0 <$ 10 mm
Muon Selection	**Requirements**
Type	combined
Pseudo-rapidity	$\lvert\eta\rvert < 2.5$
Transverse momentum	$p_T(\mu) > 25$ GeV
Track quality	MCP ID
Longitudinal impact parameter	$z_0 < 2$ mm
Significance of the transversal impact parameter	$d_0/\sigma_{d_0} < 3$
Mini isolation	$MI_{10}^e < 0.05$

5.4 Event Reconstruction

In this section, reconstructed invariant mass of the heavy gluon ($m_{g_{KK}}$) is developed as a tool for signal discrimination. This invariant mass of the g_{KK} events is computed using the invariant mass of the four-vectors of the reconstructed leptonic SM top quark and the VLQ top (considered to be leptonic and hadronic, respectively).

The invariant mass of the SM top quark is computed using the four-vector of the reconstructed neutrino, the charged lepton and the selected jet. Then reconstructed small-R jets far from the lepton (e.g. $\Delta R(\text{Lepton , Small-}R\text{jet}) > 1.5$) referred to as SJFarLep, and reconstructed large-R jets to compute VLQ top mass (m_T).

Considering five decay channels for VLQ top, one can reconstruct m_T for three scenarios [3]:

- S1: three SJFarLep which for $T \to Wb$ and can be compared to the invariant mass of the top-quark pairs, $m_{t\bar{t}}$ in the resolved selection scenario [65].
- S2: five SJFarLep for $T \to tH$ and $T \to tZ$. Where $H/Z \to 2$ SJFarLep and $t \to 3$ SJFarLep.
- S3: two SJFarLep in association with a LargeJet for $T \to Wb$ which can be compared to the invariant mass of the top-quark pairs, $m_{t\bar{t}}$ after the boosted selection [65].

Figures 5.10, 5.11 and 5.12 show the reconstructed g_{KK}. The left side of each figure shows, in purple, the leptonic SM top quark produced in association with the VLQ top, while the right side of the figures show, in green (and blue), the other particles produced according to each scenario from S1 to S3.

We used six samples of heavy gluon (which validation have been discussed in section 5.2.2), and two other validated samples as SM $t\bar{t}$ (POWHEG+PYTHIA) and g_{KK} samples. The reconstructed spectra for g_{KK} with masses of 1.0 and 2.0 TeV, and, $t\bar{t}$ are shown in figure 5.13, figures 5.14 to 5.15, figures 5.16 to 5.17 according to S1, S2 and S3 respectively. The effectiveness of the method is then measured using reconstructible Monte Carlo Tt events for which all the decays of the top quarks are in the acceptance of the detector and then can be matched to reconstructed objects. The quarks from the VLQ top decay are required to be matched to truth jets (with $p_T > 4$ GeV and $|\eta| < 5$) and those truth jets are also required to be matched to reconstructed jets. At each step, the matching is performed using a cone of radius $\Delta R = 0.4$, and in case of multiple possible matching objects the closest one is chosen. For the topologies with large-R jets, the matching of more than one quark to a reconstructed (or truth) jet is

[3] One additional scenario, S4: two LargeJets for the cases of boosted H and boosted Z, has been considered. The VLQ top mass is so large that it decays instantaneously into light particles mostly close to each other because of their high momentum. However, due to rough cuts applied to the large-R jet, we don't get enough events which contain more than two large-R jets.

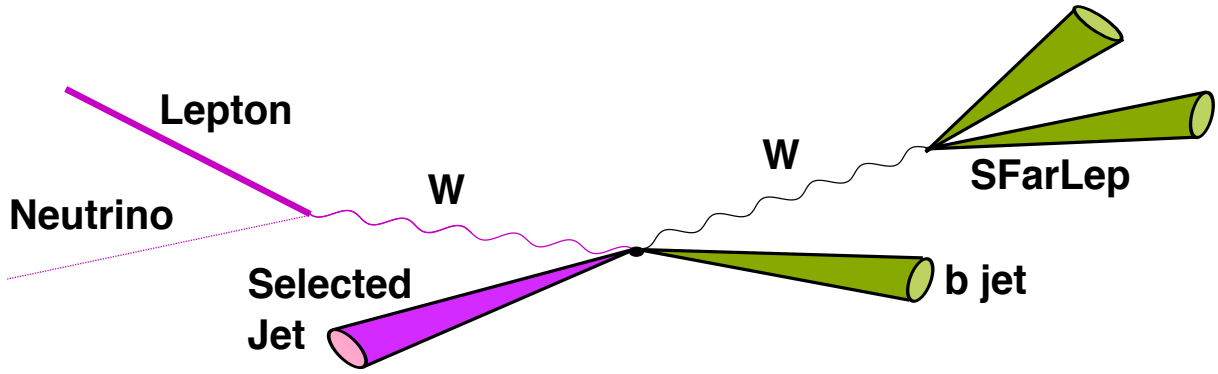

Figure 5.10: g_{KK} reconstructed from a leptonic SM top quark, in purple, (Lepton+Neutrino+Selected Jet), and a VLQ top quark decaying into three SJFarLep, in green, according to S1.

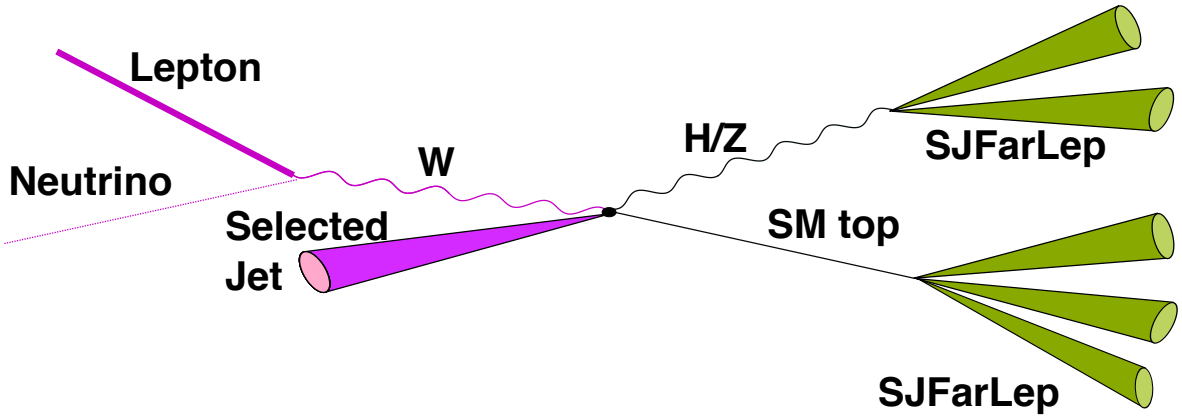

Figure 5.11: g_{KK} reconstructed from a leptonic SM top quark, in purple, (Lepton+Neutrino+Selected Jet) and a VLQ top quark decaying into five SJFarLep, in green, according to S2.

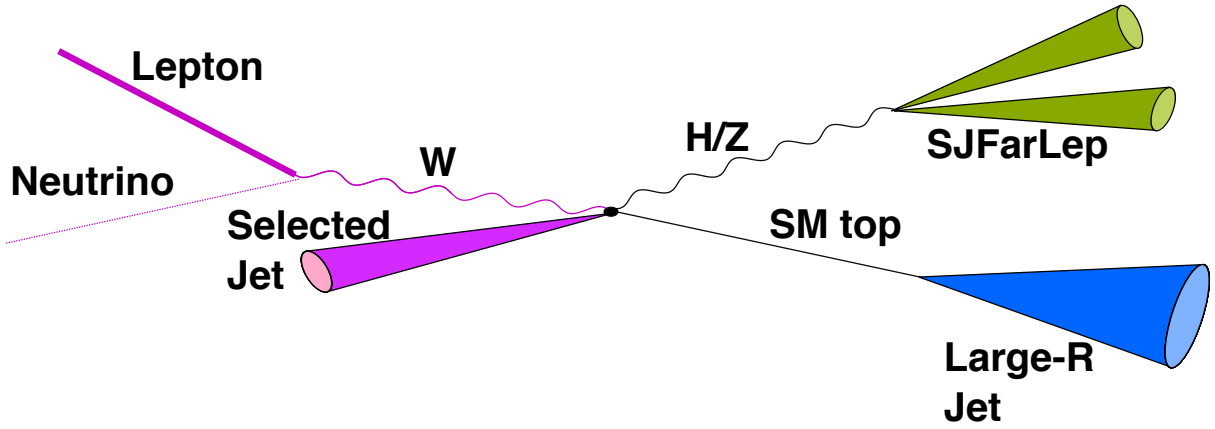

Figure 5.12: g_{KK} reconstructed from a leptonic SM top quark, in purple, (Lepton+Neutrino+Selected Jet) and a VLQ top quark decaying into one LargeJet, in blue and two SJFarLep, in green, according to S3.

allowed. The lepton (from the SM leptonic top) must match the selected reconstructed lepton, using a cone of radius $\Delta R = 0.4$. The neutrino and the E_T^{miss} are expected to point in the same direction so pass the selection $\Delta\Phi(\nu, E_T^{\text{miss}}) < 1$ rad.

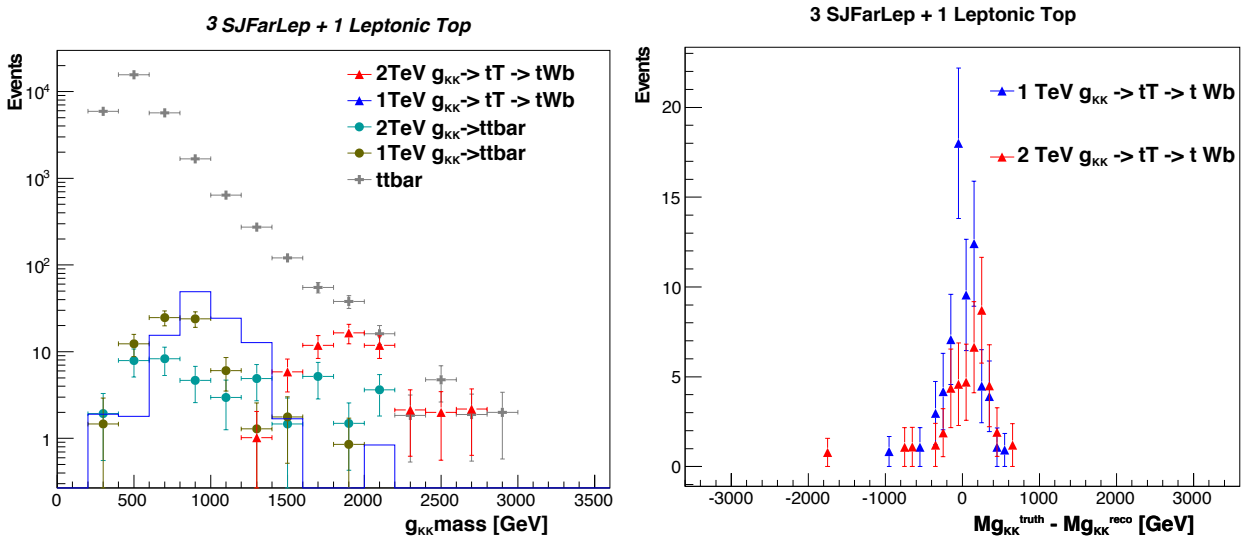

(a) Reconstructed g_{KK} mass.

(b) Reconstructed $m_{g_{KK}}$ resolution with respect to generated $m_{g_{KK}}^{\text{truth}}$.

Figure 5.13: Five samples are used in these figures: two $g_{KK} \to Tt$ samples with ($m_{g_{KK}}$, m_T) of (2.0 , 1.4) and (1.0 , 0.6) TeV, in red and blue line, respectively. Two $g_{KK} \to t\bar{t}$ samples with $m_{g_{KK}}$ of 1 and 2 TeV in khaki and green line, respectively. And finally, $t\bar{t}$ sample as the dominant background to g_{KK} signals. Left side: Reconstructed g_{KK} invariant mass using the S1 scenario. Right side: Reconstruction mass resolution for $g_{KK} \to Tt$ with respect to generated truth mass using the S1 scenario.

Figure 5.13 shows that for $T \to Wb$ channel (scenario S1), we can reconstruct signal peaks corresponding to $m_{g_{KK}}$=1.0 (e.g m_T= 0.6 TeV) and 2.0 TeV (e.g m_T= 1.4 TeV). However, g_{KK} mass is not well reconstructed and SM $t\bar{t}$ mass ($m_{t\bar{t}}^{SM}$) is shifted to higher mass. Furthermore, figures 5.14 to 5.17 related to scenarios S2 and S3, show that for all three channels $T \to Wb$, $T \to tH$ and $T \to tZ$ signal peaks at both $m_{g_{KK}}$=1.0 and 2.0 TeV are well reconstructed.

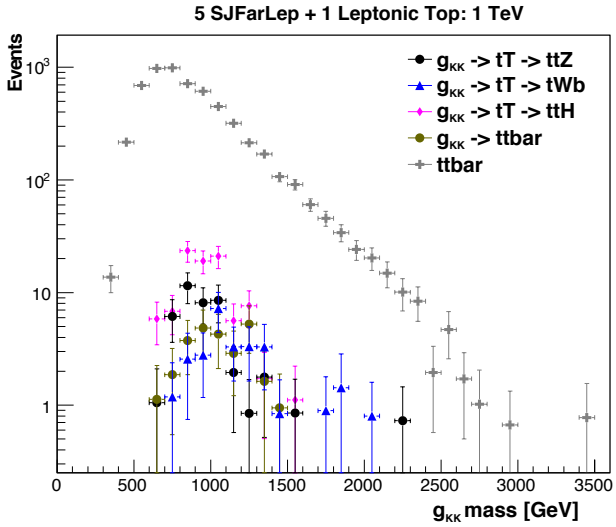

(a) Reconstructed $m_{g_{KK}} = 1.0$ TeV with $m_T = 0.6$ TeV.

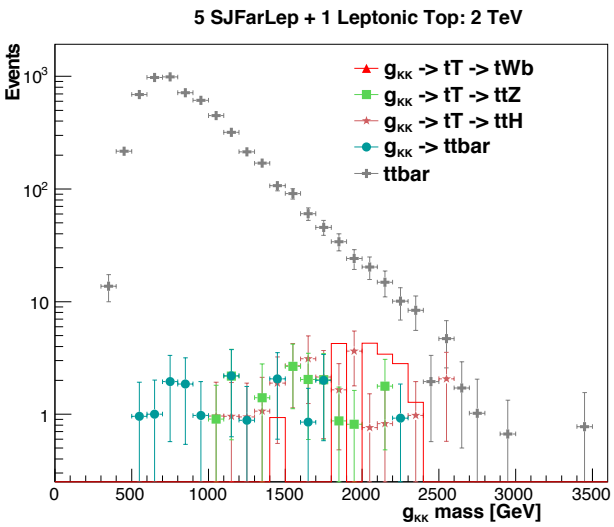

(b) Reconstructed $m_{g_{KK}} = 2.0$ TeV with $m_T = 1.4$ TeV.

Figure 5.14: Reconstructed g_{KK} invariant mass using the S2 scenario and reconstructed $m_{t\bar{t}}^{SM}$ (left side in grey).

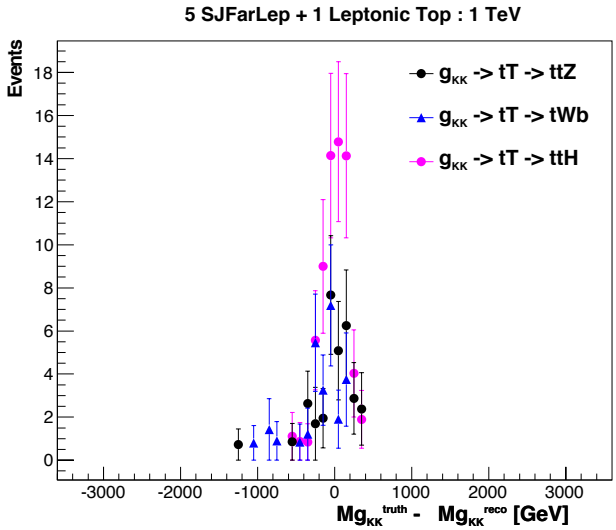

(a) Reconstructed $m_{g_{KK}}$ resolution with respect to generated $m_{g_{KK}}^{\text{truth}} = 1.0$ TeV with $m_T = 0.6$ TeV.

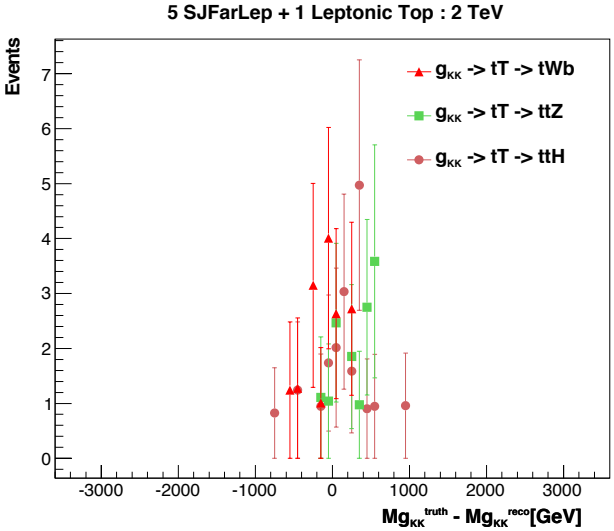

(b) Reconstructed $m_{g_{KK}}$ resolution with respect to generated $m_{g_{KK}}^{\text{truth}} = 2.0$ TeV with $m_T = 1.4$ TeV.

Figure 5.15: Reconstructed $m_{g_{KK}}$ resolution with respect to generated $m_{g_{KK}}^{\text{truth}}$ using the S2 scenario.

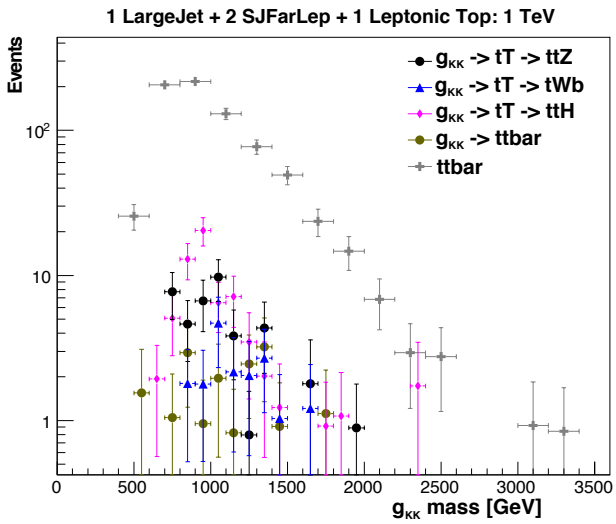

(a) Reconstructed $m_{g_{KK}} = 1.0$ TeV with $m_T = 0.6$ TeV

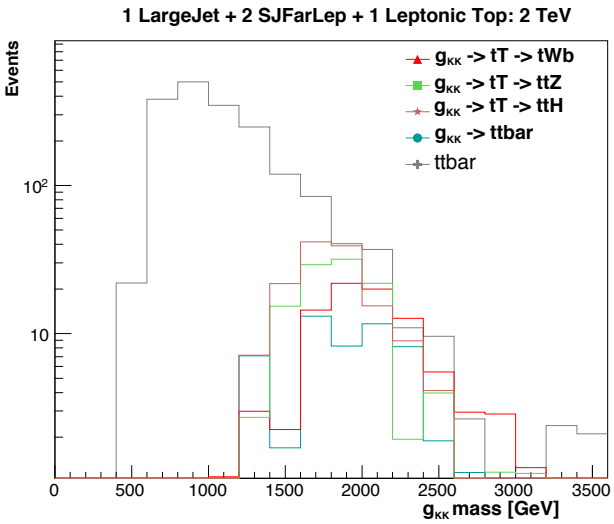

(b) Reconstructed $m_{g_{KK}} = 2.0$ TeV with $m_T = 1.4$ TeV.

Figure 5.16: Reconstructed g_{KK} invariant mass using the S3 scenario and reconstructed $m_{t\bar{t}}^{SM}$ (left side in grey).

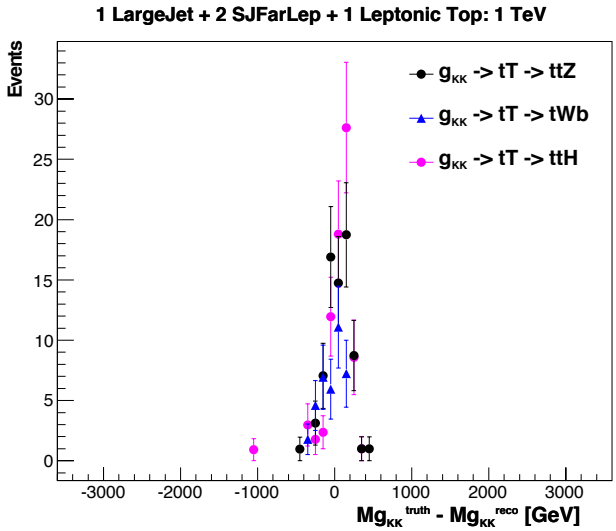

(a) Reconstructed $m_{g_{KK}}$ resolution with respect to generated $m_{g_{KK}}^{\text{truth}} = 1.0$ TeV with $m_T = 0.6$ TeV.

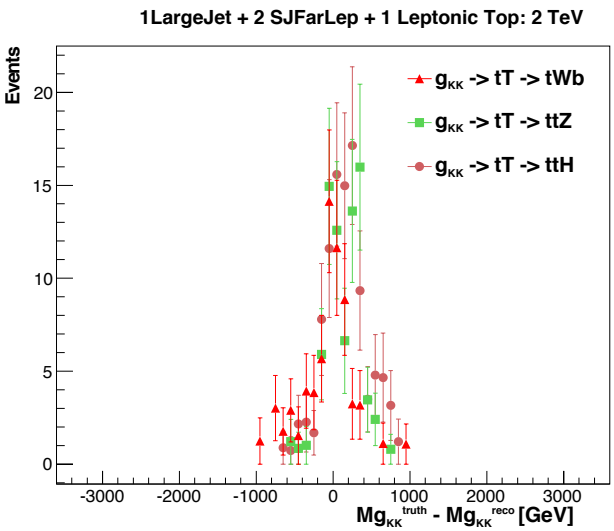

(b) Reconstructed $m_{g_{KK}}$ resolution with respect to generated $m_{g_{KK}}^{\text{truth}} = 2.0$ TeV with $m_T = 1.4$ TeV.

Figure 5.17: Reconstructed $m_{g_{KK}}$ resolution with respect to generated $m_{g_{KK}}^{\text{truth}}$ using the S3 scenario.

5.5 Background Estimation

As we consider the event selection, the g_{KK} signal is defined in terms of its final state objects. Therefore, the signal contains one lepton and a neutrino as a result of the leptonic W-boson decay, two b-quarks from the top decays and two up to five quarks from the other boson decay. If the lepton is a tauon and it decays hadronically, then it will be considered as part of background. Otherwise, the leptonic tauon is taken into consideration when it decays to an electron or a muon. From the detector perspective, a lepton, missing transverse momentum (as the undetected neutrino) and at least four jets are measured. As the final state contains either an electron or a muon, the signal is split into the electron channel or muon channel.

Many background events can be selected as they have a similar final state configurations as the g_{KK} signal: the final state particles are the same, or the misidentification of an object leads to tag background as the signal. The selection procedure helps to reject most of the background.
The remaining background in the data is then estimated after the selection and subtracted from data.

5.5.1 SM top quarks pair production background estimation

The main background to g_{KK} production is SM $t\bar{t}$ production because the final state particles are the same specially if one W boson (from one SM top quark) decays leptonically and the other W Boson (from the second SM top quark) decays hadronically.

Standard Model $t\bar{t}$ production was simulated using the POWHEG-BOX [93–96] generator r2330.3 interfaced with PYTHIA V6.427 [97] with the PERUGIA 2011C [98] tune and the CT10 [99] NLO Parton Distribution Functions (PDFs) set for the matrix element calculation. In the MC generation of POWHEG-BOX events, a parameter, called hdamp, has been added to the configuration to control the high p_T radiation. Its value was set to the top quark mass (set to $m_{t\bar{t}} = 172.5$ GeV) in order to achieve good agreement with Data. The production cross section was normalized to $\sigma_{t\bar{t}} = 167^{+17}_{-18}$ pb.

5.5.2 W+jets background estimation

After SM top quarks pair production background, the most significant background process is the production of W Bosons in association with jets (W+jets). These background could be misidentified as the signal because the W Boson could decay leptonically with initiale state radiation of jets.

Samples of W+jets events were generated using the ALPGEN generator [100] interfaced with PYTHIA V6.426, including up to five extra partons in the matrix element. Configurations with additional heavy

quarks (W+c+jets, W+$\bar{c}c$+jets, W+$b\bar{b}$+jets) were included, with the masses of heavy quarks taken into account. The CTEQ6L1 Parton Distribution Function (PDF) set and the PERUGIA 2011C tune were used. The samples were normalized using data as described in Section 5.6. Additional samples were generated with different choice of ALPGEN matching parameters in order to estimate modelling uncertainties on the production of W+jets events.

5.5.3 Single top background estimation

Production of single top quarks can yield events that pass the analysis event selection. The POWHEG-BOX generator interfaced with PYTHIA V6.426 was used to estimate the quark-antiquark annihilation, called s-channel (W Boson virtually is time-like), and top quark production in association with a W Boson, called tW channel [100–102], with the same configuration as for the $t\bar{t}$ samples. The top quark production via a W space-like boson exchange, called t-channel, was generated, in a four-flavour scheme, by using POWHEG-BOX with the CT10 NLO four-flavour PDF set. Overlap between the tW sample and $t\bar{t}$ samples was handled using the diagram removal scheme [103].

5.5.4 Minor background estimation

The minor background process which have prompt isolated leptons and multiple jets as final state particles are diboson, Z boson in association with jets (Z+jets) and $t\bar{t}$ in association with a heavy gauge boson ($t\bar{t}+V$).

The generator ALPGEN interfaced with PYTHIA V6.426 was used to simulate Z+jets events, in the same configuration used for the W+jets samples described in section 5.5.2. Then the samples were normalized to the inclusive Z boson production cross-section calculated at Next to Next to Leading Order (NNLO) in QCD using Fully Exclusive W and Z production (FEWZ) code [104].

Diboson production of ZZ, WW and WZ was modelled using the Sherpa [105–108] generator, with up to three extra partons in the matrix element and taking into account the mass of the b-quark and c-quark. The diboson samples were normalized to calculations at NLO in QCD performed using parton-level integrator MCFM [109].

The $t\bar{t}V$ events were simulated using MadGraph5 interfaced with PYTHIA V6.426 and normalized to NLO cross-section predictions [110].

5.6 Background processes estimated using data: QCD

Data from pp collisions are used to estimate two types of background from non-prompt lepton sources: W+jets events and multi-jet events.

Scale factors are determined from data then applied to correct the normalisation and flavour fractions of the W+jets background simulated by ALPGEN generator. More detail can be found in reference [65].

The multi-jet background (denoted as QCD), in events passing the selection criteria consists of events with a jet that is misreconstructed as a lepton or with non-prompt leptons that pass the identification criteria. The normalisation, reconstructed invariant mass shape, statistical and systematic uncertainties associated with the multi-jet background are estimated from data. The method used to determine fake leptons rate is very well described in [65].

5.7 Systematic uncertainties

There are two categories of systematic uncertainties: uncertainties that affect reconstructed objects listed in section 4.3 and uncertainties that affect the modelling of certain background or signal processes. We need to make sure that they are under control so we can have a correct experimental observation of g_{KK} mass resonance. Indeed, some of the uncertainties affect both the shape and the normalisation of the $m_{g_{KK}}$ spectra, while others affect the normalisation only.

5.7.1 Reconstructed objects Systematic uncertainties

The top uncertainty affecting reconstructed objects, especially large-R jets [85, 111], is the JES uncertainty. For jet objects, are also taken into account the Jet Mass Scale (JMS) and the kt splitting scales [85]. These uncertainties have been estimated to be below 11% on the overall background.

Two uncertainties on the JER and Jet Mass Resolution (JMR) are estimated for reconstructed large-R jets objects (below 6%).

Furthermore, for reconstructed small-R jets objects, the uncertainties are the JES, the jet reconstruction efficiency and the JER [74, 77]. The JES uncertainty is dominant, about 5%, in the case of scenario S1 and S2, where large-R jets are not considered in the invariant mass of g_{KK} calculations. The effect of uncertainties associated with the jet vertex fraction is also considered ($\pm$ 4%).

For reconstructed b-jet objects, a b-tagging uncertainty is modelled by varying the scale factors on the efficiency and rejection rates in simulation [112, 113]. To this, an additional b-tagging uncertainty

is applied for high-momentum jets (p_T>300 GeV) as a correction of the track reconstruction in high-p_T environments. The resulting b-tagging contribution to the overall systematic uncertainty is about $\pm$ 2%

For reconstructed lepton objects, $z \to ee$ and $z \to \mu\mu$ events are used to estimate the uncertainties on the isolation efficiency, the single lepton trigger and the reconstruction efficiency. Then, the difference between Z and $t\bar{t}$ events is determined during high-jet-multiplicity $z \to ll$ events study and extra uncertainties on the isolation efficiency are estimated. These uncertainties are relatively small, dominated by the lepton identification in the e+jets channel ($\pm$ 3%) and the muon triggering efficiency in the μ+jets channel ($\pm$ 4%).

Uncertainties on the E_T^{miss} reconstruction, as well as on the energy scale and resolution of the leptons, are also considered, and generally have a smaller impact on the yield and the search sensitivity than the uncertainties mentioned above. These systematics are below$\pm$ 1%.

5.7.2 Background and Data Systematic uncertainties

First of all, the dominant uncertainty is on the normalisation of W+jets background determined from data and MC. For each experimental source of systematic uncertainty, data samples are used to determine the W+jets uncertainty. In addition, the simulated samples generated with varied Alpgen matching parameters are used to evaluate the systematic uncertainty on the prediction. The total normalisation uncertainty on the QCD described in 5.6 is about 16%.

Then comes, the uncertainty on the single top, Z+jets and diboson backgrounds normalisation are 9%, 45% and 38% respectively.
The single top samples were normalized to NNLO cross-sections [114–116]. The luminosity uncertainty in data measued by van der Meer scans, was found to be about 3% [12]. The latter uncertainty was used to normalise all signal and simulation samples, except QCD and W+jets backgrounds estimated from data.

For the $t\bar{t}$ background, uncertainty is estimated on the QCD initial- and final- state radiation (ISR/FSR) using MC samples produced using AcerMC v3.8 [117] plus Pythia v6.426 generators. The technique consists on the ISR/FSR parameters variations within appropriate ranges with a veto on additional central jet activity [118]. The QED ISR/FSR uncertainty is negligible. However, the uncertainty on the electroweak corrections to top quark pair production is modelled by changing the difference of each correction factor from unity by 10%.

Finally, on all MC samples, a set of PDFs uncertainty is estimated. The PDFs are obtained from global fits to data from deep-inelastic scattering. At the NLO and NNLO, the total uncertainty has been calculated from renormalisation and factorisation scale uncertainties, combined PDF and strong-coupling uncertainties and uncertainties associated with the value of the top quark mass. For the combined PDF

and strong-coupling uncertainties, the three sets of PDFs that have been used are MSTW2008 68% CL NNLO (MSTW200snlo68cl) [119, 120], CT10 NNLO [99, 121] and NNPDF2.3 NNLO [122]. More detail can be found at [123].
The effect on the total background yield is 3% after the selection. The size of the uncertainty grows with reconstructed mass, attaining values of 48% above 2.0 TeV.

5.8 Comparison of data and background expectations

5.8.1 Before statistical analysis

After all event selection criteria, from section 5.3, are applied more than 71×10^3 events pass the selection. These events contain at least four small-R jets or one large-R jet. Table 5.8 lists, for each scenario S1 to S3, the event yields from data, and, from expected background processes as well as the associated uncertainties (statistic and systematic). The Table shows that, a good agreement is observed between the data and the total expected background (referred to as Total bkg).

Figure 5.18 and 5.19 show the reconstructed mass of the hadronic VLQ top, and, semileptonic SM top quark candidates. The distribution of the transverse momentum of the leading large-R jet (corresponding to the largest mass) and the leading small-R jet (jet with the largest p_T) are shown in Figures 5.20. The distribution of the reconstructed mass and first kt splitting scale of the selected large-R jet are presented in Figures 5.21.

The g_{KK} invariant mass spectra in the electron and muon channels, are shown in Figures 5.22 and 5.23. The data generally agrees with the expected background, with, slight shape deviations seen especially in the high mass regions. These deviations are consistent with the uncertainties. Moreover, Figures 5.13 to 5.17 show that the g_{KK} invariant mass spectra for both $g_{KK} \to T\bar{t}+t\bar{T}$ and $g_{KK} \to t\bar{t}$ are very well reconstructed in each scenario.

Table 5.8: Data and expected background event yields, after the selections from section 5.3, for S1, S2 and S3 scenario shown in Figures 5.10, 5.11 and 5.12. The quadratic sum of all uncertainties on the expected background yields is also given: stat. syst. stand for statistic and systematic uncertainties, respectively.

Type	e+jets ± syst. ± stat.	μ+jets ± syst. ± stat.	Sum $e+\mu$ channels ± (syst.+stat.)
Reconstructed $m_{g_{KK}}$, in S1, with a leptonic top and three SJFarLep (Figure 5.10)			
$t\bar{t}$	29,516 ± 2,473 ± 51	28,106 ± 2,718 ± 50	57,622 ± 5,292
Single top	1,683 ± 175 ± 12	1,693 ± 390 ± 12	3,376 ± 590
W+jets	3,439 ± 429 ± 59	3,662 ± 653 ± 59	7,101 ± 1,200
Z+jets	599 ± 96 ± 13	239 ± 60 ± 8	838 ± 177
Di-boson	128 ± 29 ± 6	126 ± 50 ± 6	254 ± 91
$t\bar{t}$+Boson	192 ± 12 ± 1	178 ± 15 ± 1	370 ± 29
QCD e	205 ± 0 ± 4	–	205 ± 4
QCD μ	–	181 ± 0 ± 2	181 ± 2
Total bkg	35,762 ± 3,107 ± 80	34,186 ± 3,558 ± 79	69,948 ± 6,824
Data	34,057	31,227	65284
Reconstructed $m_{g_{KK}}$, in S2, with a leptonic top and five SJFarLep (Figure 5.11)			
$t\bar{t}$	7,847 ± 1,073 ± 26	8,117 ± 1,162 ± 27	15,965 ± 2,288
Single top	111 ± 20 ± 3	612 ± 147 ± 7	723 ± 178
W+jets	694 ± 151 ± 24	801 ± 268 ± 26	1495 ± 470
Z+jets	141 ± 33 ± 5	56 ± 32 ± 4	197 ± 74
Di-boson	2.94208 ± 2.71132 ± 0.77567	29 ± 22 ± 3	32 ± 28
$t\bar{t}$+Boson	76 ± 8 ± 1	76 ± 17 ± 1	152 ± 27
QCD e	46 ± 0 ± 2	–	46 ± 2
QCD μ	–	62 ± 0 ± 1	62 ± 1
Total bkg	8,918 ± 1,252 ± 36	9,753 ± 1,516 ± 38	18,672 ± 2,843
Data	8,277	8,378	16,655
Reconstructed $m_{g_{KK}}$, in S3, with a leptonic top, one large-R jet and two SJFarLep (Figure 5.12)			
$t\bar{t}$	1,483 ± 181 ± 11	1674 ± 205 ± 12	2,156 ± 409
Single top	14 ± 3 ± 1	13 ± 3 ± 1	26 ± 9
W+jets	192 ± 35 ± 14	252 ± 51 ± 16	445 ± 115
Z+jets	18 ± 9 ± 3	12 ± 5 ± 2	30 ± 19
Di-boson	1.62393 ± 1.14297 ± 0.71812	1.50983 ± 1.48599 ± 0.67177	3.13376 ± 4.01886
$t\bar{t}$+Boson	17 ± 2 ± 0	15 ± 2 ± 0	32 ± 4
QCD e	8 ± 0 ± 1	–	8 ± 1
QCD μ	–	1 ± 0 ± 0	1 ± 0
Total bkg	1,733 ± 202 ± 18	1,968 ± 237 ± 20	3,700 ± 476
Data	1,688	1,853	3,541

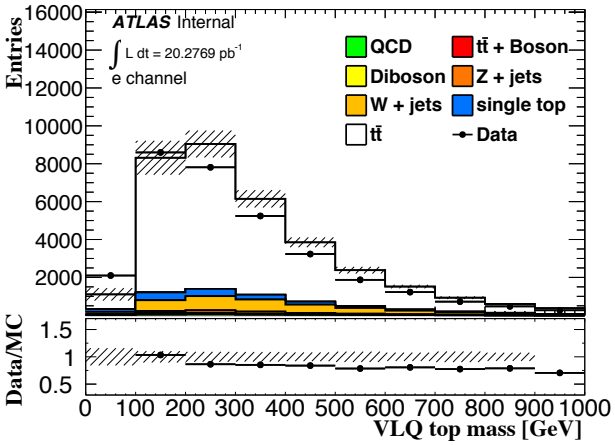

(a) S1 scenario, e+jets channel.

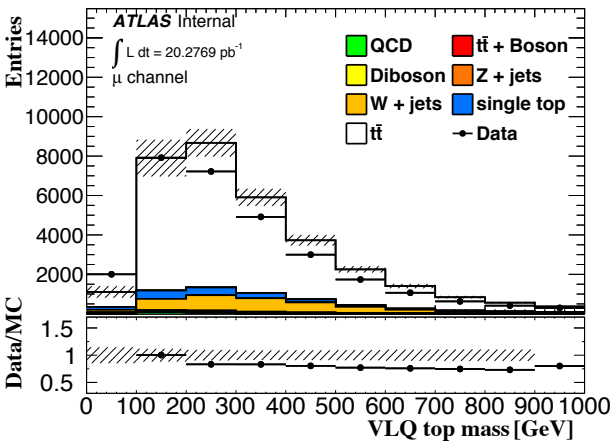

(b) S1 scenario, μ+jets channel.

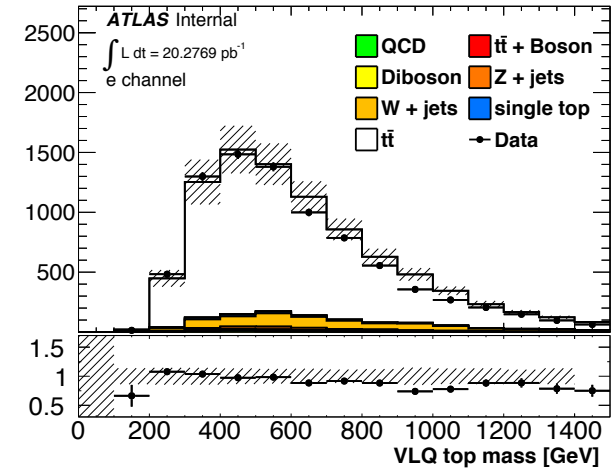

(c) S2 scenario, e+jets channel.

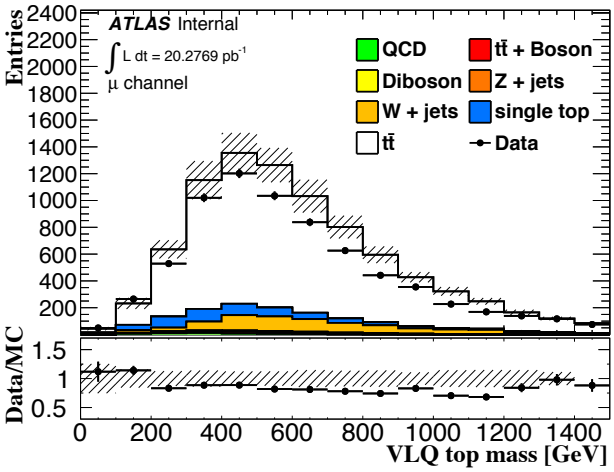

(d) S2 scenario, μ+jets channel.

Figure 5.18: Reconstructed mass of the hadronically decaying VLQ top candidate in scenario S1 and S2, in the electron and muon channels. The SM background components are shown as stacked histograms. The shaded areas indicate the total systematic uncertainties.

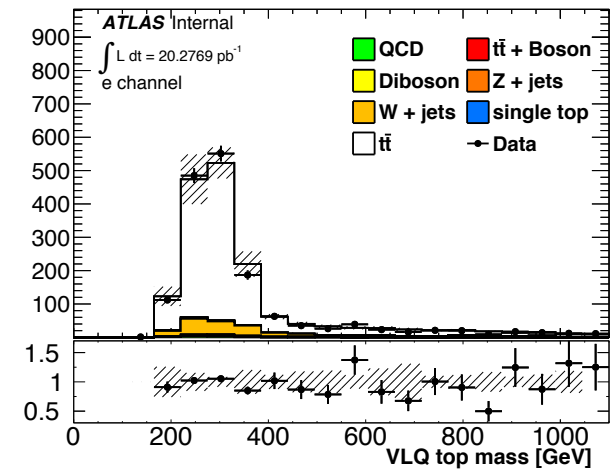

(a) S3 scenario, e+jets channel.

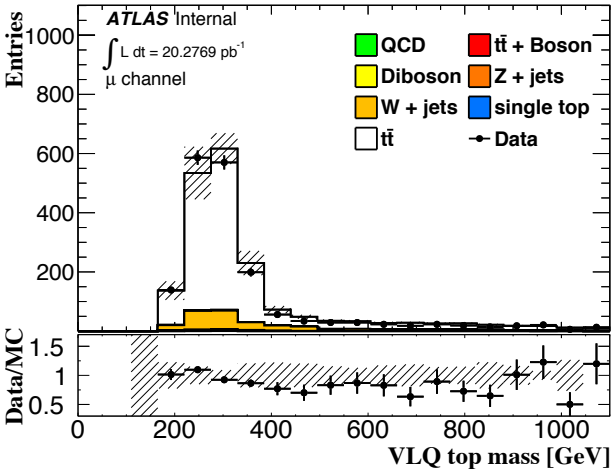

(b) S3 scenario, μ+jets channel.

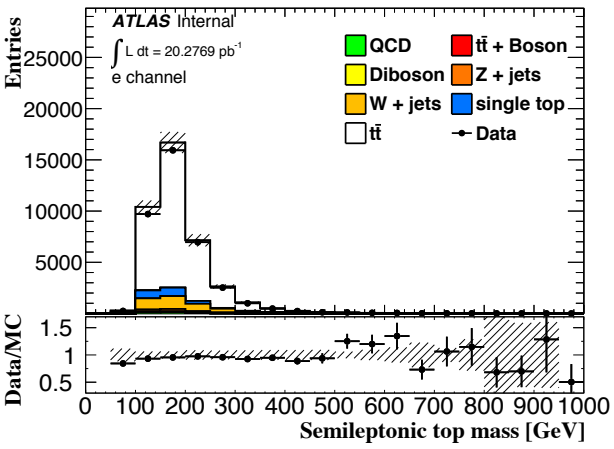

(c) e+jets channel.

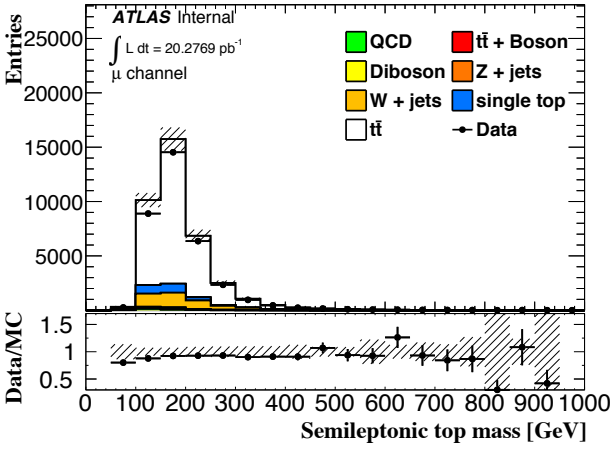

(d) μ+jets channel.

Figure 5.19: Reconstructed mass of the hadronically decaying VLQ top candidate in scenario S3 (at the top of the page), semileptonically decaying SM top quark candidate (at the bottom of the page), in the electron and muon channels. The SM background components are shown as stacked histograms. The shaded areas indicate the total systematic uncertainties.

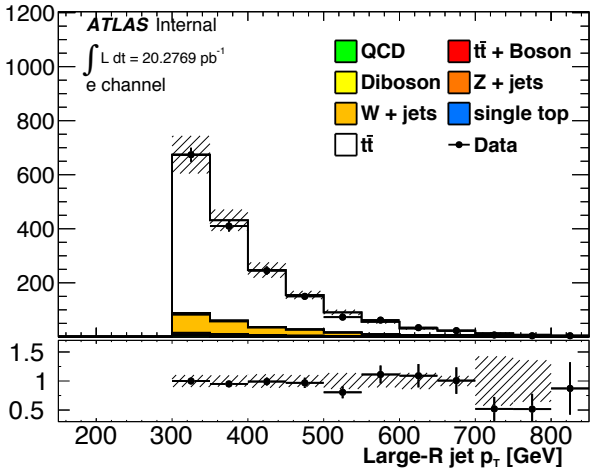

(a) e+jets channel.

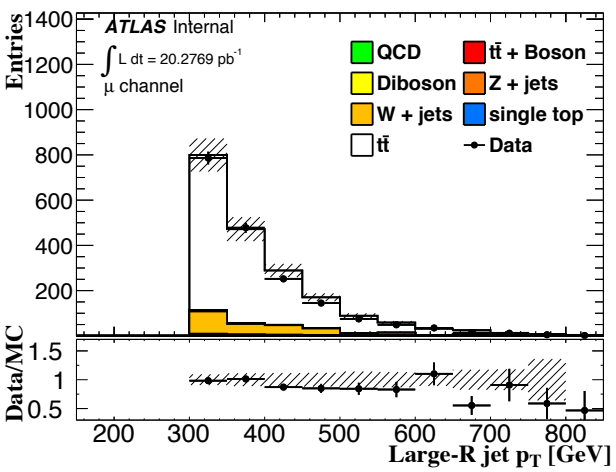

(b) μ+jets channel.

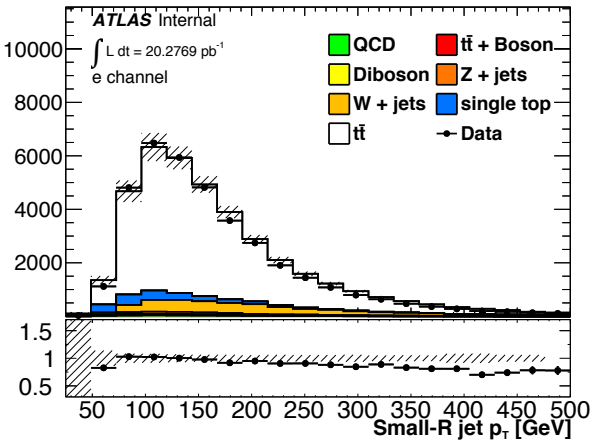

(c) e+jets channel.

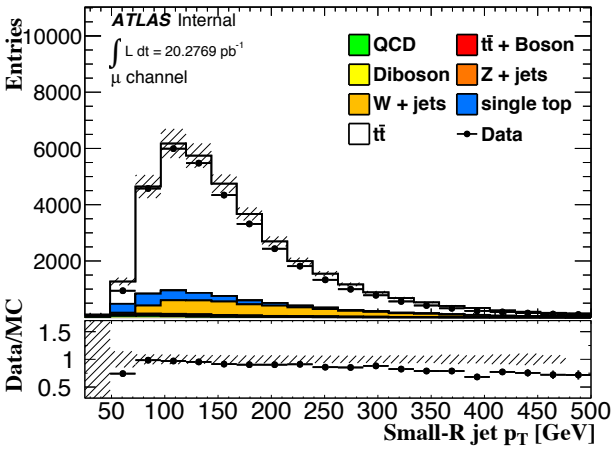

(d) μ+jets channel.

Figure 5.20: The transverse momentum of the leading large-R jet and the leading small-R jet. The SM background components are shown as stacked histograms. The shaded areas indicate the total systematic uncertainties.

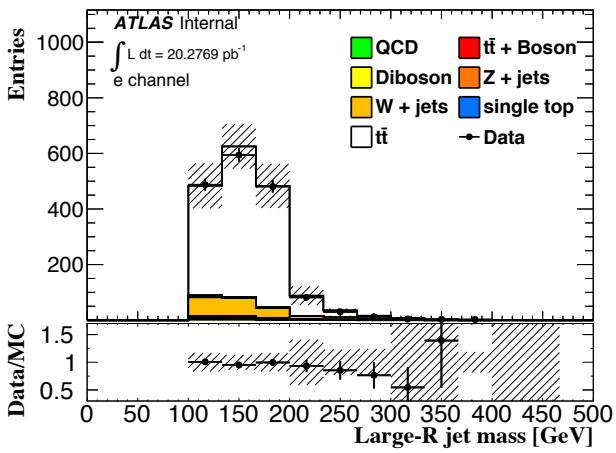

(a) e+jets channel.

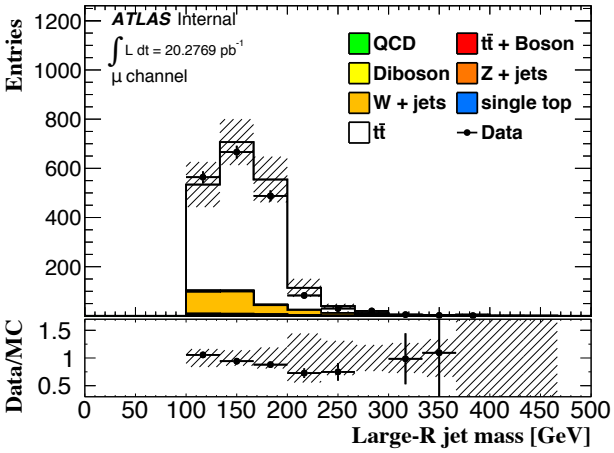

(b) μ+jets channel.

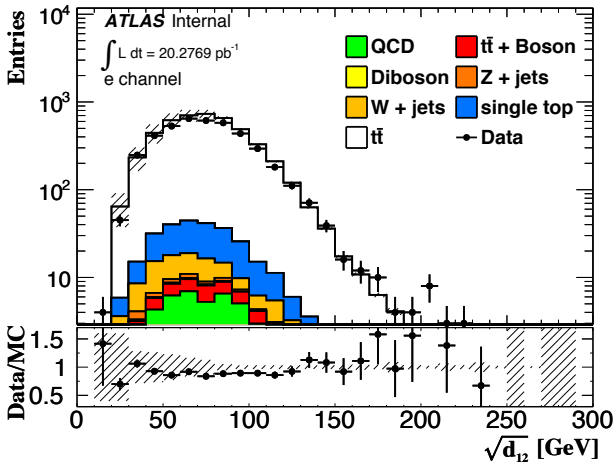

(c) e+jets channel.

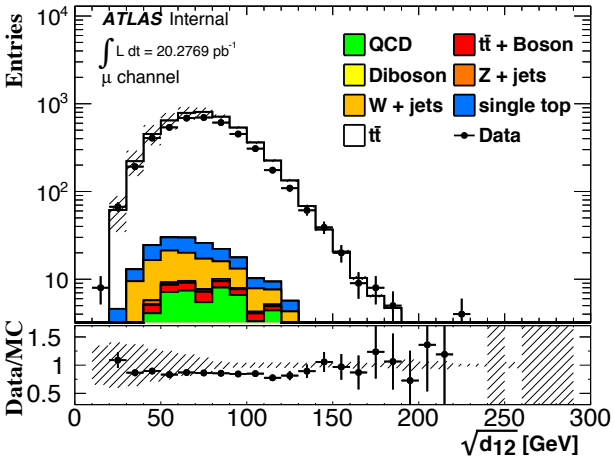

(d) μ+jets channel.

Figure 5.21: The Reconstructed large-R jet mass, and, the first kt splitting scale, $\sqrt{d_{12}}$, of the large-R jet for muon and electron channels. The SM background components are shown as stacked histograms. The shaded areas indicate the total systematic uncertainties.

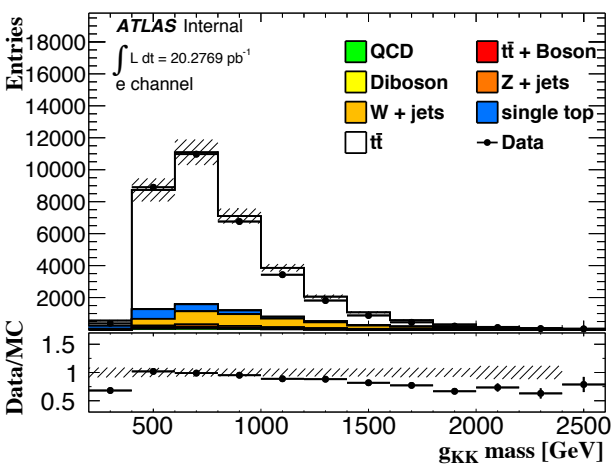

(a) Senario S1, e+jets channel.

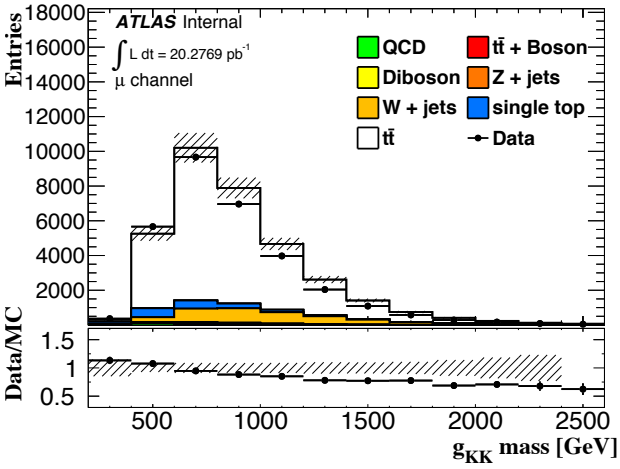

(b) Senario S1, μ+jets channel.

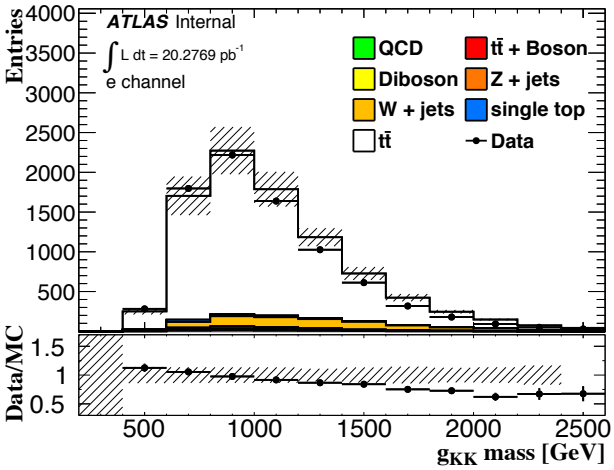

(c) Senario S2, e+jets channel.

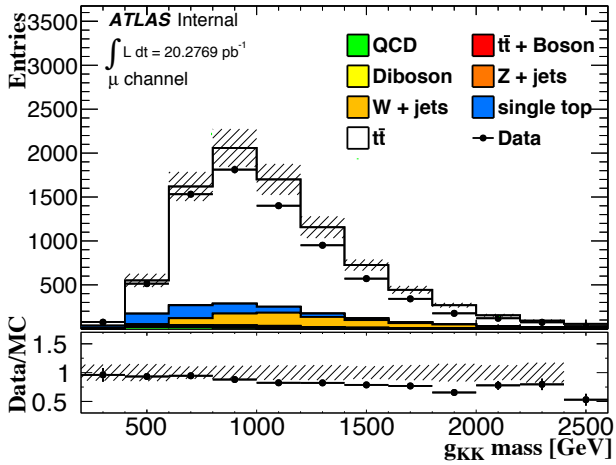

(d) Senario S2, μ+jets channel.

Figure 5.22: Reconstructed g_{KK} mass, before any nuisance parameter fit, in scenario S1 and S2, in the electron and muon channels. The SM background components are shown as stacked histograms. The shaded areas indicate the total systematic uncertainties.

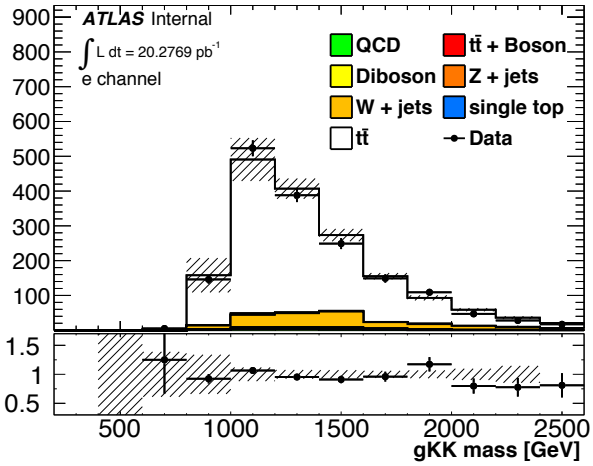

(a) Senario S3, e+jets channel.

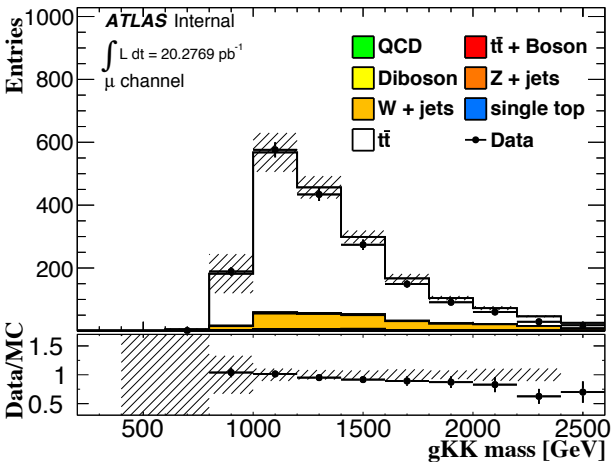

(b) Senario S3, μ+jets channel.

Figure 5.23: Reconstructed g_{KK} mass, before any nuisance parameter fit, in Senario S3, in the electron and muon channels. The SM background components are shown as stacked histograms. The shaded areas indicate the total systematic uncertainties.

5.8.2 Statistical analysis

A statistical model is used to compare data with theory for the distributions of the final discriminating variables in each of the analysis channels considered. For the analyses presented in this thesis, a package named HistFitter including three statistical tests is used. The three statistical tests are [124]:

1. hypothesis tests of signal models;
2. the construction of expected and observed confidence intervals on model parameters. For example, the 95% confidence level upper limit on the rate of a signal process;
3. the significance determination of a potentially observed event excess.

By default, Histfitter employs a Frequentist method or p-value, to perform hypothesis tests and uses the profile likelihood ratio $q_{\mu_{\text{sig}}}$ as test statistic. The CL method [125] is used to test the exclusion of new physics hypothesis [124].

The statistical model from HistFitter uses the likelihood function $L(\mu_{\text{sig}}, \theta)$. This function is the product of Poisson distributions of event and of additional distributions that implement the constraints on systematic uncertainties. The parameter μ_{sig} stands for the signal strength multiplicative factor to the theoretical signal production cross section. And, the parameter θ is a set of nuisance parameters that parametrize the impact of systematic uncertainties on the signal and background expectations.

To each systematic uncertainty is associated with a nuisance parameter that continuously interpolates between the variations and the nominal (of the expectations for signal and background) template. From this process, deviations from the nominal expectations are estimated and used as the best fit to the data. Therefore, the impact of systematic uncertainties on the signal is reduced. Likewise, both μ_{sig} and θ parameters are implemented in the likelihood function as Gaussian or log likelihood priors and rule on the total number of expected event in each bin. The profile log likelihood ratio for one hypothesized signal strength (μ_{sig}) is given by the test statistic [124]:

$$q_{\mu_{\text{sig}}} = -2 \log \left[\frac{L(\mu_{\text{sig}}, \hat{\hat{\theta}})}{L(\hat{\mu}_{\text{sig}}, \hat{\theta})} \right]. \tag{5.1}$$

where $\hat{\mu}_{\text{sig}}$ and $\hat{\theta}$ maximize the likelihood function, and $\hat{\hat{\theta}}$ maximize the likelihood for the specific fixed value of the μ_{sig}.

The first fit strategy, in HistFitter, is called background-only fit which consists of background prediction improvement. The purpose of the background-only hypothesis is to estimate the total background without making assumptions on any signal model. Therefore, only background samples are used, and, the dominant background processes are normalized to the observed event counts. Differences between normalized background, referred to as Asimov data, and the background prediction are checked relative to the smaller post-fit uncertainties in kinematic variables other than the ones used in the fit. To analyse the effect of systematics profiling, the pulls of post-fit nuisance parameters from background-only fit are examined in Figure 5.24. When Asimov data is used, the pulls are mostly centred at 0, due to absence of adjustment on background prediction. When real data is used in the fitting, the means of post-fit nuisance parameters will be further pulled away from 0 in order to fit MC to data. Due to the known $t\bar{t}$ mis-modelling issue, we have seen several nuisance parameters pulled away from 0 considerably, in order to fit the tension between data and MC.

Since, the presented analyses search for new physics phenomena (g_{KK} resonances), a second fit strategy called model-independent signal fit is used. This fit allows to set a model-independent upper limits on the number of events beyond the expected number of events. So for any signal model of interest, we can estimate the number of signal events predicted in a particular signal region and check if the model has been excluded by current measurements or not. Background and data samples are used for this fit. HistFitter provides the possibility to set an upper limit on the signal strength parameter μ_{sig}, given the observed data in the signal regions. To do so, the value of the signal strength needs to be evaluated for which the CL value falls below a certain level, usually 5% (for a 95% CL upper limit). In an initial scan, multiple hypothesis tests are executed using the asymptotic calculator [126] to evaluate the CL values for a wide range of signal strength values. A second scan follows in a smaller, refined interval, using the expected upper limit derived from the first scan.

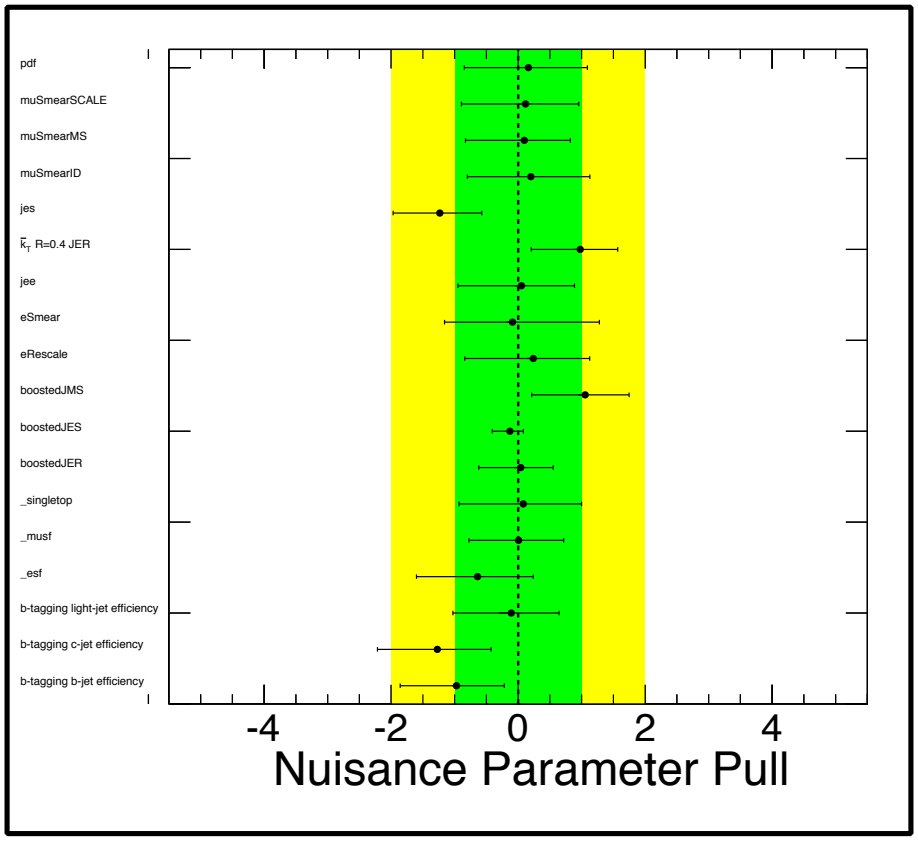

Figure 5.24: Pulls of nuisance parameters from background-only fit, using Asimov (e.g. the nominal background estimation) data for $g_{KK} \to t\bar{t}$ with a width of 15.3 % and a mass of $m_{g_{KK}} = 900$ GeV.

The obtained upper limit on the signal strength can, then, easily be converted into an upper limit on the excluded cross section of the signal model tested initially. These cross section upper limits are often displayed together with the limits obtained from the signal hypothesis test. We used same set of nuisance parameters that were used in the paper [1].

5.9 Results

After the reconstruction of the g_{KK} mass spectrum, the data and simulation distributions are compared to search for hints of new physics in the form of bumps or dips in the spectrum. The results are evaluated and upper cross section limits are computed separately for $g_{KK} \to t\bar{t}$ and for $g_{KK} \to Tt$.

5.9.1 Upper Limits: $g_{KK} \to t\bar{t}$

The search is performed on two combinations of the spectra of g_{KK} ($\to t\bar{t}$): the two channels (muon and electron) and the three scenarios S1, S2 and S3. The most significant deviation of the data from the expected background spectrum is required to appear at the same place in each of the channels of a combination. The analysis are performed adopting the following values of parameters: ($\sin\varphi_L$, $\sin\varphi_{tR}$, $\tan\theta_3$) = (0.33, 1 , 0.2), $\Gamma(g_{KK})$ = 15.3 %(the total decay width of heavy gluon), m_H = 120 GeV(the Higgs boson mass) and $m_{g_{KK}}$ = [0.4 , 3.0] TeV.

Upper limits are set on the cross section times branching ratio for each of the signal models using a profile likelihood-ratio test. The CL prescription [127] is used to derive one-sided 95% CL limits. The results are obtained using the HistFitter [124] framework with all spectra from the six channels, excluding bins with few events with g_{KK} ($\to t\bar{t}$) mass below 400 GeV in the S3 case or above 2.0 TeV in the S1 and S3 case.

The statistical and systematic uncertainties on the expected distributions are included in this CL procedure as nuisance parameters in the likelihood fits. The nuisance parameters for the systematic uncertainties are constrained by a Gaussian probability density function with a width corresponding to the size of the uncertainty considered. Correlations between different channels and bins are taken into account. The product of the various probability density functions forms the likelihood function that is maximized in the fit by adjusting the free parameter (the signal strength) and nuisance parameters. The expected g_{KK} ($\to t\bar{t}$) mass distributions are compared to data in figures 5.25 and 5.26 after a fit of nuisance parameters under the background-only hypothesis. It can be seen that the uncertainties are smaller than in figure 5.22 and 5.23 and that the procedure is able to produce a good-quality fit to the data.

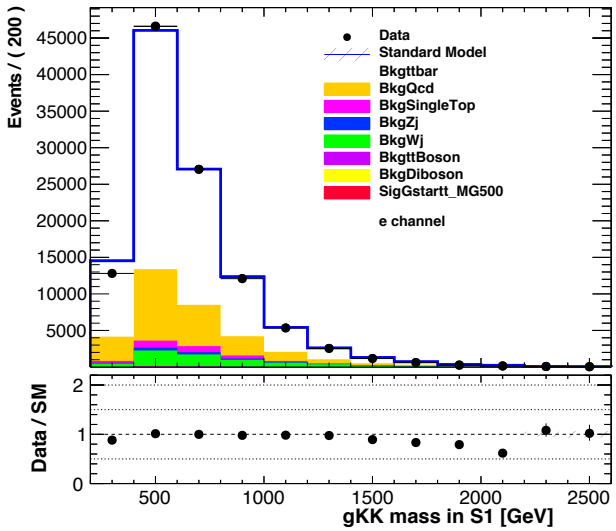

(a) e+jets channel, with $m_{g_{KK}} = 500$ GeV.

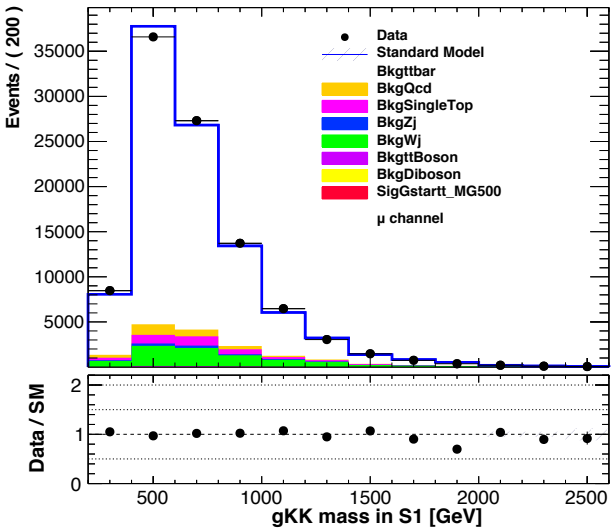

(b) μ+jets channel, with $m_{g_{KK}} = 500$ GeV.

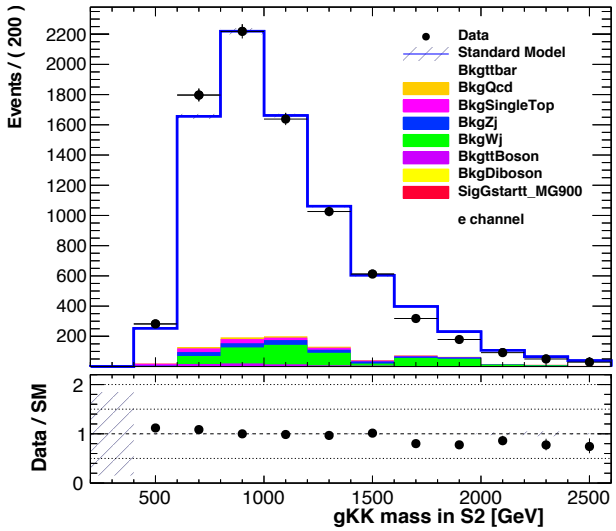

(c) e+jets channel, with $m_{g_{KK}} = 900$ GeV.

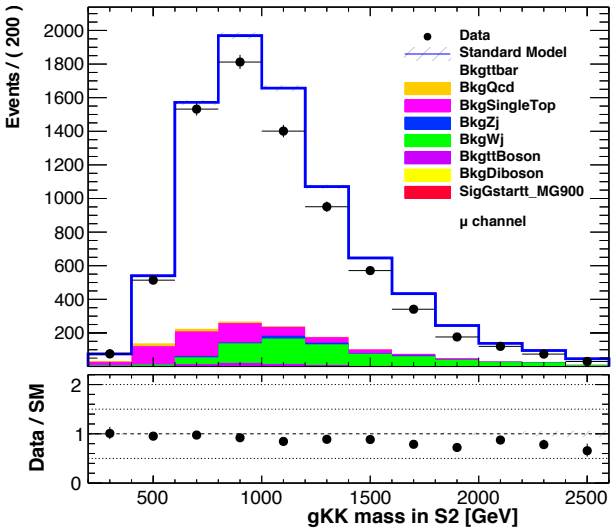

(d) μ+jets channel, with $m_{g_{KK}} = 900$ GeV.

Figure 5.25: Reconstructed g_{KK} ($\rightarrow t\bar{t}$) mass, after nuisance parameter fit, in scenario S1 and S2, in the electron and muon channels. The SM background components are shown as stacked histograms. The shaded areas indicate the total systematic uncertainties.

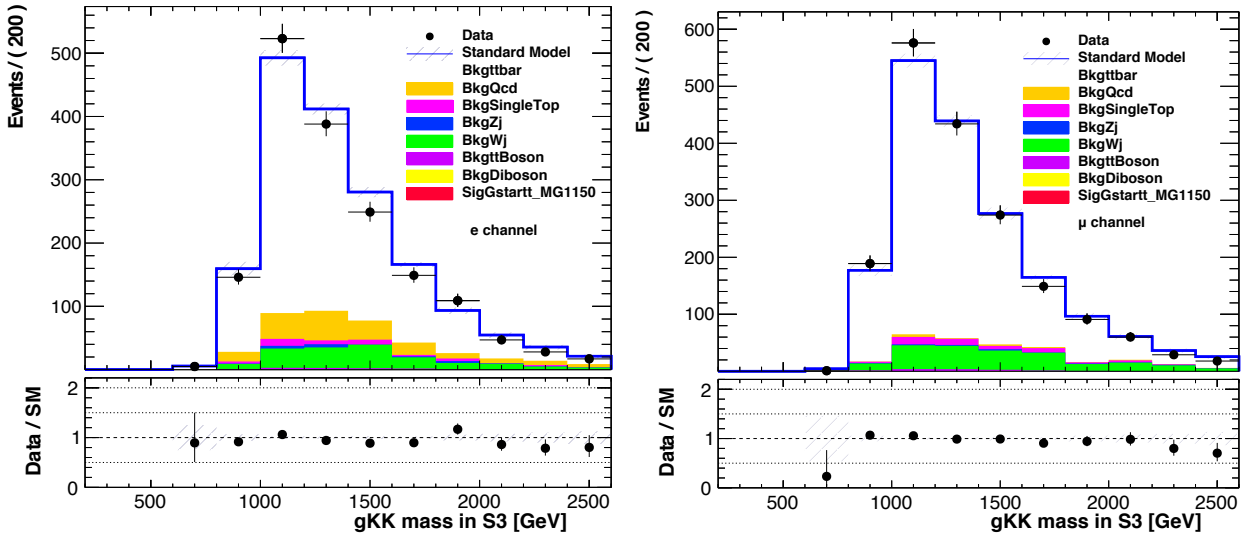

(a) e+jets channel.

(b) μ+jets channel.

Figure 5.26: Reconstructed 1150 GeV g_{KK} ($\rightarrow t\bar{t}$) mass, after nuisance parameter fit, in scenario S3, in the electron and muon channels. The SM background components are shown as stacked histograms. The shaded areas indicate the total systematic uncertainties.

The expected and observed limits using different signal models are presented in figure 5.27. Here the expected limits are obtained by taking the nominal background estimates as the expected data. For the g_{KK} ($\rightarrow t\bar{t}$) benchmark, limits on the production cross-sections vary from 4.8 pb for a mass of 0.4 TeV, to 0.09 pb for a mass of 3 TeV. A g_{KK} of width 15.3% is excluded for masses less than 2.0 TeV, while masses below 2.1 TeV are expected to be excluded.

The observed upper limits on the cross-section times g_{KK} ($\rightarrow t\bar{t}$) branching ratio are greater than the expected limits, for g_{KK} ($\rightarrow t\bar{t}$) resonance masses lower than 1.1 TeV. This arises from a tendency for data to be above the fitted background below 1.0 TeV, as seen in figures 5.25 and 5.26.

The maximisation of the likelihood, which allows the data to constrain the systematic uncertainties using the full g_{KK} ($\rightarrow t\bar{t}$) mass distribution can change the central values of the nuisance parameters and their associated uncertainties. In the region of g_{KK} ($\rightarrow t\bar{t}$) mass where the background prediction as seen in figures 5.22 and 5.23 is slightly higher than the data, we expect to have the observed limits slightly better than the expected ones.

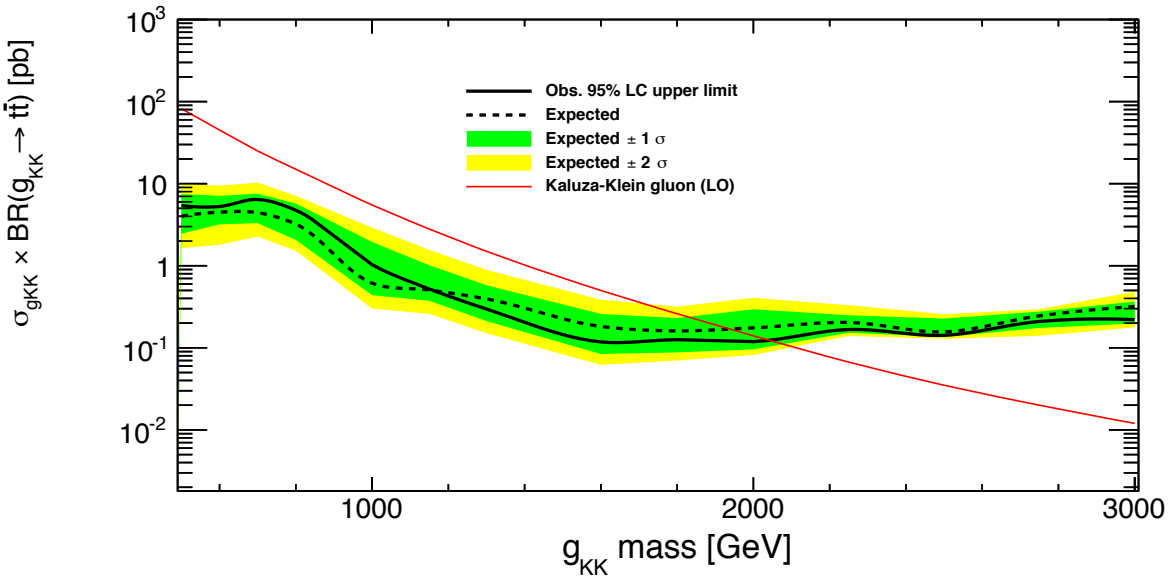

Figure 5.27: Observed and expected upper limits on the production cross-section times branching ratio to $t\bar{t}$ final states as a function of the mass of g_{KK}. The parameters are set to $(\sin\varphi_L, \sin\varphi_{tR}, \tan\theta_3)$ = (0.33, 1 , 0.2), $\Gamma(g_{KK})$ = 15.3 % and m_H = 120 GeV. The expected limits are derived from nominal (pre-fit) background estimates.

5.9.2 Upper Limits: $g_{KK} \to \bar{t}T + \bar{T}t$

The same searches are used to derive exclusion limits on g_{KK} ($\to Tt$) adopting the following values of parameters: $(m_{g_{KK}}, m_T)$ = (1.0 , 0.6), (2.0 , 1.4) TeV, $\tan\theta_3$ = 0.3 (the mixing angle), m_H = 120 GeV (the Higgs boson mass), $\Gamma(g_{KK})$ = 10 % (the total decay width of heavy gluon). We consider simultaneously all VLQ top decay modes described in 5.4 and shown in figures 5.10, 5.11 and 5.12. Upper limits at 95% CL on the Tt production cross sections are set for two benchmark scenarios for each of the g_{KK} mass.

In absence of an excess, the limits are set in the plane defined by the branching ratios to two of the decay modes ($T \to tZ$ and $T \to Wb$) as a function of the signal strength(μ_{sig}). The branching ratio to the third decay mode ($T \to tH$) is fully determined by the requirement that the sum of branching ratios equals unity. We combined the three decay modes, the three scenarios (S1, S2 and S3), muon and electron channels to set 95% CL exclusion limits for two separate g_{KK} mass of 1.0 TeV and 2.0 TeV decaying into a SM top in association with a 0.6 TeV and 1.4 TeV VLQ top, respectively. Figures 5.28 and 5.29 show the observed (in the left) and the expected (in the right) upper limits as a function of the signal strength (μ_{sig}) for $(m_{g_{KK}}, m_T)$ = (1.0 , 0.6) and (2.0 , 1.4) TeV respectively. The value of μ_{sig} doesn't exceed one for $(m_{g_{KK}}, m_T)$ = (1.0 , 0.6), which implies that any VLQ top branching ratio scenario is excluded at 95% CL for $g_{KK} \to Tt$ where the g_{KK} mass is 1.0 TeV.

Figures 5.29 and 5.30a, show that for 2.0 TeV g_{KK}, the signal strength is greater than one ($\mu_{\text{sig}} > 1$) in the region where BR ($T \rightarrow Wb$) > 0.75. Therefore, 95% CL exclusion limits have been set, in this region, for each individual scenario S1, S2 and S3 and the resulting observed and expected exclusion limits versus μ_{sig} are shown in figures 5.32 and 5.31. On the one hand, figures 5.30b and 5.31 show how the combined expected limit improves on the limits from the individual signal regions. On the other hand, the observed exclusion limits results show that, S1 and S2 scenarios have better observed limits (figures 5.32a and 5.32b) than the full combination (figure 5.30a). These results imply that any scenario with BR ($T \rightarrow Wb$) < 0.80 is excluded at 95% CL for $g_{KK} \rightarrow Tt$ where the g_{KK} mass is 2.0 TeV.

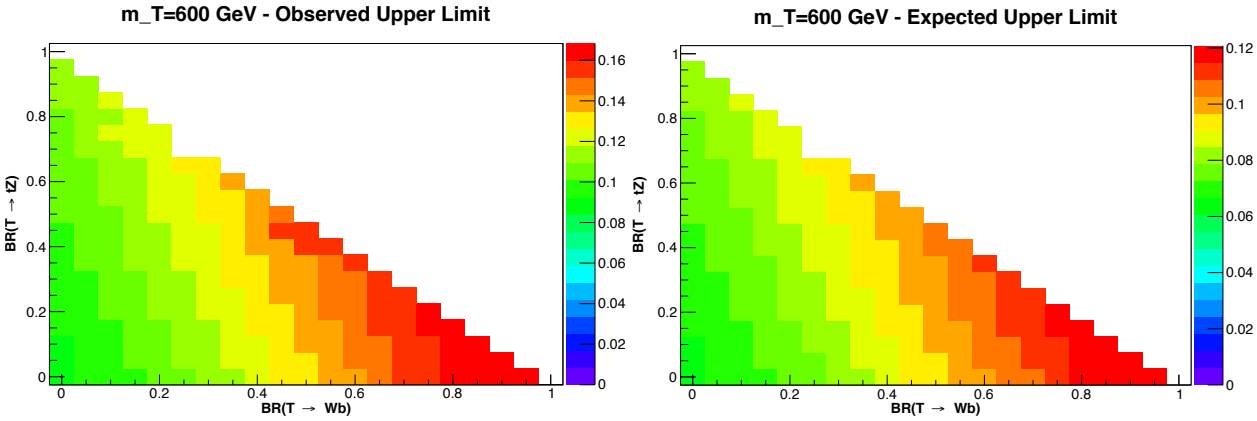

(a) Observed upper limits.

(b) Expected upper limits.

Figure 5.28: Observed and expected 95% CL exclusion as a function of the signal strength(μ_{sig} shown by the right sided axis in color), in the plane of BR ($T \rightarrow Wb$) versus BR($T \rightarrow tZ$), from the combination of the $T \rightarrow Wb$, $T \rightarrow tH$ and $T \rightarrow tZ$ searches. The expected CL exclusion have been set for ($m_{g_{KK}}$, m_T) = (1.0 , 0.6) TeV, $\tan\theta_3 = 0.3$, $m_H = 120$ GeV and $\Gamma(g_{KK}) = 10$ %. The top right area (in white) corresponds to the unphysical region, where the sum of branching ratios exceeds unity.

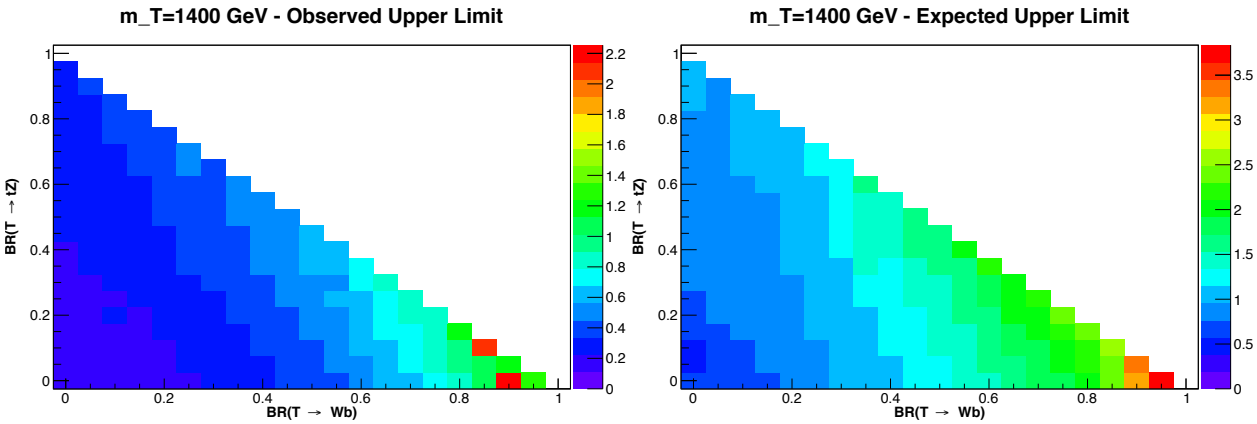

(a) Observed upper limits.

(b) Expected upper limits.

Figure 5.29: Observed and expected 95% CL exclusion as a function of the signal strength(μ_{sig} shown by the right sided axis in color), in the plane of BR ($T \to Wb$) versus BR($T \to tZ$), from the combination of the $T \to Wb$, $T \to tH$ and $T \to tZ$ searches. The CL exclusion have been set for ($m_{g_{KK}}$, m_T) = (2.0 , 1.4) TeV, $\tan\theta_3 = 0.3$, $m_H = 120$ GeV and $\Gamma(g_{KK}) = 10$ %. The top right area (in white) corresponds to the unphysical region, where the sum of branching ratios exceeds unity. The region of BR ($T \to Wb$) where $\mu_{\text{sig}} > 1$ corresponds to the unphysical region.

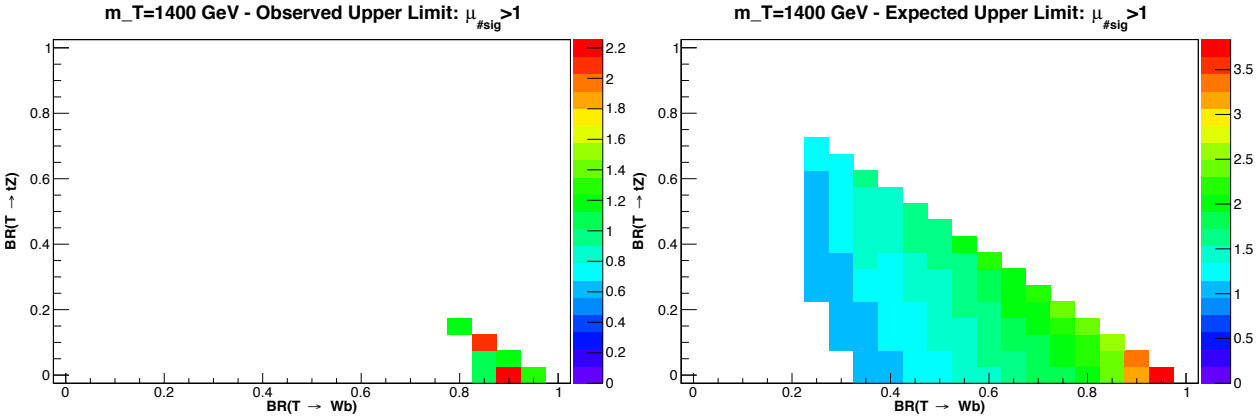

(a) Observed upper limits for combined S1+S2+S3 scenarios.

(b) Expected upper limits for combined S1+S2+S3 scenarios.

Figure 5.30: Observed and expected 95% CL exclusion as a function of the signal strength(μ_{sig} shown by the right sided axis in color) when $\mu_{\text{sig}} > 1$, in the plane of BR ($T \to Wb$) versus BR ($T \to tZ$), from the combination of the $T \to Wb$, $T \to tH$ and $T \to tZ$ searches. The CL exclusion have been set for ($m_{g_{KK}}$, m_T) = (2.0 , 1.4) TeV, $\tan\theta_3 = 0.3$, $m_H = 120$ GeV and $\Gamma(g_{KK}) = 10$ %.

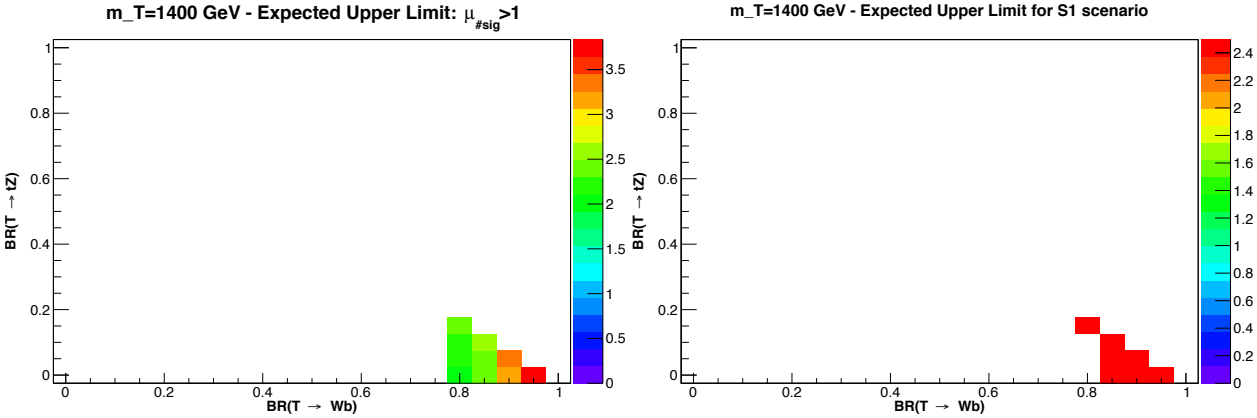

(a) Expected upper limits for combined S1+S2+S3 scenarios.

(b) Expected upper limits for S1 scenario only.

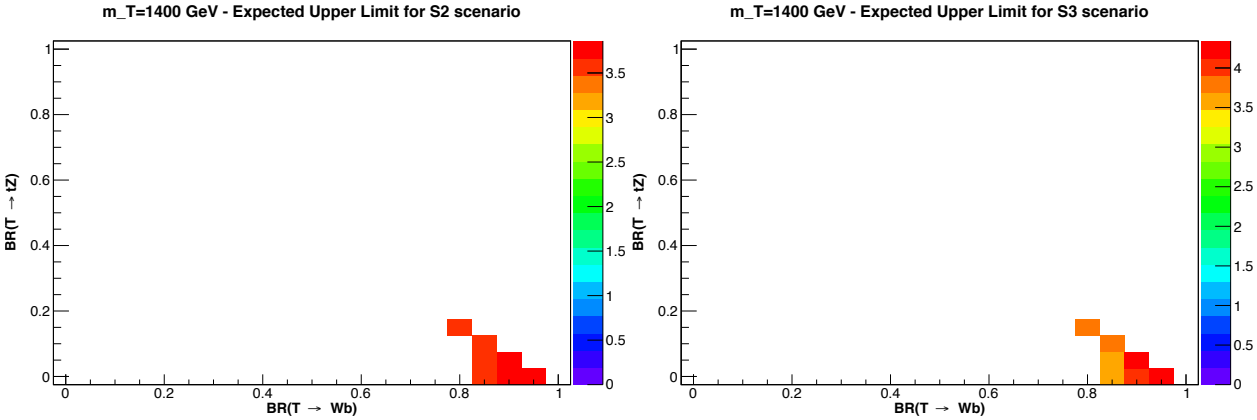

(c) Expected upper limits for S2 scenario only.

(d) Expected upper limits for S3 scenario only.

Figure 5.31: Expected 95% CL exclusion as a function of the signal strength(μ_{sig} shown by the right sided axis in color) when $\mu_{\text{sig}} > 1$, in the plane of BR ($T \rightarrow Wb$) versus BR ($T \rightarrow tZ$), from the combination of the $T \rightarrow Wb$, $T \rightarrow tH$ and $T \rightarrow tZ$ searches. The CL exclusion have been set for ($m_{g_{KK}}$, m_T) = (2.0 , 1.4) TeV, $\tan\theta_3 = 0.3$, $m_H = 120$ GeV and $\Gamma(g_{KK}) = 10$ %.

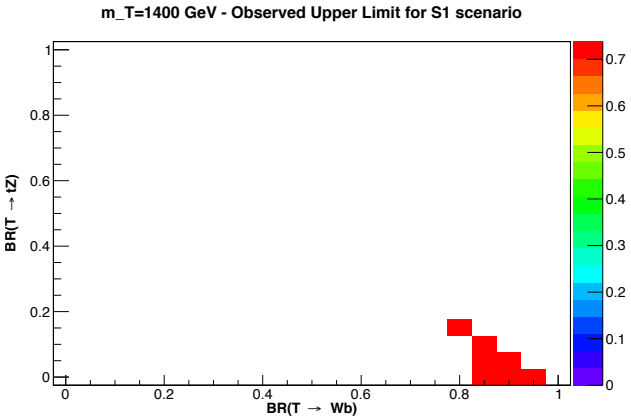

(a) Observed upper limits for S1 scenario only.

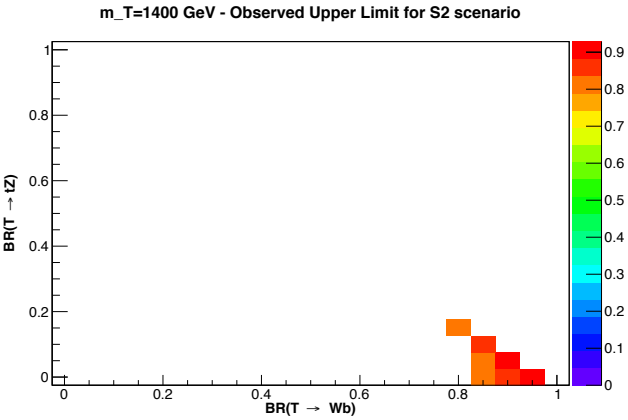

(b) Observed upper limits for S2 scenario only.

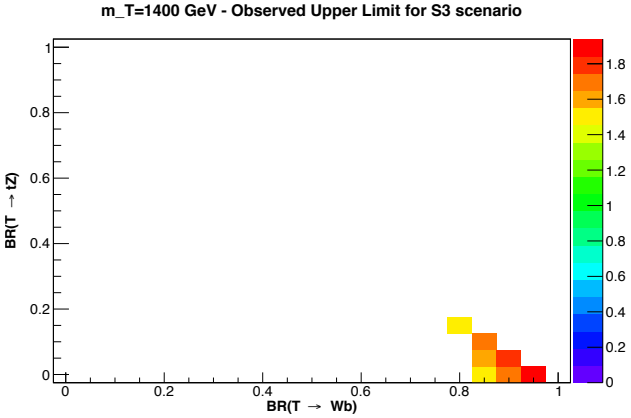

(c) Observed upper limits for S3 scenario only.

Figure 5.32: Observed 95% CL exclusion as a function of the signal strength(μ_{sig} shown by the right sided axis in color) when $\mu_{\text{sig}} > 1$, in the plane of BR ($T \rightarrow Wb$) versus BR ($T \rightarrow tZ$), from the combination of the $T \rightarrow Wb$, $T \rightarrow tH$ and $T \rightarrow tZ$ searches. The CL exclusion have been set for ($m_{g_{KK}}$, m_T) = (2.0 , 1.4) TeV, $\tan\theta_3 = 0.3$, $m_H = 120$ GeV and $\Gamma(g_{KK}) = 10$ %.

6 Conclusion

The discovery of the 125 GeV Higgs boson at the LHC, raised a general interest for theories BSM such as models with additional VLQ top compatible with current measurements of SM. In parallel, with the effective theory of the heavy gluon, the lightest Kaluza-Klein excitation of gluon (g_{KK}) is introduced in theories with a warped extra dimension with a coupling to SM top quarks and VLQ top large enough, so that, if kinematically allowed, g_{KK} decays with a large rate, to a pair of top quarks ($g_{KK} \to t\bar{t}$ or $g_{KK} \to T\bar{T}$) or to a SM top quark in association with a VLQ top ($g_{KK} \to T\bar{t}$) . The VLQ top , from the effective theory of the top partners, is a $SU(2)_L$ doublet with charge $+2/3$. According to its largest coupling, it decays to Wb, Zt or Ht (t and H stand for SM top and Composite Higgs, respectively).

Two independent searches for $g_{KK} \to t\bar{t}$ (Kaluza-Klein excitation of gluon with a branching ratio of 100% into a SM top quark pairs in a Randall–Sundrum model) and $g_{KK} \to \bar{t}T$ (Kaluza-Klein excitation of gluon in a composite model where the heavy gluon decays to tT, using benchmark parameters for mixing angles) in the lepton-plus-jets decay channel were carried out with the ATLAS experiment at the LHC. The searches use data corresponding to an integrated luminosity of 20.3 fb^{-1} of proton–proton collisions at a centre-of-mass energy of 8 TeV. No excess of events beyond the Standard Model predictions is observed in the $t\bar{t}$ and the $T\bar{t}$ invariant mass spectra. Upper limits on the cross-section times branching ratio are set for a broad (15.3% width) $g_{KK} \to t\bar{t}$ and two (10% width) $g_{KK} \to \bar{t}T$ point masses. Based on the results, a $g_{KK} \to t\bar{t}$ of width 15.3% is excluded for masses less than 2.0 TeV, while masses below 2.1 TeV are expected to be excluded at 95% CL.

Furthermore, every VLQ top branching ratio scenario is excluded at 95% CL for $g_{KK} \to \bar{t}T$ where the g_{KK} mass is 1.0 TeV. Finally, any scenario with BR ($T \to Wb$) < 0.80 is excluded at 95% CL for $g_{KK} \to \bar{t}T$ where the g_{KK} mass is 2.0 TeV.

The samples used in these analyses were validated by ATLAS collaboration, however the results shown in this thesis were not reviewed by the ATLAS collaboration for publication.

Bibliography

[1] Aad, G. et al., *A search for $t\bar{t}$ resonances using lepton-plus-jets events in proton-proton collisions at $\sqrt{s} = 8$ TeV with the ATLAS detector*. JHEP, **08**: 148 (2015), doi:10.1007/JHEP08(2015)148, arXiv:1505.07018. iii, 3, 96

[2] Aad, G. et al., *Measurement of the top pair production cross section in 8 TeV proton-proton collisions using kinematic information in the lepton+jets final state with ATLAS*. Phys. Rev., **D91** (11): 112 013 (2015), doi:10.1103/PhysRevD.91.112013, arXiv:1504.04251. iii

[3] Aaboud, M. et al., *Performance of the ATLAS Transition Radiation Tracker in Run 1 of the LHC: tracker properties*. JINST, **12** (05): P05 002 (2017), doi:10.1088/1748-0221/12/05/P05002, arXiv:1702.06473. iii

[4] Beringer et Group, P. D., *The Review of Particle Physics*. Physical Review D, **86** (1): 010 001 (2012). xvii, 5, 10, 24, 27

[5] Peskin, M. E. et Schroeder, D. V., *An introduction to quantum field theory*. Advanced book program, Westview Press Reading (Mass.), Boulder (Colo.) (1995), ISBN 0-201-50934-2, URL `http://opac.inria.fr/record=b1131978`. Autre tirage : 1997. xvii, 9, 11

[6] Denner, A., Heinemeyer, S., Puljak, I. et al., *Standard Model Higgs-Boson Branching Ratios with Uncertainties*. Eur. Phys. J., **C71**: 1753 (2011), doi:10.1140/epjc/s10052-011-1753-8, arXiv:1107.5909. xvii, 11

[7] Perkins, D. H., *Introduction to High Energy Physics*. Daniel V. Schroeder (2000), ISBN 9780521621960. xvii, 1, 3, 6, 8, 9, 10, 13, 15

[8] Gabella, M., *The Randall-Sundrum Model* (June 2006. Online), URL `https://www-thphys.physics.ox.ac.uk/people/MaximeGabella/rs.pdf`. xvii, 17, 18

[9] Bini, C., Contino, R. et Vignaroli, N., *Heavy-light decay topologies as a new strategy to discover a heavy gluon*. JHEP, **01**: 157 (2012), doi:10.1007/JHEP01(2012)157, arXiv:1110.6058. xvii, 20, 22, 23, 25, 26, 28, 29, 30, 60, 73

[10] Stirling, J., *The cross sections of the SM particles as a function of collider energy* (Revision 1,14 August 2013. Online), URL http://www.hep.ph.ic.ac.uk/~wstirlin/plots/plots.html. xviii, 33, 34

[11] ATLAS Experiment, *Luminosity Public Results for 2011-2012 data taking*. (2013), URL https://twiki.cern.ch/twiki/bin/view/AtlasPublic/LuminosityPublicResults?rev=43. (Revision 43, 17 August 2013. Online). xix, xxi, 46, 59

[12] Aad, G. et al., *Improved luminosity determination in pp collisions at sqrt(s) = 7 TeV using the ATLAS detector at the LHC*. Eur. Phys. J., **C73** (8): 2518 (2013), doi:10.1140/epjc/s10052-013-2518-3, arXiv:1302.4393. xix, 46, 85

[13] Aad, G. et al., *Performance of the ATLAS Trigger System in 2010*. Eur. Phys. J., **C72**: 1849 (2012), doi:10.1140/epjc/s10052-011-1849-1, arXiv:1110.1530. xx, 47, 48, 49

[14] Dorigo, T., *ATLAS Seeks Invisible Particles With Top Quarks* (4 August 2014. Online), URL http://www.science20.com/a_quantum_diaries_survivor/atlas_seeks_invisible_particles_with_top_quarks-148371. xx, 56

[15] Aad, G. et al., *Observation of a new particle in the search for the Standard Model Higgs boson with the ATLAS detector at the LHC*. Phys. Lett., **B716**: 1–29 (2012), doi:10.1016/j.physletb.2012.08.020, arXiv:1207.7214. 1, 10, 12, 16

[16] Chatrchyan, S. et al., *Observation of a new boson at a mass of 125 GeV with the CMS experiment at the LHC*. Phys. Lett., **B716**: 30–61 (2012), doi:10.1016/j.physletb.2012.08.021, arXiv:1207.7235. 1, 10, 16

[17] Lee, T. D., *A Theory of Spontaneous T Violation*. Phys. Rev., **D8**: 1226–1239 (1973), doi:10.1103/PhysRevD.8.1226. [,516(1973)]. 2

[18] Branco, G. C., Ferreira, P. M., Lavoura, L. et al., *Theory and phenomenology of two-Higgs-doublet models*. Phys. Rept., **516**: 1–102 (2012), doi:10.1016/j.physrep.2012.02.002, arXiv:1106.0034. 2

[19] Randall, L. et Sundrum, R., *A Large mass hierarchy from a small extra dimension*. Phys. Rev., **83**: 3370–3373 (1999), doi:10.1103/PhysRevLett.83.3370, arXiv:hep-ph/9905221. 2, 18, 19

[20] Agashe, K., Delgado, A., May, M. J. et Sundrum, R., *RS1, custodial isospin and precision tests*. JHEP, **08**: 050 (2003), doi:10.1088/1126-6708/2003/08/050, arXiv:hep-ph/0308036.

[21] Davoudiasl, H., Hewett, J. L. et Rizzo, T. G., *Bulk gauge fields in the Randall-Sundrum model*. Phys. Lett., **B473**: 43–49 (2000), doi:10.1016/S0370-2693(99)01430-6, arXiv:hep-ph/9911262. 20, 30

[22] Pomarol, A., *Gauge bosons in a five-dimensional theory with localized gravity*. Phys. Lett., **B486**: 153–157 (2000), doi:10.1016/S0370-2693(00)00737-1, arXiv:hep-ph/9911294. 2

[23] Kaplan, D. B. et Georgi, H., *SU(2) x U(1) Breaking by Vacuum Misalignment*. Phys. Lett., **B136**: 183–186 (1984), doi:10.1016/0370-2693(84)91177-8. 2

[24] Kaplan, D. B., Georgi, H. et Dimopoulos, S., *Composite Higgs Scalars*. Phys. Lett., **B136**: 187–190 (1984), doi:10.1016/0370-2693(84)91178-X.

[25] Georgi, H., Kaplan, D. B. et Galison, P., *Calculation of the Composite Higgs Mass*. Phys. Lett., **B143**: 152–154 (1984), doi:10.1016/0370-2693(84)90823-2.

[26] Georgi, H. et Kaplan, D. B., *Composite Higgs and Custodial SU(2)*. Phys. Lett., **B145**: 216–220 (1984), doi:10.1016/0370-2693(84)90341-1.

[27] Dugan, M. J., Georgi, H. et Kaplan, D. B., *Anatomy of a Composite Higgs Model*. Nucl. Phys., **B254**: 299–326 (1985), doi:10.1016/0550-3213(85)90221-4.

[28] Georgi, H., *A Tool Kit for Builders of Composite Models*. Nucl. Phys., **B266**: 274–284 (1986), doi:10.1016/0550-3213(86)90092-1.

[29] Bellazzini, B., Csáki, C. et Serra, J., *Composite Higgses*. Eur. Phys. J., **C74** (5): 2766 (2014), doi:10.1140/epjc/s10052-014-2766-x, arXiv:1401.2457. 2

[30] Langacker, P., *Theoretical Study of the Electroweak Interaction–Present and Future*. Arxiv preprint (hep-ph) (1994), URL arXiv:hep-ph/9408310. 3

[31] Nakamura, K. et Group, P. D., *The Review of Particle Physics*. Journal of Physics G: Nuclear and Particle Physics, **37** (7A): 075 021 (2010). 8

[32] Peskin, M. E. et Schroeder., D. V., *Quantum field theory*. Cambridge University Press (1995), ISBN 9780201503975. 3

[33] Wagner, W., *Top quark physics in hadron collisions*. Rept. Prog. Phys., **68**: 2409–2494 (2005), doi:10.1088/0034-4885/68/10/R03, arXiv:hep-ph/0507207. 10

[34] Kidonakis, N., *Differential and total cross sections for top pair and single top production*. Dans *Proceedings, 20th International Workshop on Deep-Inelastic Scattering and Related Subjects (DIS 2012): Bonn, Germany, March 26-30, 2012*, pages 831–834 (2012), doi:10.3204/DESY-PROC-2012-02/251, arXiv:1205.3453, URL https://inspirehep.net/record/1114754/files/arXiv:1205.3453.pdf. [,831(2012)]. 10

[35] Chatrchyan, S. et al., *Observation of a new boson at a mass of 125 GeV with the CMS experiment at the LHC*. Phys. Lett., **B716**: 30–61 (2012), doi:10.1016/j.physletb.2012.08.021, arXiv:1207.7235. 12

[36] Cline, J. M., *Baryogenesis*. Dans *Les Houches Summer School - Session 86: Particle Physics and Cosmology: The Fabric of Spacetime Les Houches, France, July 31-August 25, 2006* (2006), arXiv:hep-ph/0609145. 13

[37] Stecker, F. W., *Baryon Symmetric Big Bang Cosmology*. Nature, **273**: 493–497 (1978), doi:10.1038/273493a0. 13

[38] Fajfer, S., Greljo, A., Kamenik, J. F. et Mustac, I., *Light Higgs and Vector-like Quarks without Prejudice*. JHEP, **07**: 155 (2013), doi:10.1007/JHEP07(2013)155, arXiv:1304.4219. 13

[39] Arkani-Hamed, N., Dimopoulos, S. et Dvali, G. R., *Phenomenology, astrophysics and cosmology of theories with submillimeter dimensions and TeV scale quantum gravity*. Phys. Rev., **D59**: 086 004 (1999), doi:10.1103/PhysRevD.59.086004, arXiv:hep-ph/9807344. 16

[40] Schmaltz, M. et Tucker-Smith, D., *Little Higgs review*. Ann. Rev. Nucl. Part. Sci., **55**: 229–270 (2005), doi:10.1146/annurev.nucl.55.090704.151502, arXiv:hep-ph/0502182. 17

[41] Csaki, C., Marandella, G., Shirman, Y. et Strumia, A., *The Super-little Higgs*. Phys. Rev., **D73**: 035 006 (2006), doi:10.1103/PhysRevD.73.035006, arXiv:hep-ph/0510294. 17

[42] Perelstein, M., *Little Higgs models and their phenomenology*. Prog. Part. Nucl. Phys., **58**: 247–291 (2007), doi:10.1016/j.ppnp.2006.04.001, arXiv:hep-ph/0512128. 17

[43] Arkani-Hamed, N., Cohen, A. G. et Georgi, H., *Electroweak symmetry breaking from dimensional deconstruction*. Phys. Lett., **B513**: 232–240 (2001), doi:10.1016/S0370-2693(01)00741-9, arXiv:hep-ph/0105239. 17

[44] Kaluza, T., *Zum Unitätsproblem der Physik* (1921). 17

[45] Polchinski, J., *String Theory. vol I*, chapitre 8:Toroidal compactification and T-duality. Cambridge (1995). 17

[46] Arkani-Hamed, N., Dimopoulos, S. et Dvali, G. R., *Phenomenology, astrophysics and cosmology of theories with submillimeter dimensions and TeV scale quantum gravity*. Phys. Rev., **D59**: 086 004 (1999), doi:10.1103/PhysRevD.59.086004, arXiv:hep-ph/9807344. 17

[47] L. Randall, R. S., *An Alternative to Compactification.* Phys. Rev., **83** (23): 83,4690 (1999). 18

[48] Gaberdiel, M. R., *An Introduction to Conformal Field Theory.* Rept. Prog. Phys., **63** (4): 607–667 (2000), URL arXiv:hep-th/9910156. 19

[49] K. Agashe, A. P., R. Contino, *The Minimal Composite Higgs Model.* Nucl. Phys B, **719**: 165–187 (2005), URL arXiv:hep-ph/0412089.

[50] Aharony, O., Gubser, S., Maldacena, J. et al., *Large N Field Theories, String Theory and Gravity*. Phys. Rept., **323** (3): 183–386 (2000), URL arXiv:hep-th/9905111. 19

[51] Nima Arkani-Hamed, L. R., Massimo Porrati, *Holography and Phenomenology.* Journal of High Energy Physics, **2001** (08): 017 (2001), URL arXiv:hep-th/0012148. 20

[52] Lillie, B., Randall, L. et Wang, L.-T., *The Bulk RS KK-gluon at the LHC*. JHEP, **09**: 074 (2007), doi:10.1088/1126-6708/2007/09/074, arXiv:hep-ph/0701166. 20, 30, 73

[53] Contino, R., Nomura, Y. et Pomarol, A., *Higgs as a holographic pseudoGoldstone boson*. Nucl. Phys., **B671**: 148–174 (2003), doi:10.1016/j.nuclphysb.2003.08.027, arXiv:hep-ph/0306259. 20, 30

[54] Grossman, Y. et Neubert, M., *Neutrino masses and mixings in nonfactorizable geometry*. Phys. Lett., **B474**: 361–371 (2000), doi:10.1016/S0370-2693(00)00054-X, arXiv:hep-ph/9912408. 22

[55] Gherghetta, T. et Pomarol, A., *Bulk fields and supersymmetry in a slice of AdS*. Nucl. Phys., **B586**: 141–162 (2000), doi:10.1016/S0550-3213(00)00392-8, arXiv:hep-ph/0003129.

[56] Huber, S. J. et Shafi, Q., *Fermion masses, mixings and proton decay in a Randall-Sundrum model*. Phys. Lett., **B498**: 256–262 (2001), doi:10.1016/S0370-2693(00)01399-X, arXiv:hep-ph/0010195. 22

[57] Redi, M. et Weiler, A., *Flavor and CP Invariant Composite Higgs Models*. JHEP, **11**: 108 (2011), doi:10.1007/JHEP11(2011)108, arXiv:1106.6357. 23

[58] Fitzpatrick, A. L., Perez, G. et Randall, L., *Flavor anarchy in a Randall-Sundrum model with 5D minimal flavor violation and a low Kaluza-Klein scale*. Phys. Rev. Lett., **100**: 171 604 (2008), doi:10.1103/PhysRevLett.100.171604, arXiv:0710.1869. 23

[59] Santiago, J., *Minimal Flavor Protection: A New Flavor Paradigm in Warped Models*. JHEP, **12**: 046 (2008), doi:10.1088/1126-6708/2008/12/046, arXiv:0806.1230.

[60] Csaki, C., Falkowski, A. et Weiler, A., *A Simple Flavor Protection for RS*. Phys. Rev., **D80**: 016 001 (2009), doi:10.1103/PhysRevD.80.016001, arXiv:0806.3757.

[61] Csaki, C., Perez, G., Surujon, Z. et Weiler, A., *Flavor Alignment via Shining in RS*. Phys. Rev., **D81**: 075 025 (2010), doi:10.1103/PhysRevD.81.075025, arXiv:0907.0474. 23

[62] Contino, R., Da Rold, L. et Pomarol, A., *Light custodians in natural composite Higgs models*. Phys. Rev., **D75**: 055 014 (2007), doi:10.1103/PhysRevD.75.055014, arXiv:hep-ph/0612048. 23

[63] Aad, G. et al., *The ATLAS Experiment at the CERN Large Hadron Collider*. JINST, **3**: S08 003 (2008), doi:10.1088/1748-0221/3/08/S08003. 36, 43

[64] Aad G., e. a., *ATLAS inner detector: Technical design report.* Journal of Instrumentation, **1** (1997). 36

[65] Collaboration., T. A., *A search for $\mathrm{t\bar{t}}$ resonances using lepton plus jets events in proton-proton collisions at $\sqrt{s} = 8$ TeV with the ATLAS detector*. Prépublication ATLAS-CONF-2015-009, CERN, Geneva (2015), URL http://cds.cern.ch/record/2002440. 44, 54, 77, 84

[66] Aad, G. et al., *Luminosity Determination in pp Collisions at $\sqrt{s} = 7$ TeV Using the ATLAS Detector at the LHC*. Eur. Phys. J., **C71**: 1630 (2011), doi:10.1140/epjc/s10052-011-1630-5, arXiv:1101.2185. 46

[67] Aad G., e. a., *Electron reconstruction and identification efficiency measurements with the ATLAS detector using the 2011 LHC proton-proton collision data.* Eur.Phys.J.C, **74** (2014), URL arXiv:1404.2240. 49

[68] Aad G., e. a., *Object selection and calibration, background estimations and MC samples for the Winter 2013 Top Quark analyses with 2012 data.* ATL-COM-PHYS, **088** (2013). 49, 50

[69] Rehermann, K. et Tweedie, B., *Efficient Identification of Boosted Semileptonic Top Quarks at the LHC*. JHEP, **03**: 059 (2011), doi:10.1007/JHEP03(2011)059, arXiv:1007.2221. 49

[70] Aad, G. et al., *Measurement of the muon reconstruction performance of the ATLAS detector using 2011 and 2012 LHC proton–proton collision data*. Eur. Phys. J., **C74** (11): 3130 (2014), doi:10.1140/epjc/s10052-014-3130-x, arXiv:1407.3935. 50

[71] Cacciari, M., Salam, G. P. et Soyez, G., *The Anti-k(t) jet clustering algorithm*. JHEP, **04**: 063 (2008), doi:10.1088/1126-6708/2008/04/063, arXiv:0802.1189. 51

[72] Ellis, S. D. et Soper, D. E., *Successive combination jet algorithm for hadron collisions*. Phys. Rev., **D48**: 3160–3166 (1993), doi:10.1103/PhysRevD.48.3160, arXiv:hep-ph/9305266. 51

[73] Cacciari, M., Salam, G. P. et Soyez, G., *FastJet User Manual*. Eur. Phys. J., **C72**: 1896 (2012), doi:10.1140/epjc/s10052-012-1896-2, arXiv:1111.6097. 51

[74] Aad, G. et al., *Jet energy measurement and its systematic uncertainty in proton-proton collisions at $\sqrt{s} = 7$ TeV with the ATLAS detector*. Eur. Phys. J., **C75**: 17 (2015), doi:10.1140/epjc/s10052-014-3190-y, arXiv:1406.0076. 51, 52, 84

[75] Aad, G. et al., *Performance of pile-up mitigation techniques for jets in pp collisions at $\sqrt{s} = 8$ TeV using the ATLAS detector*. Eur. Phys. J. (2015), arXiv:1510.03823. 52, 53

[76] Aad, G. et al., *Pile-up subtraction and suppression for jets in ATLAS*. Eur. Phys. J. (2013), URL https://cds.cern.ch/record/1570994. 52

[77] Aad, G. et al., *Jet energy measurement with the ATLAS detector in proton-proton collisions at $\sqrt{s} = 7$ TeV*. Eur. Phys. J., **C73** (3): 2304 (2013), doi:10.1140/epjc/s10052-013-2304-2, arXiv:1112.6426. 52, 84

[78] B. Butler, A. S., *Track-Jet Reconstruction and Performance*. ATL-PHYS-INT, **040** (2010). 52

[79] Aad, G. et al., *Jet energy resolution and selection efficiency relative to track jets from in-situ techniques with the ATLAS Detector Using Proton-Proton Collisions at a Center of Mass Energy $sqrts = 7$ TeV*. Prépublication ATLAS-CONF-2010-054, CERN, Geneva (2010), URL https://cds.cern.ch/record/1281311. 52

[80] D.W. Miller, D. S., A. Schwartzman, *Pile-up jet energy scale corrections using the jet-vertex fraction method*. Technical Report, **180**: 25 (2009). 52

[81] Aad, G. et al., *Selection of jets produced in proton-proton collisions with the ATLAS detector using 2011 data*. Prépublication ATLAS-CONF-2012-020, CERN, Geneva (2012), URL https://cds.cern.ch/record/1430034. 53

[82] Grahn, K., *Recommendations for jet cleaning for data 2011*. (2013), URL https://twiki.cern.ch/twiki/bin/view/AtlasProtected/TopJetLiaisonR172Recommendations. (Revision 31, 17 April 2013. Online). 53

[83] Cacciari, M., Salam, G. P. et Soyez, G., *FastJet*. (26 February 2010. Online), URL http://fastjet.fr. 53

[84] Krohn, D., Thaler, J. et Wang, L.-T., *Jet Trimming*. JHEP, **02**: 084 (2010), doi:10.1007/JHEP02(2010)084, arXiv:0912.1342. 53

[85] Aad, G. et al., *Performance of large-R jets and jet substructure reconstruction with the ATLAS detector*. Prépublication ATLAS-CONF-2012-065, CERN, Geneva (2012), URL http://cds.cern.ch/record/1459530. 53, 84

[86] Aad G., e. a., *Commissioning of the ATLAS high-performance b-tagging algorithms in the 7 TeV collision data*. ATLAS-CONF-2011-102 (2011). 54

[87] Aad G., e. a., *Performance of the ATLAS Secondary Vertex b-tagging Algorithm in 7 TeV Collision Data*. ATLAS-CONF-2010-042 (2010). 54

[88] Flavour Tagging Conveners, *ATLAS Flavour Tagging Working Group*. (2016), URL https://twiki.cern.ch/twiki/bin/viewauth/AtlasProtected/FlavourTagging. (Revision 229, 24 Mai 2016. Online). 54

[89] Aad, G. et al., *Performance of Missing Transverse Momentum Reconstruction in Proton-Proton Collisions at 7 TeV with ATLAS*. Eur. Phys. J., **C72**: 1844 (2012), doi:10.1140/epjc/s10052-011-1844-6, arXiv:1108.5602. 56, 57, 58

[90] Luminosity Conveners, *Luminosity Public Results.* (Revision 44, 20 June 2015. Online), URL https://twiki.cern.ch/twiki/bin/view/AtlasPublic/LuminosityPublicResults. 59

[91] Carmona, A., Chala, M. et Santiago, J., *New Higgs Production Mechanism in Composite Higgs Models*. JHEP, **07**: 049 (2012), doi:10.1007/JHEP07(2012)049, arXiv:1205.2378. 60

[92] Alwall, J., Demin, P., de Visscher, S. et al., *MadGraph/MadEvent v4: The New Web Generation*. JHEP, **09**: 028 (2007), doi:10.1088/1126-6708/2007/09/028, arXiv:0706.2334. 73

[93] Frixione, S., Nason, P. et Ridolfi, G., *A Positive-weight next-to-leading-order Monte Carlo for heavy flavour hadroproduction*. JHEP, **09**: 126 (2007), doi:10.1088/1126-6708/2007/09/126, arXiv:0707.3088. 82

[94] Nason, P., *A New method for combining NLO QCD with shower Monte Carlo algorithms*. JHEP, **11**: 040 (2004), doi:10.1088/1126-6708/2004/11/040, arXiv:hep-ph/0409146.

[95] Frixione, S., Nason, P. et Oleari, C., *Matching NLO QCD computations with Parton Shower simulations: the POWHEG method*. JHEP, **11**: 070 (2007), doi:10.1088/1126-6708/2007/11/070, arXiv:0709.2092.

[96] Alioli, S., Nason, P., Oleari, C. et Re, E., *A general framework for implementing NLO calculations in shower Monte Carlo programs: the POWHEG BOX*. JHEP, **06**: 043 (2010), doi:10.1007/JHEP06(2010)043, arXiv:1002.2581. 82

[97] Sjostrand, T., Mrenna, S. et Skands, P. Z., *PYTHIA 6.4 Physics and Manual*. JHEP, **05**: 026 (2006), doi:10.1088/1126-6708/2006/05/026, arXiv:hep-ph/0603175. 82

[98] Skands, P. Z., *Tuning Monte Carlo Generators: The Perugia Tunes*. Phys. Rev., **D82**: 074 018 (2010), doi:10.1103/PhysRevD.82.074018, arXiv:1005.3457. 82

[99] Lai, H.-L., Guzzi, M., Huston, J. et al., *New parton distributions for collider physics*. Phys. Rev., **D82**: 074 024 (2010), doi:10.1103/PhysRevD.82.074024, arXiv:1007.2241. 82, 86

[100] Alioli, S., Nason, P., Oleari, C. et Re, E., *NLO single-top production matched with shower in POWHEG: s- and t-channel contributions*. JHEP, **09**: 111 (2009), doi:10.1007/JHEP02(2010)011,10.1088/1126-6708/2009/09/111, arXiv:0907.4076. [Erratum: JHEP02,011(2010)]. 82, 83

[101] Frederix, R., Re, E. et Torrielli, P., *Single-top t-channel hadroproduction in the four-flavour scheme with POWHEG and aMC@NLO*. JHEP, **09**: 130 (2012), doi:10.1007/JHEP09(2012)130, arXiv:1207.5391.

[102] Re, E., *Single-top Wt-channel production matched with parton showers using the POWHEG method*. Eur. Phys. J., **C71**: 1547 (2011), doi:10.1140/epjc/s10052-011-1547-z, arXiv:1009.2450. 83

[103] Frixione, S., Laenen, E., Motylinski, P. et al., *Single-top hadroproduction in association with a W boson*. JHEP, **07**: 029 (2008), doi:10.1088/1126-6708/2008/07/029, arXiv:0805.3067. 83

[104] Gavin, R., Li, Y., Petriello, F. et Quackenbush, S., *W Physics at the LHC with FEWZ 2.1*. Comput. Phys. Commun., **184**: 208–214 (2013), doi:10.1016/j.cpc.2012.09.005, arXiv:1201.5896. 83

[105] Gleisberg, T., Hoeche, S., Krauss, F. et al., *Event generation with SHERPA 1.1*. JHEP, **02**: 007 (2009), doi:10.1088/1126-6708/2009/02/007, arXiv:0811.4622. 83

[106] Hoeche, S., Krauss, F., Schumann, S. et Siegert, F., *QCD matrix elements and truncated showers*. JHEP, **05**: 053 (2009), doi:10.1088/1126-6708/2009/05/053, arXiv:0903.1219.

[107] Gleisberg, T. et Hoeche, S., *Comix, a new matrix element generator*. JHEP, **12**: 039 (2008), doi:10.1088/1126-6708/2008/12/039, arXiv:0808.3674.

[108] Schumann, S. et Krauss, F., *A Parton shower algorithm based on Catani-Seymour dipole factorisation*. JHEP, **03**: 038 (2008), doi:10.1088/1126-6708/2008/03/038, arXiv:0709.1027. 83

[109] Campbell, J. M. et Ellis, R. K., *MCFM for the Tevatron and the LHC*. Nucl. Phys. Proc. Suppl., **205-206**: 10–15 (2010), doi:10.1016/j.nuclphysbps.2010.08.011, arXiv:1007.3492. 83

[110] Garzelli, M. V., Kardos, A., Papadopoulos, C. G. et Trocsanyi, Z., *$t\,\bar{t}\,W^{+-}$ and $t\,\bar{t}\,Z$ Hadroproduction at NLO accuracy in QCD with Parton Shower and Hadronization effects*. JHEP, **11**: 056 (2012), doi:10.1007/JHEP11(2012)056, arXiv:1208.2665. 83

[111] Aad, G. et al., *Jet mass and substructure of inclusive jets in $\sqrt{s} = 7$ TeV pp collisions with the ATLAS experiment*. JHEP, **05**: 128 (2012), doi:10.1007/JHEP05(2012)128, arXiv:1203.4606. 84

[112] Aad, G. et al., *Measurement of the b-tag Efficiency in a Sample of Jets Containing Muons with 5 fb^{-1} of Data from the ATLAS Detector*. Prépublication ATLAS-CONF-2012-043, CERN, Geneva (2012), URL `http://cds.cern.ch/record/1435197`. 84

[113] Aad, G. et al., *Measurement of the Mistag Rate with 5 fb^{-1} of Data Collected by the ATLAS Detector*. Prépublication ATLAS-CONF-2012-040, CERN, Geneva (2012), URL `http://cds.cern.ch/record/1435194`. 84

[114] Kidonakis, N., *NNLL resummation for s-channel single top quark production*. Phys. Rev., **D81**: 054 028 (2010), doi:10.1103/PhysRevD.81.054028, arXiv:1001.5034. 85

[115] Kidonakis, N., *Next-to-next-to-leading-order collinear and soft gluon corrections for t-channel single top quark production*. Phys. Rev., **D83**: 091 503 (2011), doi:10.1103/PhysRevD.83.091503, arXiv:1103.2792.

[116] Kidonakis, N., *Two-loop soft anomalous dimensions for single top quark associated production with a W- or H-*. Phys. Rev., **D82**: 054 018 (2010), doi:10.1103/PhysRevD.82.054018, arXiv:1005.4451. 85

[117] Kersevan, B. P. et Richter-Was, E., *The Monte Carlo event generator AcerMC versions 2.0 to 3.8 with interfaces to PYTHIA 6.4, HERWIG 6.5 and ARIADNE 4.1*. Comput. Phys. Commun., **184**: 919–985 (2013), doi:10.1016/j.cpc.2012.10.032, arXiv:hep-ph/0405247. 85

[118] Aad, G. et al., *Measurement of $t\bar{t}$ production with a veto on additional central jet activity in pp collisions at sqrt(s) = 7 TeV using the ATLAS detector*. Eur. Phys. J., **C72**: 2043 (2012), doi:10.1140/epjc/s10052-012-2043-9, arXiv:1203.5015. 85

[119] Martin, A. D., Stirling, W. J., Thorne, R. S. et Watt, G., *Parton distributions for the LHC*. Eur. Phys. J., **C63**: 189–285 (2009), doi:10.1140/epjc/s10052-009-1072-5, arXiv:0901.0002. 86

[120] Martin, A. D., Stirling, W. J., Thorne, R. S. et Watt, G., *Uncertainties on alpha(S) in global PDF analyses and implications for predicted hadronic cross sections*. Eur. Phys. J., **C64**: 653–680 (2009), doi:10.1140/epjc/s10052-009-1164-2, arXiv:0905.3531. 86

[121] Gao, J., Guzzi, M., Huston, J. et al., *CT10 next-to-next-to-leading order global analysis of QCD*. Phys. Rev., **D89** (3): 033 009 (2014), doi:10.1103/PhysRevD.89.033009, arXiv:1302.6246. 86

[122] Ball, R. D. et al., *Parton distributions with LHC data*. Nucl. Phys., **B867**: 244–289 (2013), doi:10.1016/j.nuclphysb.2012.10.003, arXiv:1207.1303. 86

[123] Botje, M. et al., *The PDF4LHC Working Group Interim Recommendations*. Eur. Phys. J. (2011), arXiv:1101.0538. 86

[124] Baak, M., Besjes, G. J., Côte, D. et al., *HistFitter software framework for statistical data analysis*. Eur. Phys. J., **C75**: 153 (2015), doi:10.1140/epjc/s10052-015-3327-7, arXiv:1410.1280. 93, 94, 96

[125] Read, A. L., *Presentation of search results: the CL s technique*. Journal of Physics G: Nuclear and Particle Physics, **28** (10): 2693 (2002), URL `http://stacks.iop.org/0954-3899/28/i=10/a=313`. 93

[126] Cowan, G., Cranmer, K., Gross, E. et Vitells, O., *Asymptotic formulae for likelihood-based tests of new physics*. Eur. Phys. J., **C71**: 1554 (2011), doi:10.1140/epjc/s10052-011-1554-0,10.1140/epjc/s10052-013-2501-z, arXiv:1007.1727. [Erratum: Eur. Phys. J.C73,2501(2013)]. 94

[127] Read, A. L., *Presentation of search results: The CL(s) technique*. J. Phys., **G28**: 2693–2704 (2002), doi:10.1088/0954-3899/28/10/313. [,11(2002)]. 96

A Natural units

The base quantities in human scale are mass, length and time from which are derived velocity, angular momentum and energy, illustrated in Table A.1.

Quantity	Dimensions	Units
Mass	[M]	1 kg
Length	[L]	1 m
Time	[T]	1 s
Velocity	[L T^{-1}]	1 m s^{-1}
Angular momentum	[M L^2 T^{-1}]	1 kg m^2 s^{-1}
Energy	[M L^2 T^{-2}]	1 J

Table A.1: International System of Units (SI). Velocity and angular momentum are derived from mass, length and time.

However, in particle physics these units are not appropriate since we work with particles which compose the proton with a mass of m_p=1.67 10^{-27} kg and size as small as $r_P = 0.8\ 10^{-15}$ m. Therefore, we use natural units in which Special Relativity speed of light in vacuum $c = 3.0\ 10^8$ m s^{-1} and Quantum Mechanics reduced Planck's constant $\hbar = 1.055\ 10^{-34}$ J s^{-1} are set to one $\hbar \equiv c \equiv 1$. The consequence of this set is that the equation of a mass, m, at rest $E^2 = p^2c^2 + m^2c^4$ becomes $E^2 = p^2 + m^2$ and so energy, velocity and angular momentum as expressed as base quantities and the units from table A.1 are transformed as illustrated in table A.2. Thus, a proton at rest has an energy (or equivalent mass) of $E = m_p = 0{:}938$ GeV.

Quantity	Dimensions	Units
Energy	[E]	1 GeV = 1.602 10^{10} J
Velocity	[V]	1 (unit of c)
Angular momentum	[W]	1 (unit of $\hbar$)
Mass	[E V^2]	1 GeV (unit of c)^2
Length	[V W E^{-1}]	1 (unit of c) (unit of $\hbar$) GeV^{-1}
Time	[W E^{-1}]	1 (unit of $\hbar$) GeV^{-1}

Table A.2: Natural units used in Particle Physics: mass, length and time are derived from energy, angular momentum and velocity.

B tZ channel sensitivity

In this appendix, we want to check the sensitivity of the samples produced via madgraph only for $T \to tZ$ channel without LO→NLO K-factor.

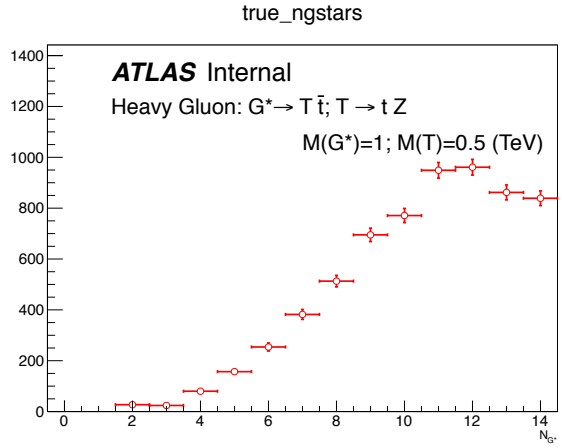

(a) Number of heavy gluon.

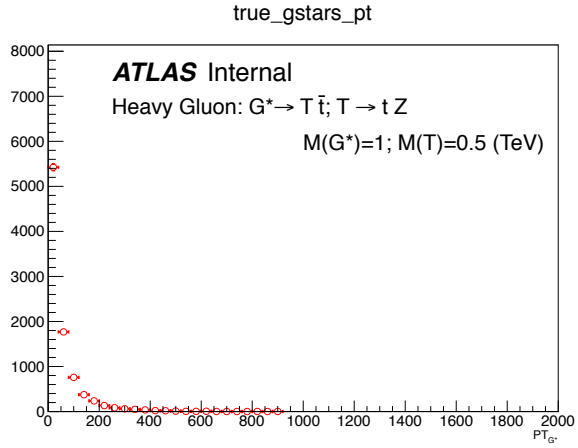

(b) Heavy gluon p_T.

Figure B.1: First generation of particles: Heavy Gluons (G*).

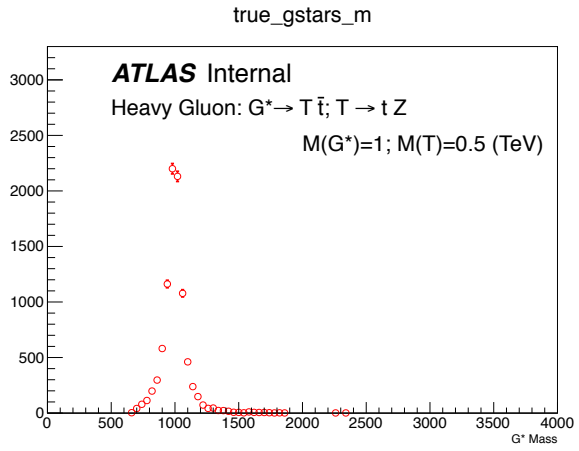

(a) Heavy Gluon mass in GeV.

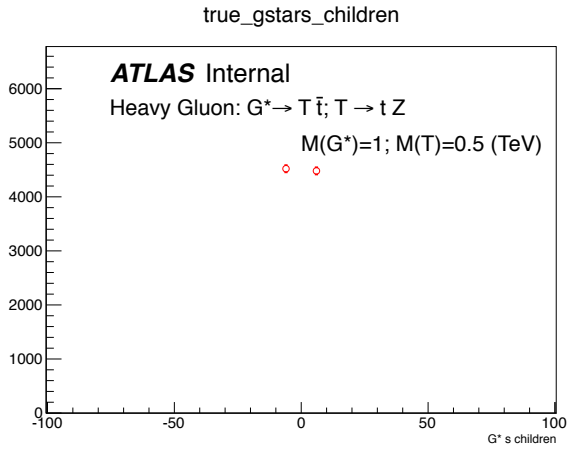

(b) Heavy Gluon Children: 50 % of top and 50 % of anti-top.

Figure B.2: First generation of particles: Heavy Gluons (G*).

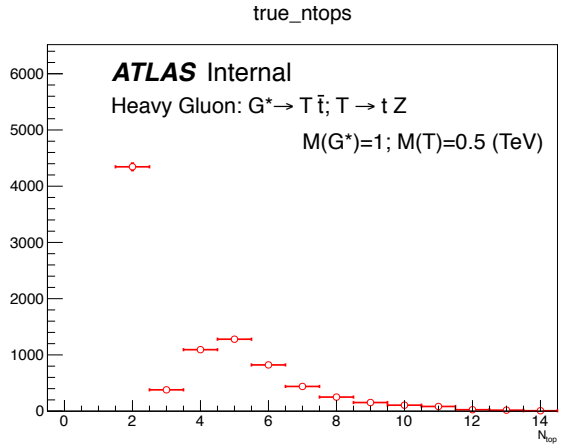

(a) Number of SM top.

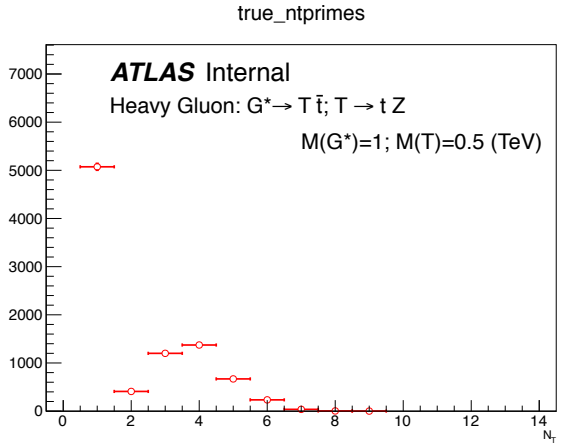

(b) Number of VLQ top quarks.

Figure B.3: Second generation of particles: SM top and VLQ top.

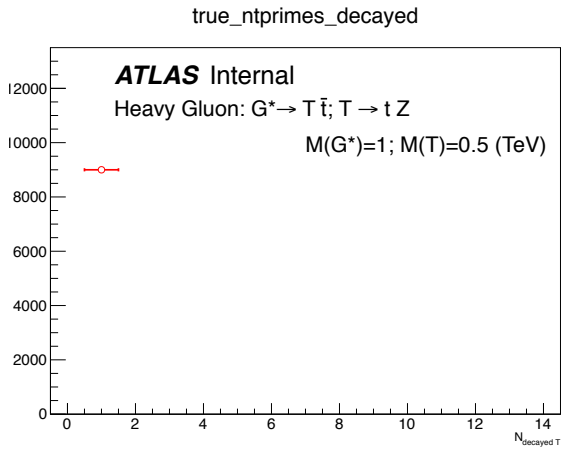

(a) Number of Decayed VLQ top.

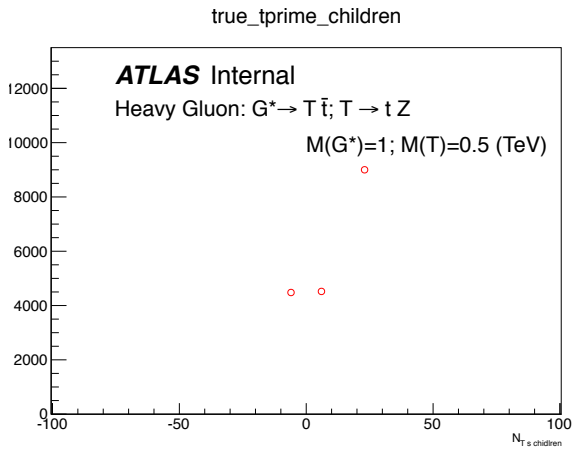

(b) VLQ top quarks Children

Figure B.4: Second generation of particles: VLQ top (T)

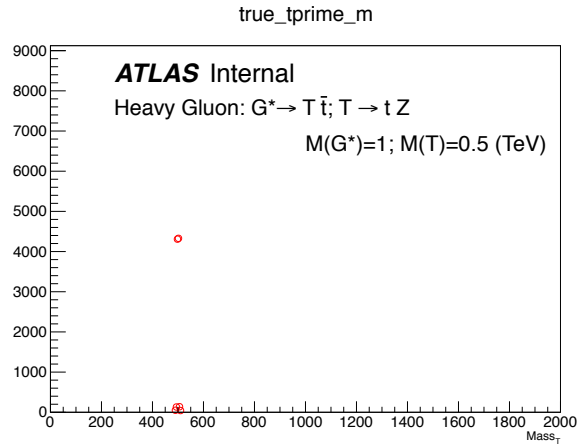

(a) VLQ top quarks Mass in GeV.

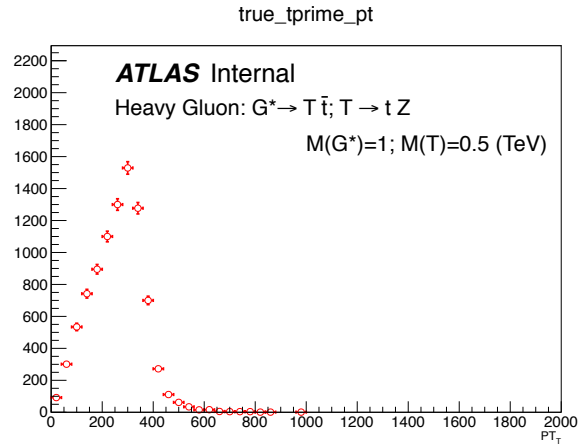

(b) VLQ top quarks $p_T(T)$ in GeV.

Figure B.5: Second generation of particles: VLQ top (T)

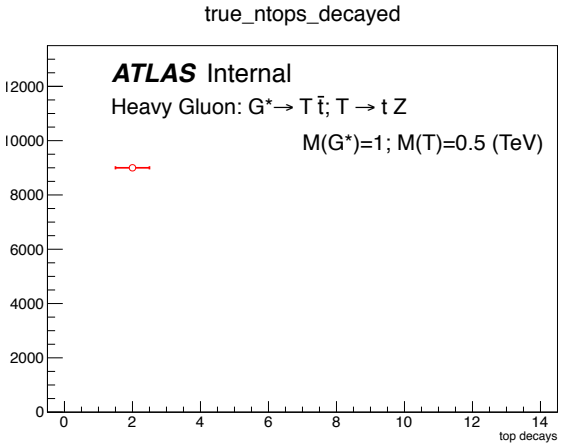

(a) Number of Decayed SM top quarks.

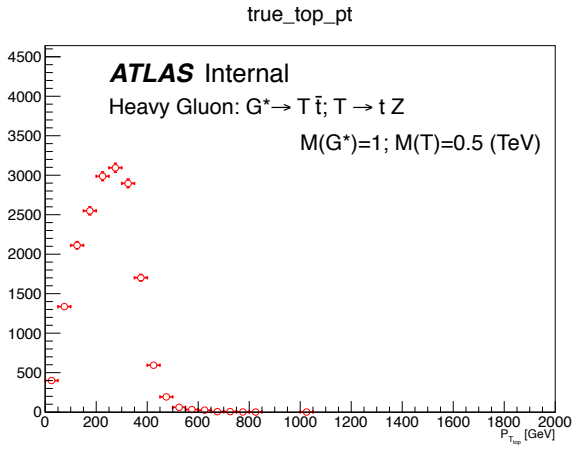

(b) SM top quarks $P_T(t))$ in GeV.

Figure B.6: Second generation of particles: SM top

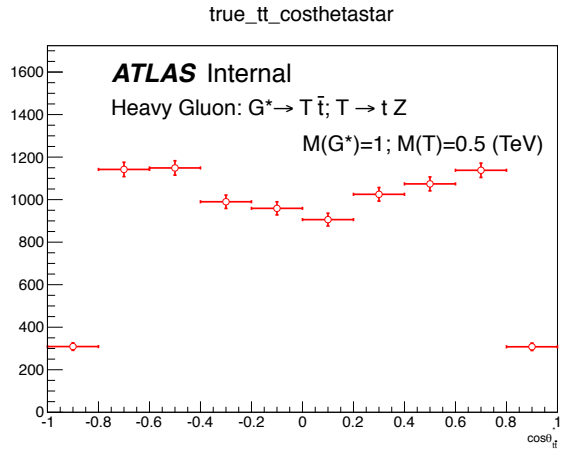

(a) Top quarks Rapidity($y_{t\bar{t}}$).

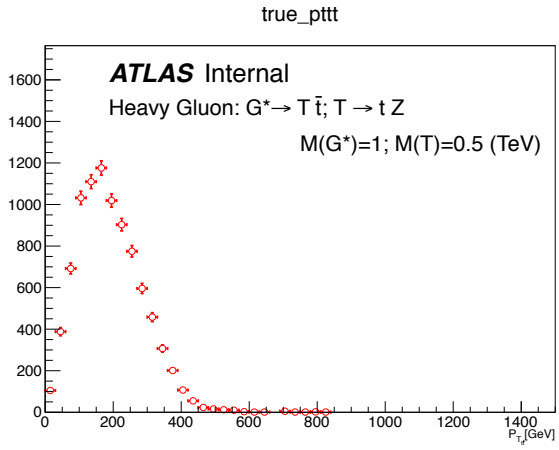

(b) $t\bar{t}$ transverse momentum.

Figure B.7: Second generation of particles: SM top.

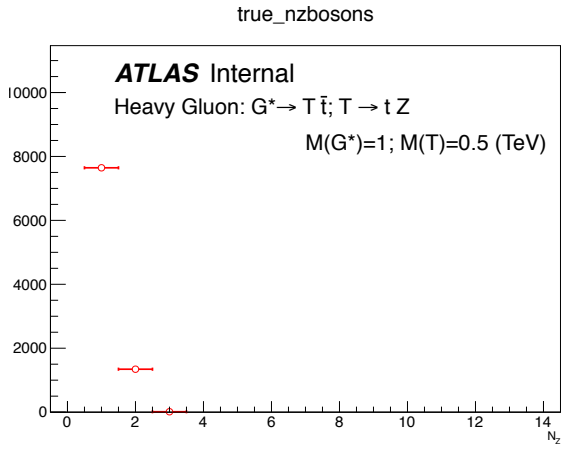

(a) Number of Z Bosons.

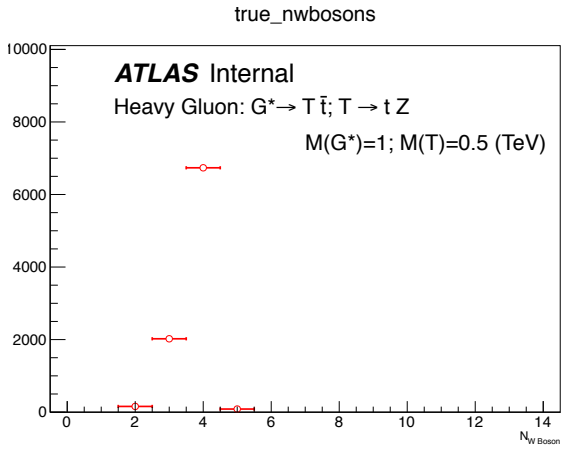

(b) Number of W bosons.

Figure B.8: nW boson.

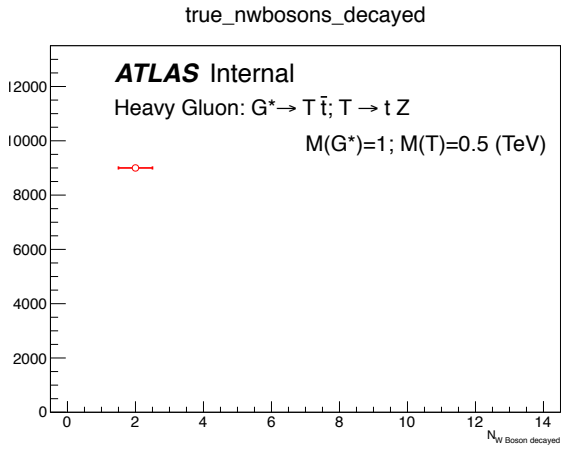

(a) Number of Decayed W Bosons.

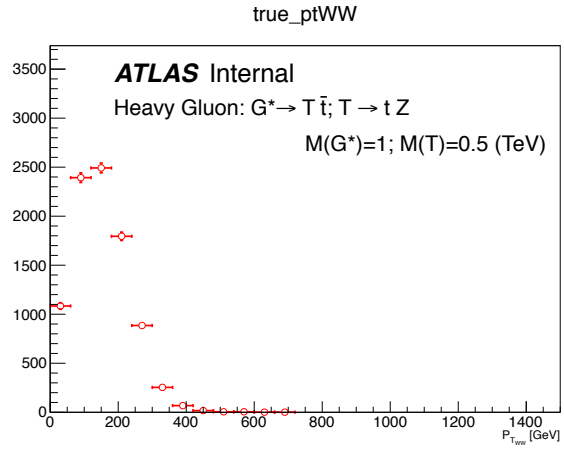

(b) Dibosons $P_T(WW)$.

Figure B.9: W boson.

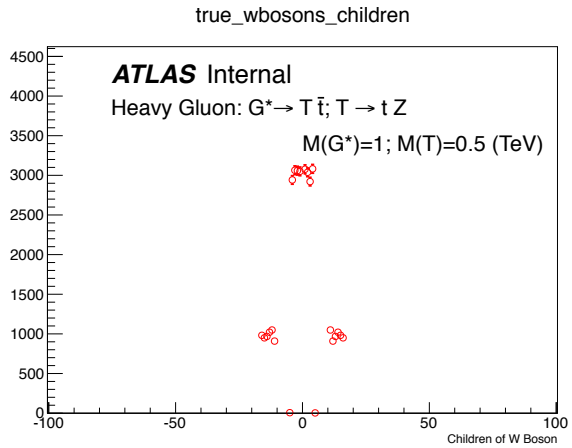

(a) W Bosons Children.

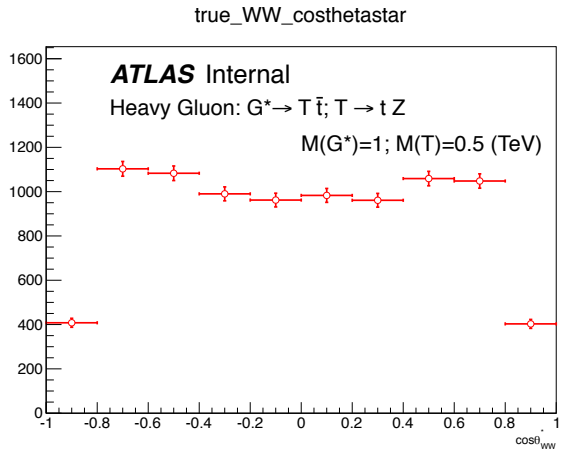

(b) Centre-of-mass scattering angle $cos[\theta^*(WW)]$ of the WW system.

Figure B.10: Third generation of particles: W bosons and b quarks.

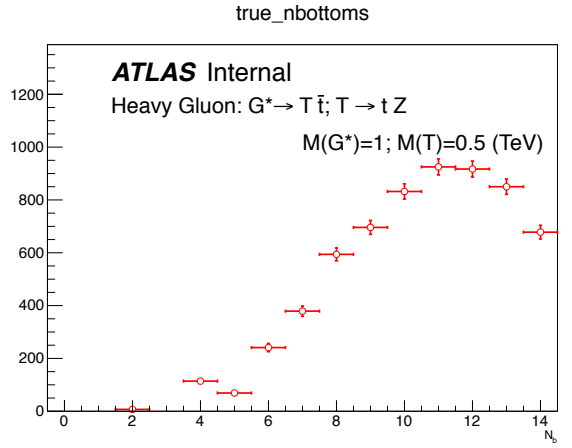

(a) Number of b quarks.

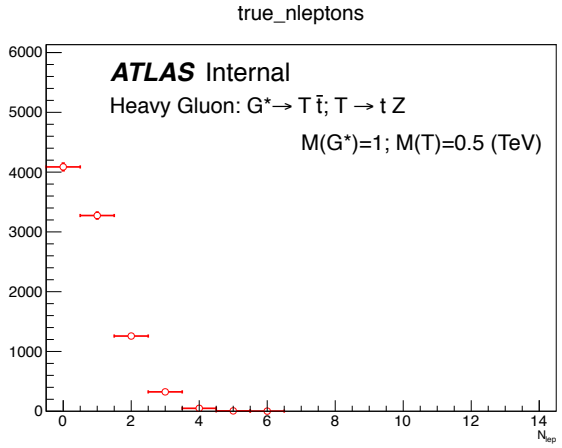

(b) Number of Leptons.

Figure B.11: b quarks and fourth generation of particles: Leptons.

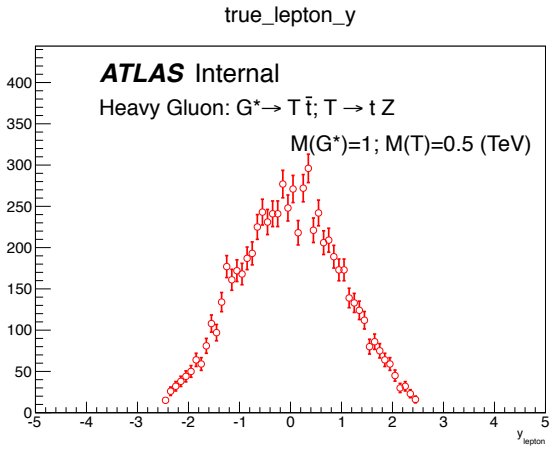

(a) Leptons Rapidity (y_{lepton}).

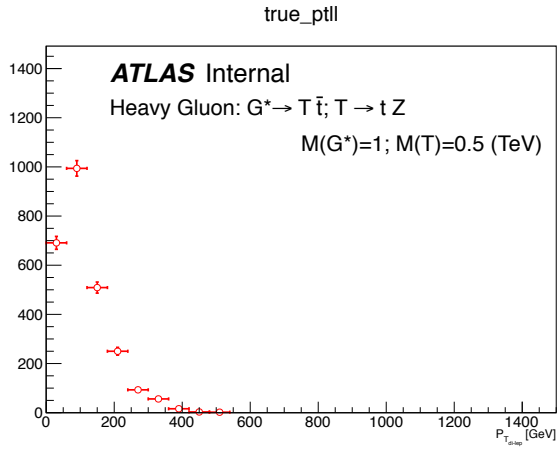

(b) Dileptons $P_T(l\bar{l})$ in GeV .

Figure B.12: Fourth generation of particles: Leptons.

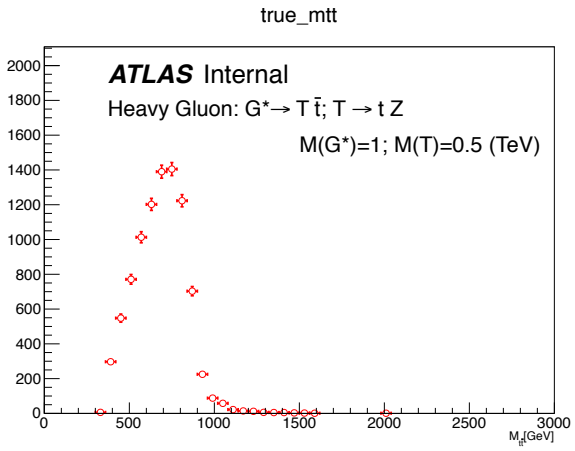

Figure B.13: $t\bar{t}$ Mass.

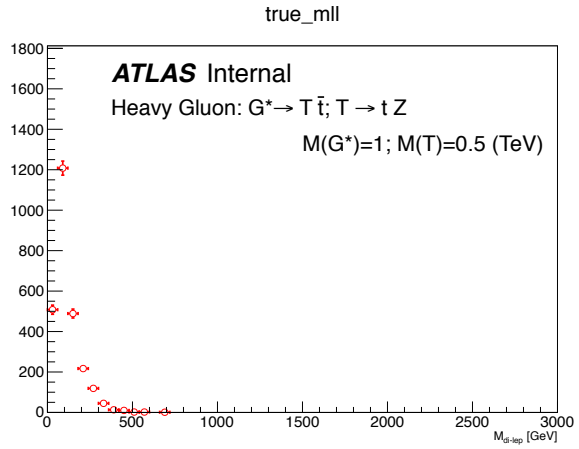

(a) Dileptons Mass ($M(l\bar{l})$ in GeV).

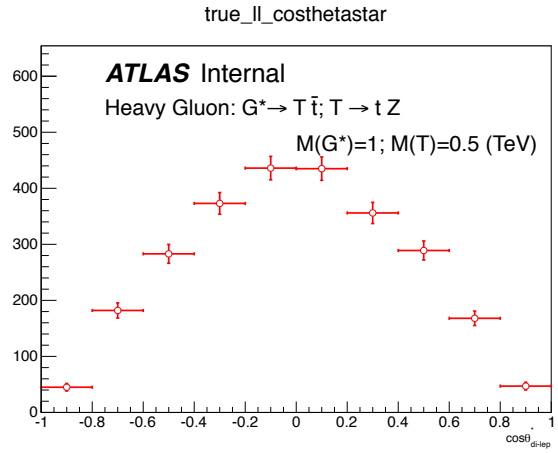

(b) Centre-of-mass scattering angle $cos[\theta^*(l\bar{l})]$ of the dilepton system.

Figure B.14: Fourth generation of particles: Leptons.

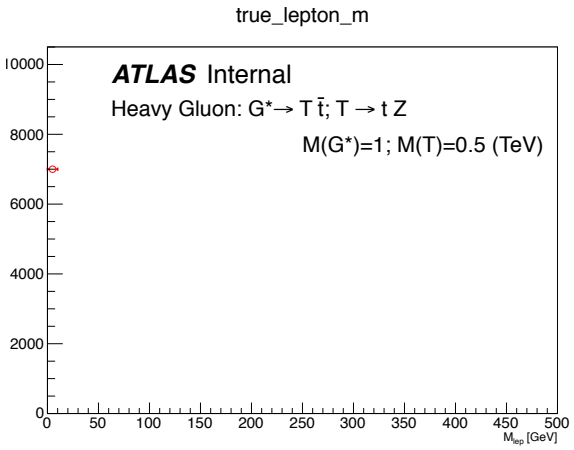

(a) Lepton Mass ($M(l\bar{l})$ in GeV).

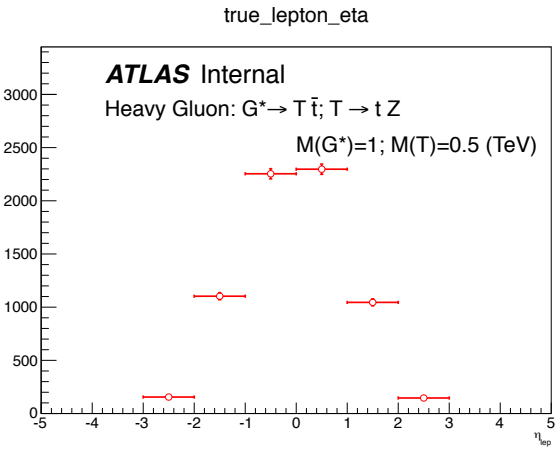

(b) Lepton η.

Figure B.15: Fourth generation of particles: Leptons.

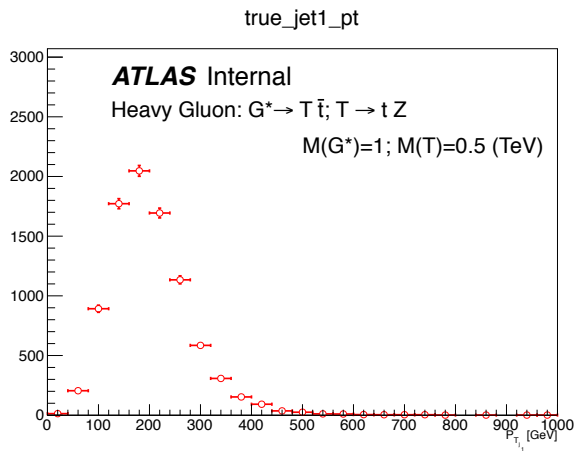

(a) Leading jet $P_T(j_1)$ in GeV.

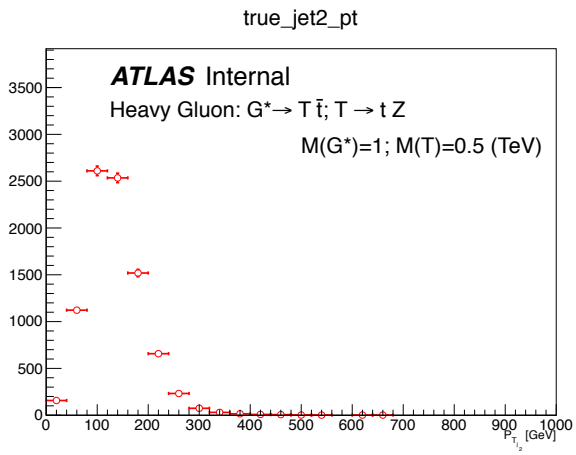

(b) Second Leading jet $P_T(j_2)$ in GeV.

Figure B.16: Fourth generation of particles: Jets.

C tH channel sensitivity

In this appendix, we want to check the sensitivity of the samples produced via madgraph only for $T \to tH$ channel without LO→NLO K-factor.

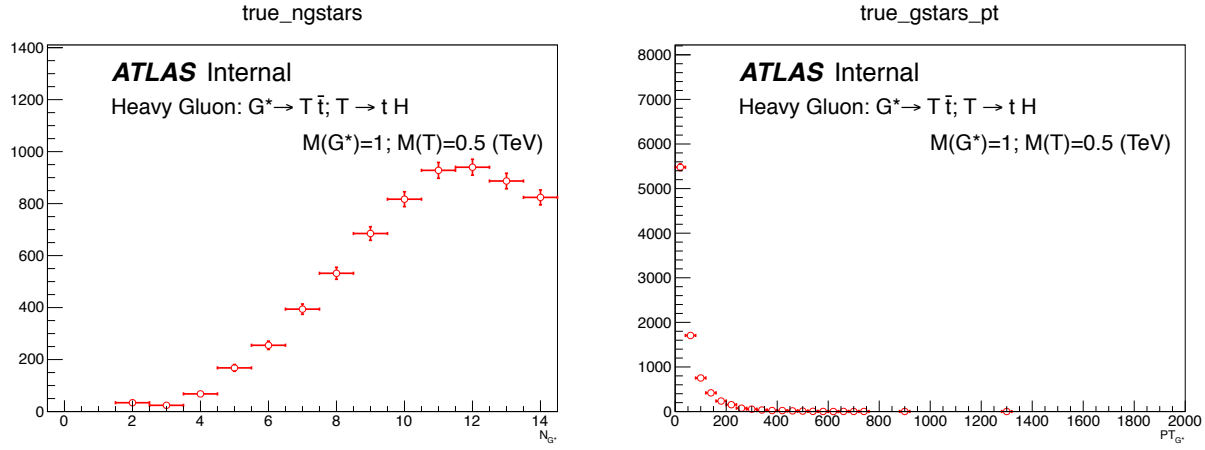

(a) Number of heavy gluon.

(b) Heavy gluon p_T.

Figure C.1: First generation of particles: Heavy Gluons (G*).

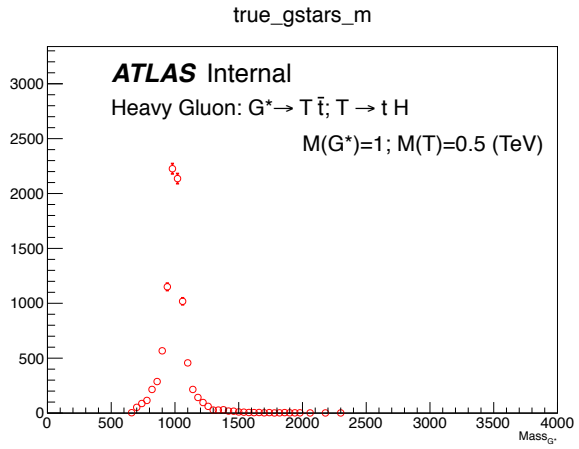

(a) Heavy Gluon mass in GeV.

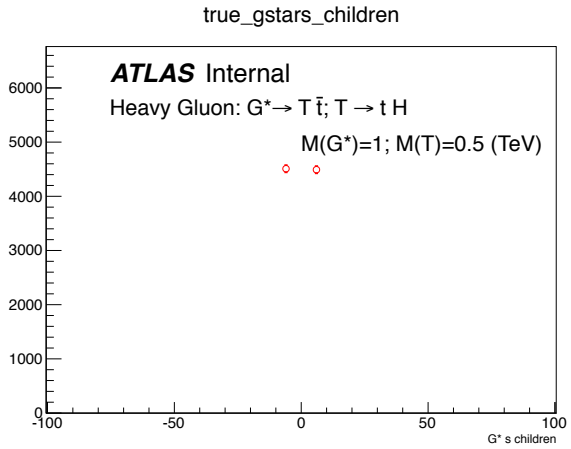

(b) Heavy Gluon Children: 50 % of top and 50 % of anti-top.

Figure C.2: First generation of particles: Heavy Gluons (G*).

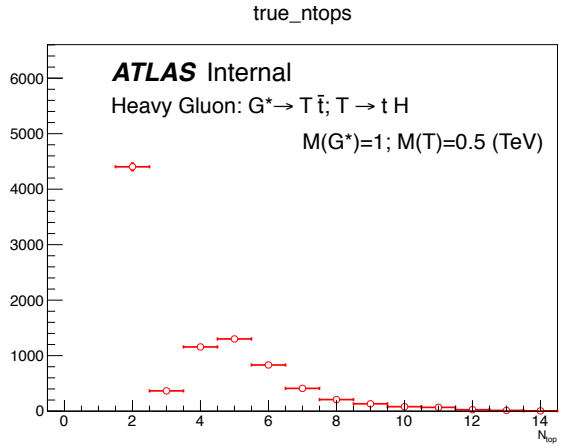

(a) Number of SM top.

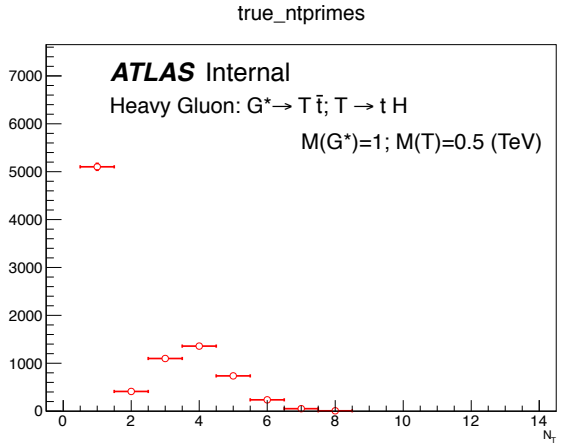

(b) Number of VLQ top quarks.

Figure C.3: Second generation of particles: SM top and VLQ top.

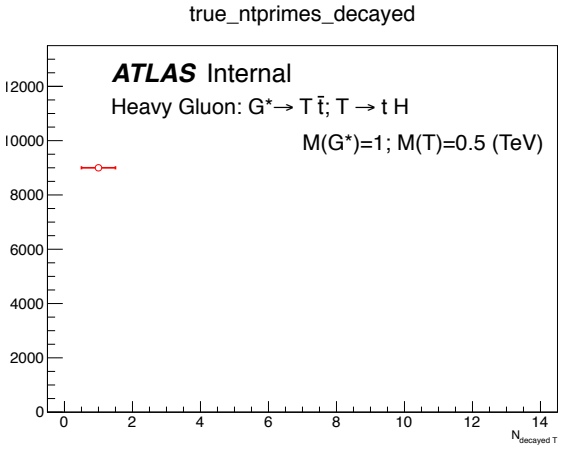

(a) Number of Decayed VLQ top.

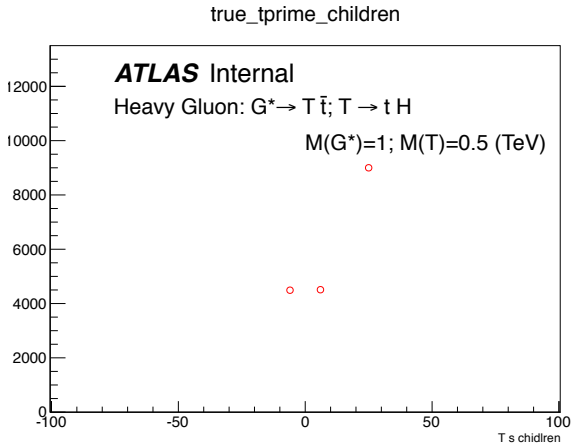

(b) VLQ top quarks Children

Figure C.4: Second generation of particles: VLQ top (T)

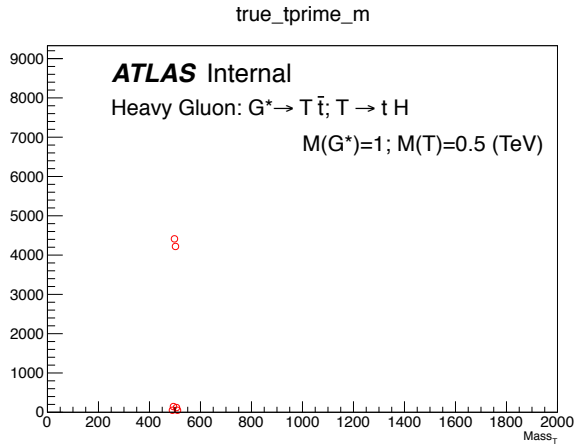

(a) VLQ top quarks Mass in GeV.

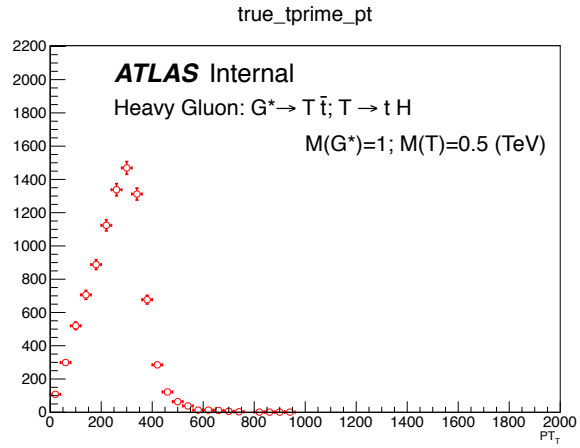

(b) VLQ top quarks $p_T(T)$ in GeV.

Figure C.5: Second generation of particles: VLQ top (T)

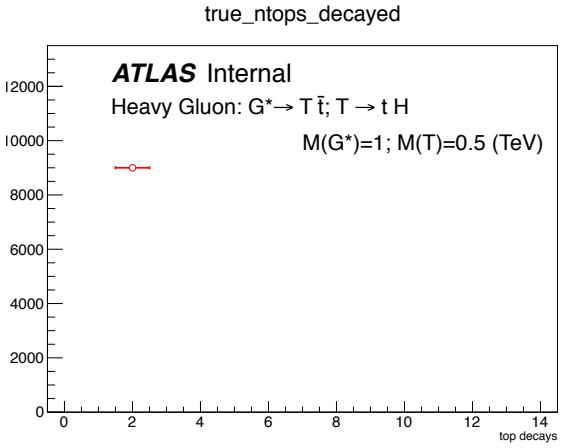

(a) Number of Decayed SM top quarks.

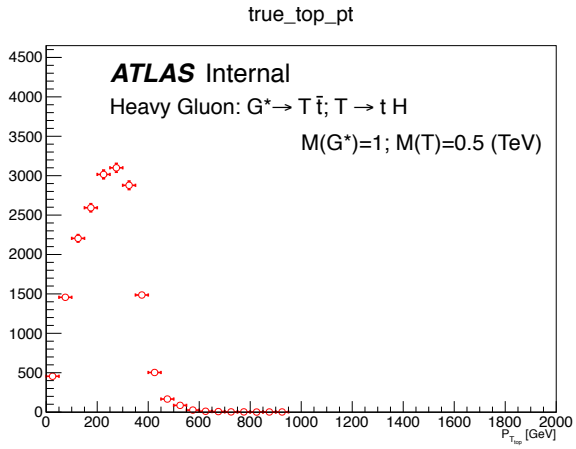

(b) SM top quarks $P_T(t))$ in GeV.

Figure C.6: Second generation of particles: SM top

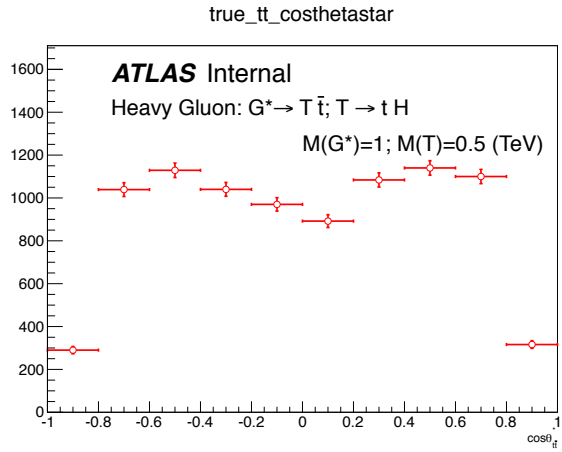

(a) Top quarks Rapidity($y_{t\bar{t}}$).

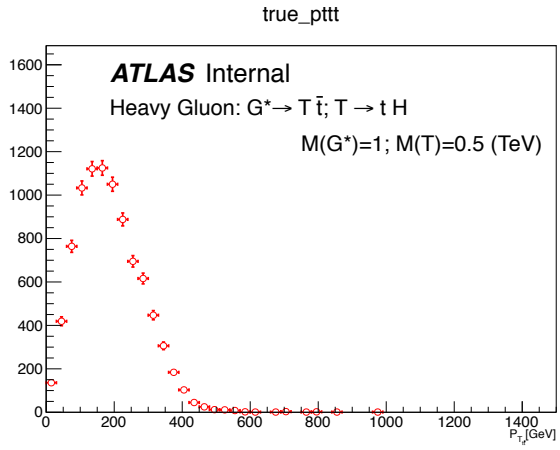

(b) $t\bar{t}$ transverse momentum.

Figure C.7: Second generation of particles: SM top.

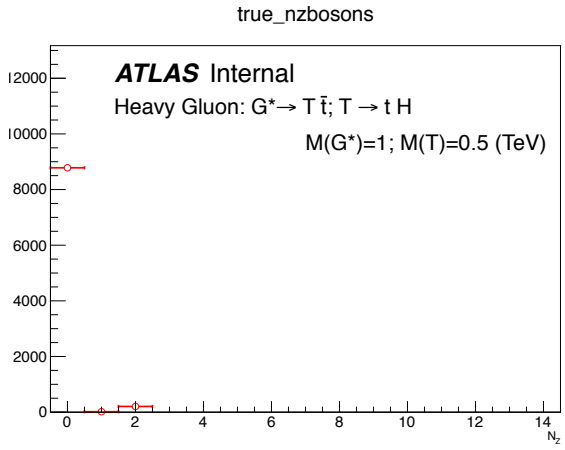

(a) Number of Z Bosons.

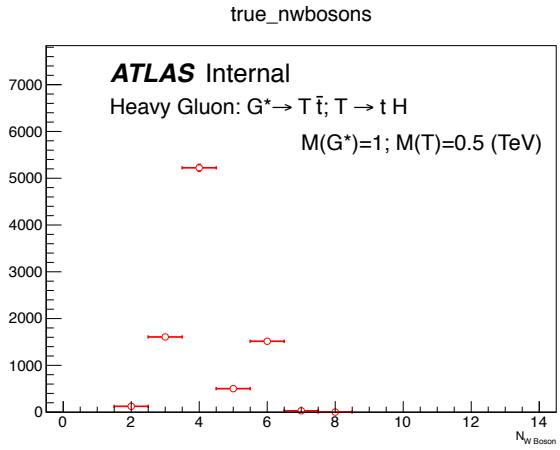

(b) Number of W bosons.

Figure C.8: nW boson.

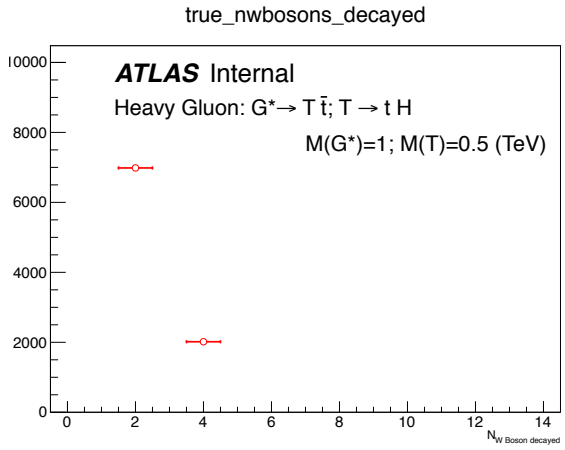

(a) Number of Decayed W Bosons.

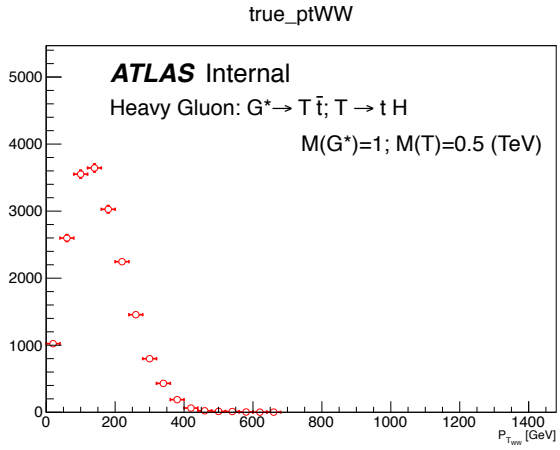

(b) Dibosons $P_T(WW)$.

Figure C.9: W boson.

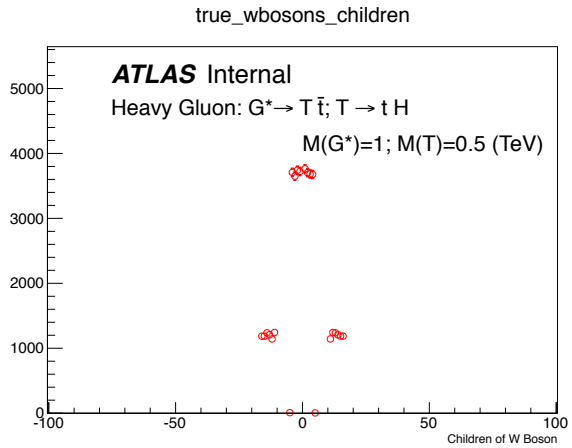

(a) W Bosons Children.

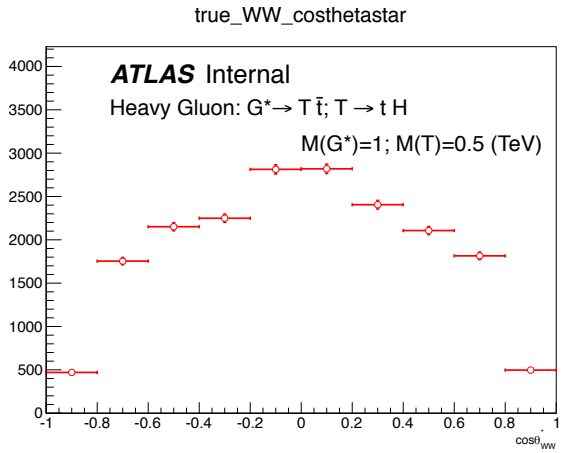

(b) Centre-of-mass scattering angle $cos[\theta^*(WW)]$ of the WW system.

Figure C.10: Third generation of particles: W bosons and b quarks.

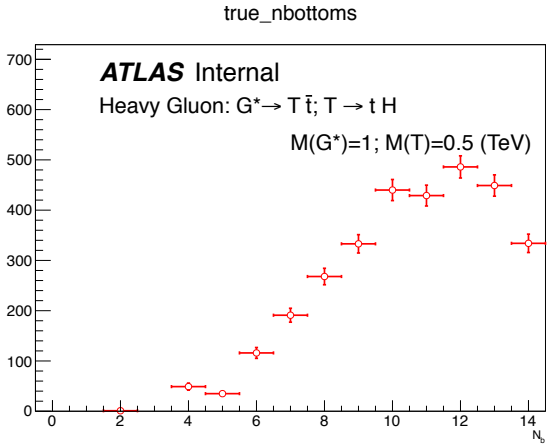

(a) Number of b quarks.

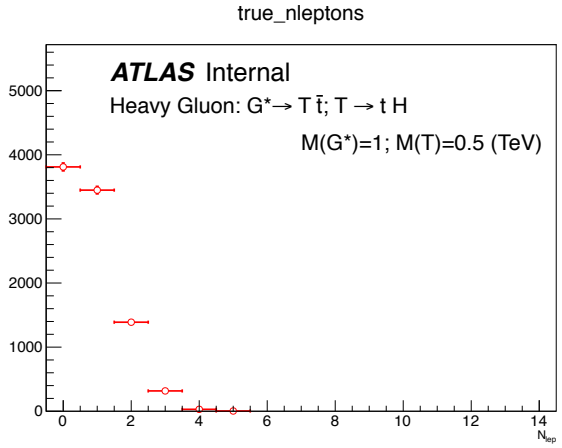

(b) Number of Leptons.

Figure C.11: b quarks and fourth generation of particles: Leptons.

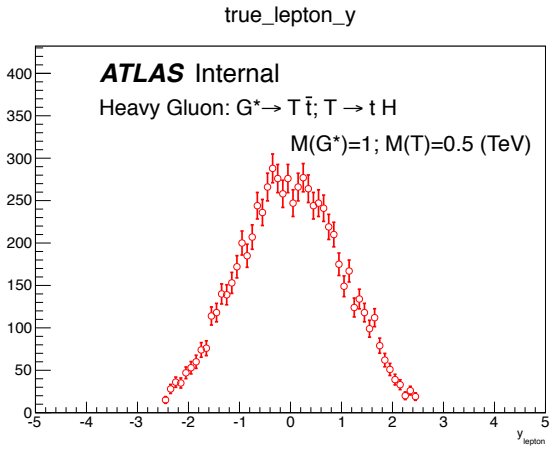

(a) Leptons Rapidity (y_{lepton}).

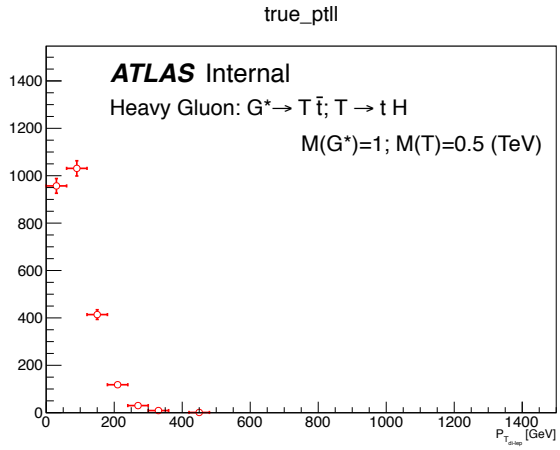

(b) Dileptons $P_T(l\bar{l})$ in GeV .

Figure C.12: Fourth generation of particles: Leptons.

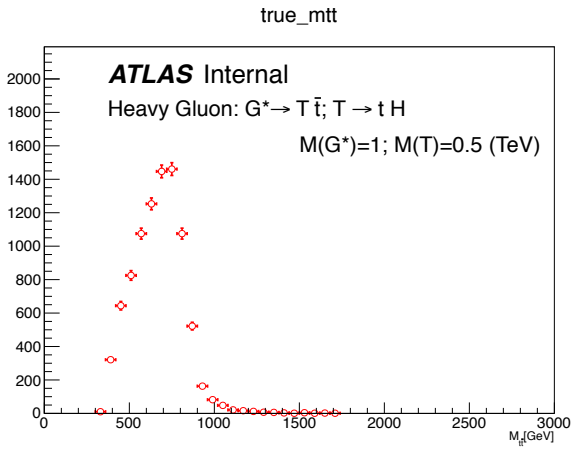

Figure C.13: $t\bar{t}$ Mass.

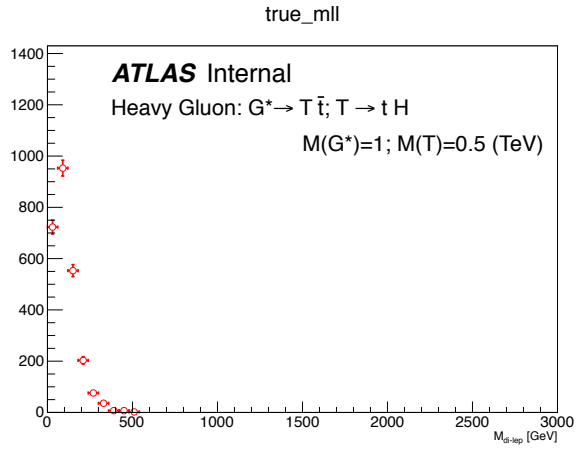

(a) Dileptons Mass ($M(l\bar{l})$ in GeV).

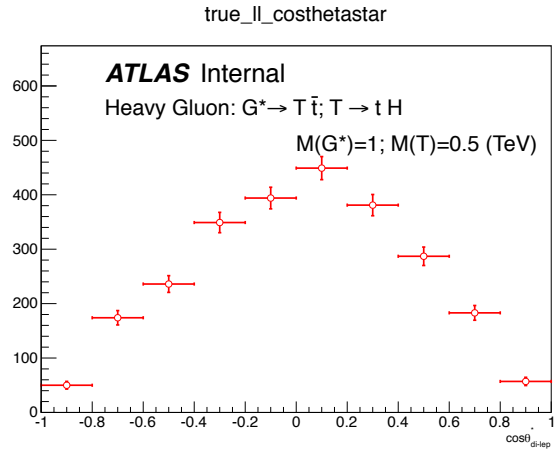

(b) Centre-of-mass scattering angle $cos[\theta^*(l\bar{l})]$ of the dilepton system.

Figure C.14: Fourth generation of particles: Leptons.

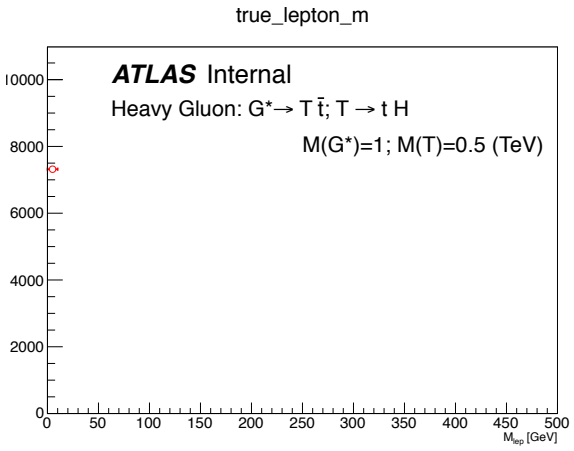

(a) Lepton Mass ($M(l\bar{l})$ in GeV).

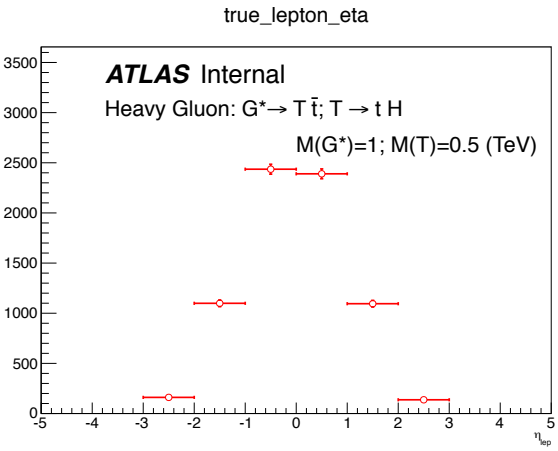

(b) Lepton η.

Figure C.15: Fourth generation of particles: Leptons.

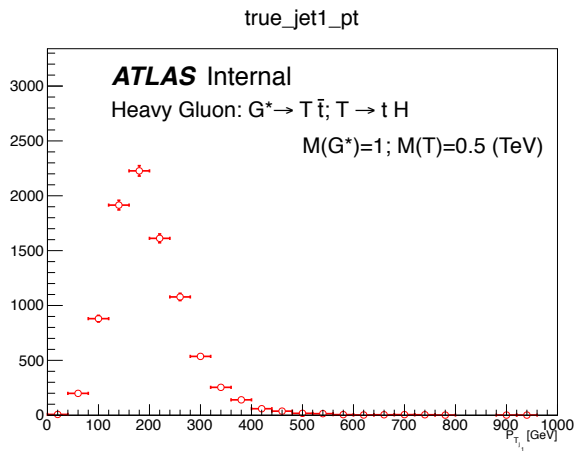

(a) Leading jet $P_T(j_1)$ in GeV.

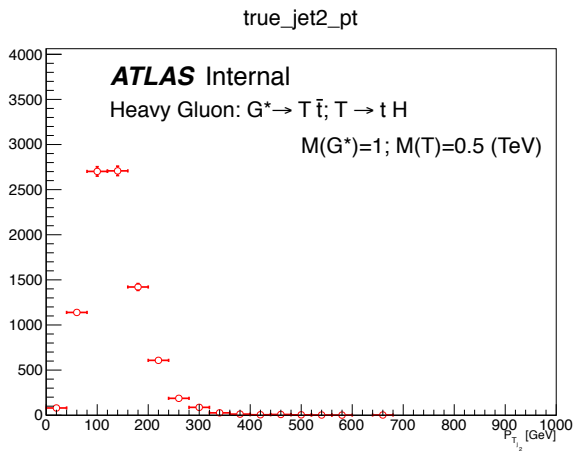

(b) Second Leading jet $P_T(j_2)$ in GeV.

Figure C.16: Fourth generation of particles: Jets.